

1997

Spatial, Geostatistical, and Fractal Measures of Seafloor Microtopography Across the Eel River Shelf, off Northern California

George Randall. Cutter
College of William and Mary - Virginia Institute of Marine Science

Follow this and additional works at: <https://scholarworks.wm.edu/etd>



Part of the [Geology Commons](#), and the [Oceanography Commons](#)

Recommended Citation

Cutter, George Randall., "Spatial, Geostatistical, and Fractal Measures of Seafloor Microtopography Across the Eel River Shelf, off Northern California" (1997). *Dissertations, Theses, and Masters Projects*. Paper 1539617726.

<https://dx.doi.org/doi:10.25773/v5-ec7f-2x60>

This Thesis is brought to you for free and open access by the Theses, Dissertations, & Master Projects at W&M ScholarWorks. It has been accepted for inclusion in Dissertations, Theses, and Masters Projects by an authorized administrator of W&M ScholarWorks. For more information, please contact scholarworks@wm.edu.

SPATIAL, GEOSTATISTICAL, AND FRACTAL MEASURES OF
SEAFLOOR MICROTOPOGRAPHY ACROSS THE EEL RIVER SHELF,
OFF NORTHERN CALIFORNIA

A Thesis
Presented to
The Faculty of the School of Marine Science
College of William and Mary

In Partial Fulfillment
Of the Requirements for the Degree of
Master of Science


by
G. Randy Cutter, Jr.

1997

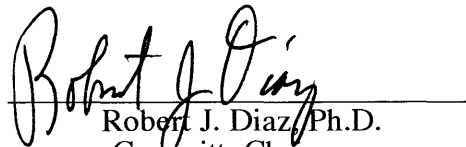
APPROVAL SHEET

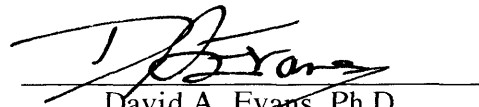
This thesis is submitted in partial fulfillment
of the requirements for the degree of


Master of Science


G. R. Cutler, Jr.

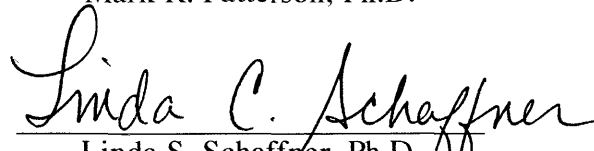
Approved: December, 1997


Robert J. Diaz, Ph.D.
Committee Chairman


David A. Evans, Ph.D.


Jerome P.-Y. Maa, Ph.D.


Mark R. Patterson, Ph.D.


Linda S. Schaffner, Ph.D.

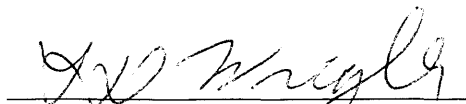

L. Donelson Wright, Ph.D.

TABLE OF CONTENTS

ABSTRACT	v
INTRODUCTION	2
Summary of study	2
Background	3
Seafloor roughness	5
Micro to macro-scale	5
Large scale	7
STUDY AREA	10
METHODS	12
Sampling	12
Sediment profile imaging	12
Mechanics	12
Profile images and SPI analysis	13
Data source	14
Digital image storage and processing	14
Sediment-water interface (SWI) profile contour extraction	15
Manual tracing	15
Automated image processing routines	15
Spatial domain processing	16
Frequency (wavenumber) domain processing	16
Imaging the sediment-water interface	17
Roughness measures applied to SWI	19
Descriptive statistics	19
Semivariogram	19
Semivariogram components	20
Determination of scaling properties	20
Fractal measures	22
Demonstration of fractal measures	24
Hausdorff measure	25
Minkowski dimension	26
Isotropy and anisotropy	26
RESULTS	28
Benthic habitat characteristics	28
General description	28
Parameterizations by water depth, sediment type, and biological activity	28
Flood deposit layer thickness	28
Measured SPI parameters	29
Apparent color RPD	29
SPI prism penetration	29
Sediment grain size	29
Bioturbation and sediment mixing	30
Examination of parameters by flood deposit thickness	30
Sediment-water interface spatial analysis and roughness measures	31
Semivariance of microtopographical elevations	31
Surface relief	32
Standard deviation of the SWI	32
Fractal dimensions (measures)	33

Hausdorff	33
Minkowski	33
Power spectral slopes	34
Comparison of traced and auto-extracted SWI contours	35
Isotropy of micro-scale roughness	35
Comparison of parameters from cross-crest to crest parallel images	35
Statistical tests comparing roughness measures grouped by habitat type	36
Multiple regression	36
DISCUSSION AND CONCLUSIONS	38
Habitat characteristics and the influence of Eel River flood deposit	38
Spatial processes of the seafloor at micro scales	39
Generalized biologically-influenced roughness in the area	40
Spatial aspects of roughness	43
ACKNOWLEDGEMENTS	49
REFERENCES	50
TABLES	54
FIGURES	66
APPENDIX A	109
APPENDIX B	119

ABSTRACT

Physically-induced and biologically-induced seafloor roughness features are both common in soft sediments. Rarely is only one manifestation present. If only physical roughness features are present, they may be accounted for in mathematical terms which utilize their geometries. These geometrical depictions of roughness elements may be then translated to hydraulic roughness. Biological roughness features are typically more difficult to describe geometrically. This stems from both the variable morphologies of obvious biological roughness elements, and from the possibility that non-obvious biological surface roughness features are present due to infaunal activities. When a combination of physical, obvious and non-obvious biological roughness features are all present, quantifying roughness element geometries is especially difficult, and separation of components may be infeasible. Therefore, seafloor roughness may be better characterized by integrative measures which convey information about the geometries of all component elements.

This study characterized integrated physical and biological seafloor roughness by various measures of the sediment water interface defined using high-resolution digital sediment profile imagery. 15 cm sections of the sediment-water interface were extracted from profile images in order to quantify roughness. Scaling behavior of roughness was described using semivariogram functions. The small-scale seafloor roughness appeared self-affine over certain scales, but apparently scale-dependent beyond those. However semivariograms from scale-dependent and fractal processes may be similar if only part of the scaling behavior is observed, therefore fractal behavior of the seafloor could not be ruled out. Roughness was measured using statistical, fractal and spectral measures.

A transect across the Eel River continental shelf encountered two major geophysical zones: inshore sands with wave-induced structures, and mid-shelf mud-deposits with high levels of bioturbation. The geophysical zones could not be distinguished in terms of surface roughness using the statistical or fractal measures, but could be distinguished by the spectral slope. Micro (<1 mm to 5 cm) and macro-scale (>5 to 15 cm) roughness behavior was different across the study area, apparently due to the primary forcing factors and substrate composition. Therefore, although distinction between the physical and biological roughness elements may be possible using a commonly applied methodology, many promising roughness measures are confounded by nearly similar geometries.

SPATIAL, GEOSTATISTICAL, AND FRACTAL MEASURES OF SEAFLOOR
MICROTOPOGRAPHY ACROSS THE EEL RIVER SHELF, OFF NORTHERN CALIFORNIA

INTRODUCTION

Summary of Study

Several methods have been commonly applied to quantify the roughness or variability of the seafloor. Techniques generally vary by discipline and scale of the studied process. Each approach to roughness characterization has its merits, and all are useful for certain circumstances. Certain measures may be more efficient, as in able to convey more information about the character of the surface complexity, or more simple to calculate than others, and apply to more diverse roughness elements encountered. This study applied several roughness measures to microtopographical feature profiles and tests assumptions for their application. The measures applied were: simple statistical measures, geostatistical measures, fractal measures, and Fourier spectra. The objective was to characterize integrated physical and biological seafloor roughness by various measures of the sediment water interface defined using high-resolution digital sediment profile imagery.

In order to examine seafloor microtopographical roughness, and to relate roughness to the sedimentary environment and bioturbation on the Eel River continental shelf, seven procedures were implemented. 1) Standard analyses were applied to sediment profile images to describe qualitatively and quantitatively benthic habitat characteristics similar to Bonsdorff et al. (1996) such as sediment-type and grain size, depth of the apparent color redox potential discontinuity, signs of infaunal activity, and infaunal and epifaunal presence. 2) Image processing methods were used to extract the sediment-water interface profile contour from images, so that roughness measures could be applied to just the configuration of the interface. 3) Simple statistical roughness measures were estimated. 4) Geostatistical analyses were performed to describe the spatial relationships of roughness elements and to determine the scaling behavior of the seafloor examined at these scales (< 1 mm to 150 mm). 5) Fractal measures were calculated for the sediment-water interface contours. 6) Power spectra were calculated for piecewise continuous versions of the

sediment-water interface contours. 7) Summary statistics were calculated and comparisons were made of roughness measures in relation to different physical and biological habitat attributes.

Background

Seafloor roughness, or the variation and spatial organization of seafloor elevation and geometry, results from interactions between substrate composition, near-bottom flow dynamics and benthic and epibenthic biology. I used the terms microscale and macro-scale roughness to distinguish categories of small-scale seafloor roughness features based upon the horizontal component of the elements. Roughness elements were described as micro-scale seafloor roughness when vertical elevation changes were contained by elements with horizontal components of less than a millimeter to about five centimeters, and macro-scale roughness elements as those associated with horizontal gradients greater than about five centimeters. Micro and macro-scale roughness influences the behavior of acoustic waves, with which most mapping of the seafloor is accomplished (Goff et al., 1996), and also influences benthic boundary layer flow dynamics and material transport by momentum and mass transfer effects (Wright, et al., 1997; Grant and Madsen, 1986). Quantification of the small-scale roughness thus is important for proper interpretation of acoustic seafloor mapping and for the prediction of sediment transport and all associated processes. Roughness is also a dynamic feature (Wright, 1993; Wheatcroft, 1994), therefore the temporal manifestations of morphology should be considered in addition to static spatial aspects.

Attempts to characterize seafloor roughness have focused primarily upon large-scale roughness features, on the order of hundreds of meters to kilometers (Fox and Hayes, 1985; Malinverno, 1989; Herzfeld et al., 1993). The roughness model of Fox and Hayes (1985), based upon large-scale features, has been shown to be applicable at small scales (centimeters to <1 meter), but others have only suggested the possibility of extension of large-scale models to small scales.

The capability to accurately extrapolate mathematical models of seafloor geometry, composition, and erodibility is important since the acoustic devices used to map the seafloor have limited resolution. These empirically-derived models have spatial scale ranges for which they are suitable, outside of which their suitability must be assumed. If macro-scale roughness characteristics can be determined from large-scale data, then there would be no need to directly examine their characteristics. Larger areas can be mapped using lower resolution data, therefore if model extrapolation was valid mapping could be done more economically since knowledge of features at one scale would be sufficient to determine characteristics at other scales. Quantification of seafloor roughness at micro-scales to macro-scales in different environments is necessary to test the utility of model expansion by the establishment of spatial-scale similarities in the seafloor and the processes which influence its structure. Flow-dynamic and material transport models are also limited to particular conditions and scales.

In addition to modeling roughness for mapping efforts, roughness characterization is important to studies of benthic boundary layer flow. Form drag and skin-friction drag both depend upon seafloor roughness element morphologies, though each relate to different scales of morphological variability and configuration. The scaling aspect of roughness elements has been related to geologic and sedimentary processes (Fox and Hayes, 1985; Malinverno, 1989) at large scales, whereas at macro scales surficial geological facies provides an overall limit to scaling properties of roughness elements, being directly related to wave and current induced flow dynamics (Wiberg and Harris, 1994; Robert and Richards, 1988). However, biological contributions to seafloor roughness features also become increasingly significant at diminishing scales (Grant and Madsen, 1986; Wheatcroft, 1994; Wright, et al., 1987; Wright, et al., 1997), tending to superimpose nearly random roughness features over more regular features of physical origin. Biological roughness has been characterized in terms both independent of and integrated with physical roughness character. The complexity of biologically induced seafloor roughness features can hinder accurate model parameter estimates and add variability to roughness measures.

This study provided several distinct quantitative measures of geometry and spatial character of micro-scale (0.5 to 150 mm) integrated physical and biological seafloor roughness features across the continental shelf of the Eel River Basin, California. For references on the study area, see the special issue of *Oceanography* (Volume 9, Number 3, 1996) devoted to STRATAFORM. Fractal, spectral, and geostatistical measures were applied to high resolution sediment profile imagery of the seafloor sediment-water interface to produce microtopographical roughness measures which integrally characterized physical and biological processes. Since physical and biogenic roughness features may be distinguished qualitatively, this study also sought to distinguish measures of roughness in terms of their ability to discriminate feature origin.

Seafloor Roughness

Micro to Macro-scale

Seafloor roughness height has the designation, k . The characteristic height, k , typically depicts Nikuradze, or grain, roughness. Grain roughness, k or k_d , bed configuration heights (or ripple roughness), k_{br} , and biological roughness, k_{bi} , compose total roughness height k_b (Wright, et al., 1997).

Roughness height measurement depends upon how height distributions of local microtopographical roughness elements are characterized. For a given area of the seafloor, several distinct estimates of each parameter would be plausible because of the directionality or spatial variability in the roughness height distributions. Unless all elements and bottom configurations are uniform and isotropic, they will not lead to the same determination of roughness height. Thus, k , may be most accurately determined as a regionalized variable, or in terms of spatial correlations of values at different distance lags.

Several distinct approaches exist for depicting elevation distributions and roughness geometries. Typically, k is expressed using a traditional statistic of elevation heights such as the root mean square distance, standard deviation, or linear extrema, for aperiodic roughness elements. Periodicities in seafloor roughness, for example in cases of rippled beds, often are parameterized

as wave heights or amplitudes, wavelengths, or steepness ratios which combine height and length. For many boundary layer flow studies, k is expressed as a single number which expresses a linear combination of roughness element measures, considered sufficient to characterize the region of interest.

Unless biological roughness elements are the only contributors to bed roughness, k_{bi} , biological roughness, cannot be directly determined. Rather, k_{bi} must be estimated by manipulation of the apparent roughness determined by some form of the Prandtl-von Karman equation

$$\frac{u(z)}{u_*} = \frac{1}{\kappa} \ln\left(\frac{z}{z_0}\right) \quad (\text{Equation 1})$$

where u is time-averaged water velocity at some elevation above the bottom, z , and u_* is the friction velocity and κ is von-Karman's constant (approximately 0.4). The calculated apparent roughness, or roughness length, z_0 , is converted to predicted bed roughness, k_b , which is then separated into bedform or ripple roughness and biological roughness, k_{bi} , heights (Wright, pers. comm.). This seems to provide reasonable estimates of magnitude of organism-related feature heights (Wright, et al., 1997).

However, those height estimates for the biological features are only valid if the number is directly related to a characteristic dimension of the biogenic structures in terms of relating hydrodynamic characteristics (for discussion, see Vogel, 1994). Wooding et al. (1973) described a function to calculate roughness length directly from geometric properties of roughness elements as

$$z_0 = 2.04h\lambda\phi \quad (\text{Equation 2})$$

where h represents element heights, λ represents areal concentration of element as the quotient of frontal area and average horizontal area, and $\phi = (h/s)^{0.38}$ where s is a streamwise length of roughness elements (Paola, 1985). This may be translated to biological roughness as

$$k_{bi} = 61\eta\beta\left(\frac{\eta}{\lambda}\right)^{0.38} \quad (\text{Equation 3})$$

where η represents element heights, k_{bi} represents biological roughness, and β represents element density, using the relationship $k_{bi} = 30z_0$ (Wright, 1995). Although other direct parameterizations are possible, Equations 2 and 3 are empirical derivations. The validity of Equation 3 from Wooding et al. (1973) and Paola (1985) extends at least to equilibrium bed ripples, as shown by Grant and Madsen (1982).

Organisms' shapes may not be well defined by simplified geometric representations, and it is unlikely that only one type of organism would be present in any region. Therefore the choice of a formula used to directly estimate biological roughness should likely be based upon both the type of benthic organisms present and statistically-modelled geometric measures based upon samples of the constituents. Predictions of flow-derived apparent roughness estimates from geometrical formulations of biological roughness heights are not reliable using most *in situ* data.

Large-scale

Fox and Hayes (1985) examined large-scale seafloor roughness utilizing frequency-dependent expressions of roughness elements, employing frequency transforms to calculate power spectra. Briggs (1988) also applied power spectra to his study of microtopographical roughness of the seafloor of Dry Tortugas Bank, Gulf of Mexico, where biological roughness has been implicated as a significant factor determining seafloor configuration (Wright, et al., in press). Fractal measures have been applied by some investigators to describe roughness as well (Malinverno, 1989), though not without criticism concerning assumptions (Herzfeld, et al., 1993). Geostatistical techniques, such as semivariogram analysis, has been used by Herzfeld (1989), Malinverno (1989), and Herzfeld et al. (1993) to determine the spatial variation and scale-related variation patterns of roughness for large-scale seafloor features (fracture zones, spreading centers, and sedimentary slopes and plains), and by Robert and Richards (1988) to examine macro-scale bedform geometry. Variogram or semivariogram analysis can also be used to determine the scaling behavior of a process (Journel and Huijbregts, 1978) or whether a process is scale-dependent or scale-invariant (Herzfeld et al., 1993).

The apparent fractal structure of the seafloor has been observed by several researchers and used to describe roughness or roughness zones in terms of fractal dimensions or fractal measures (Barenblatt et al., 1984; Arakawa and Kratkov, 1991; Malinverno, 1989; Herzfeld et al., 1993). Fractal geometry, fractal models, and fractal measures have been increasingly applied with abundant supporting theory (Mandelbrot, 1983; Taylor, 1986) in many fields, especially those considering natural surfaces (e.g. Pentland, 1984; Pfeifer, 1984; Yokoya et al., 1989), which are generally considered random fractals. True, or deterministic, fractals result from fixed iteration functions which describe a process indefinitely, across all scales, whereas random fractals result from the incorporation of stochasticity into the iterator (Pietgen et al., 1992). Natural surfaces may approximate random fractals, however they are bound by scale limits at some point (Pfeifer, 1984; Russ, 1994).

Application of fractal measures, or calculation of fractal dimensions, requires the assumption of scale-invariance for a process, also called self-similarity, although some measures assume only self-affinity, or weak scale-invariance (Russ, 1994). Seldom is this assumption tested (Herzfeld et al., 1993), although determination is relatively straightforward for one or two dimensional datasets. Self-affinity may be thought of in terms of how rescaled, or magnified, portions of the original object appear in relation to the original. Self-affine objects, magnified will resemble the original, but will be distorted by a fixed factor on one of the coordinate axes. For a more thorough explanation, see Mandelbrot (1983) or Pietgen et al. (1992).

Determination of the scaling behavior may be made by visual inspection of the semivariogram calculated for actual data representing a line or surface (Herzfeld et al., 1993). For distributional properties, Loehle and Li (1996) have described an information fractal dimension which directly incorporates the spatial manifestations of variables in the calculation of the dimension. Loehle and Li (1996) also discuss the potential statistical properties of fractal measures including sampling and estimation. Fractal measures, or fractal dimension estimates, directly and concisely relate the relative roughness or heterogeneity of a process within the bounding

topological dimensions (Hastings and Sugihara, 1993). Fractal measures are not applied here to describe the general fractal nature of the seafloor formed by a definitive process. There are several realizations of fractal dimensions whose measures rarely agree and whose statistical properties have recently been tested and reviewed (Cutler and Dawson, 1990; Ramsey and Yuan, 1990; Theiler, 1990). Fractal measures are applied in this study because of their utility as single-number parameterizations of roughness which integrate different configurations of heterogeneity, and because of their relationship to some of the other, more common, roughness characterizations such as Fourier spectra.

STUDY AREA

This study was part of the STRATAFORM program (Nittrouer and Kravitz, 1996; Wiberg, et al., 1996; Wheatcroft, et al. 1996; Syvitski et al., 1996; Pratson, et al., 1996; Austin, et al., 1996; Goff, et al., 1996; and Steckler, et al., 1996) which was conceived to advance understanding of stratigraphic sequence formation on continental margins by interdisciplinary examination of sedimentary structures and processes (Goff et al, 1996). A sediment profiling camera and surface camera system was deployed December, 1995 from the R/V Pacific Hunter along an irregular transect offshore from Eureka, CA (**Figures 1 - 2**) from N 40° 51.668' W 124° 12.727' to N 40° 57.801' W 124° 16.927'. The sediment profile images I used to quantify microtopographical roughness elements of the seafloor were acquired primarily to document the recent depositional stratigraphic record in the surficial sediments.

The Eel River margin is a flood-deposit dominated, high-energy, narrow continental shelf off the northern California coast, extending approximately from Cape Mendocino to Trinidad Head (Wheatcroft et al., 1996). The continental shelf in this region is relatively smooth in geologic and acoustic terms (Goff et al., 1996).

The cross-shelf study transect traversed sands to marine muds in water depths from approximately 28 to 83 m, and included the primary depositional area where sediments transported offshore by Eel River winter floods settle (Wheatcroft, et al., 1996).

In the vicinity of the study region, Wheatcroft (unpublished) has recently surveyed benthic communities as part of the STRATAFORM project. These data are not yet available. Previously, benthic fauna was surveyed by Pequegnat et al. (1990) near the SPI study transect in 18 to 73 m water depth. They reported that benthic numerical and biomass dominants were polychaetes, and that dominant species were different in shallow and deep water zones. Most of the infauna from all taxa collected by Pequegnat et al. (1990) were small throughout the study area, an attribute explained by seasonal disturbance, presumably by flood deposition but perhaps also by high energy winter storm effects upon the substrate. The majority of the dominant polychaetes found

were subsurface deposit feeders. Some large nephtyid and lumbrinerid polychaetes were occasionally observed in contrast to the many small animals.

The benthic biological community of the Eel margin was studied by Lissner et al. (1989) in deeper water (100 to 600 m). They showed that the Eel River continental shelf region is biologically distinct from other shelf regions along the northern California coast, possibly because of the sediment-type differences between the regions. The biological community also showed cross-shelf differences which appeared related to sediment-type. The community was composed mainly of burrowing, deposit-feeding infaunal polychaetes found in highest abundances at the deeper sites (Lissner et al., 1989).

METHODS

Sampling

Sediment profile images and plan-view surface images were acquired from ten stations. The camera system was deployed five to six times at each station (**Table 1**). Time and position was automatically recorded for each separate deployment. Five good profile image sets (two were taken during each deployment) were obtained from nine of the ten stations. Only one profile image was acquired from Station 9. Sediment surface images were taken during each system deployment; however highly turbid near bottom waters were encountered over most of the area, rendering bottom features indistinguishable. The profile camera system is self-contained and therefore not subject to turbidity, so that all the sediment profile images were clear. Several of the sample sites were near the locations where the V.I.M.S., the University of Washington, and the USGS had, or were planning to deploy tripods to measure benthic boundary layer flow and transport phenomena (Wright, et al., in press) (**Figure 2**).

Sediment Profile Imaging (SPI)

Mechanics

The sediment profile camera is a specialized remote underwater still camera system (Rhoads and Cande, 1971). For this study a Benthos model 3731 was used. The camera system is designed to provide an *in situ* image of the sediment-water interface and subsurface 22 cm of sediment with unparalleled detail. It consists of a large stainless steel frame structure, within which a cradle supports the camera attached to a water filled prism angled at 45 degrees is able to move vertically independent of the frame. The camera views the sediment through a Plexiglas window in the prism by means of a mirror. The prism penetrates into the bottom, slicing downward through the sediments by means of a sharpened blade edge. The camera was modified to take two photos at adjustable delay and timing. One photo was taken 8 sec. after bottom contact and the second after 15 sec. Clear images are acquired irrespective of bottom water turbidity because the prism is filled with clear distilled water and sealed from ambient water.

Profile Images and SPI Analysis

In addition to revealing recent subsurface sedimentary stratigraphy (**Figure 3**) and undisturbed sediment-water interface features, the profile images also display features which relate the degree and depth to which the surficial sediments and strata have been reworked by benthic organisms (Diaz et al., 1994) as seen in **Figure 4**. Surface-layer relative consolidation can be determined directly from profile images as well since unconsolidated surface sediments have visible pore spaces between grains or aggregates (**Figure 5**).

Standard sediment profile image (SPI) analysis (Rhoads and Germano, 1982 and 1986; Diaz and Schaffner, 1988) of sediment profile images allows sedimentary regimes and benthic habitats to be classified in terms of functional community parameters which corroborate habitat characterizations made using traditional benthic methods (Bonsdorff et al., 1996).

Approximate sediment grain size was estimated from the original SPI slides. Grain size is directly measurable for grains approximately > 0.25 mm. Below 0.25 mm grain size was estimated based upon visual textural characteristics of the sediments. Sediments were categorized initially into descriptive classes, then converted to sizes using the Wentworth-Udden scale (Folk, 1974). The relative degree to which the sediments in profile images were bioturbated, estimated as the overall extent to which biological features dominated sedimentary structures based upon a combination of mottled areas, burrows, tubes or infaunal feeding void structures, and the actual visible presence of organisms, was classified into five categories (none, trace, low, moderate, and high) from sediment profile images. Bioturbation categories were parameterized (0, 0.1, 1, 2, and 3) for inclusion in multiple regression models. The non-uniformly spaced ordination categories were chosen to represent the apparent degree of bioturbational because the nominal categories represented visual estimations of proportional amount of sediments reworked. These proportions could only be visually relegated to crude percentage coverings. The entire sediment image area viewed represented 1, and the approximate proportion of sediments reworked were 0, $<1/10$, $1/4$, $1/2$, $3/4$; representing the range of bioturbation observed. If all the viewed area were bioturbated,

an additional class called "total" and parameterized 1 would have been included. The trace, or 0.1 category might be considered negligible bioturbation. This classification scheme could be reduced to fewer classes easily, however initially it was desired to enable as much discriminatory resolution as possible.

Sediment mixing depth was estimated as the deepest extent to which evidence of recent biological activities was seen. This generally included depths of active and oxidized infaunal burrows, open feeding voids, organism presence, and sometimes mottling. The difference in elevation extrema for the sediment-water interface observed in the profile images was measured and recorded as surface relief. Correlations and multivariate models were constructed in an attempt to account for some of the relationships and variability in the measures using several environmental and benthic habitat parameters determined from the sediment profile image analyses.

Data Source

Microtopographical seafloor profiles obtained from sediment profile images using digital image processing and two dimensional signal processing techniques, were used to calculate a variety of roughness measures. Some of the roughness measures applied have been commonly used to describe macro-scale roughness, others were adapted from measures applied previously to large-scale seafloor morphology. It is important that all scales receive similar measures if comparison and extrapolation of concepts is to be accomplished.

Digital Image Storage and Processing

Digitization was done at 1100 by 1500 pixels per slide image using a Canon Fiery Scanner model 200i. Images were initially stored as RGB color mode, 8-bits per color plane, encapsulated post-script (EPS) format with no compression.

Unaltered digitized images were analyzed visually for standard biological and physical sediment parameters. Image feature measurements were made using NIH Image version 1.58 (for Apple Macintosh computers). Image length scales were determined based upon total 15 cm width of images. The number of pixels per 15 cm total image width was applied to calibrate image

feature measurements. Color plane curves, or the transfer function which controls the intensity levels of the individual or combined color planes which compose an RGB image, were adjusted during visual analysis to increase hue differences and allow visual detection of features difficult to discern. Color adjustments were consistent among similar sediment profile images.

Sediment-Water Interface Profile Contour Extraction

In order to apply roughness measures, the sediment-water interface profile contours had to be extracted from each image as a single continuous line. This was done manually and using spatial and frequency domain automated processing routines. In order to apply the frequency domain processing routines, the images were initially cropped from 1100 pixels wide to 1024 pixels wide, so that Fast Fourier transforms could be applied without altering the data series. For manual traces, the 1024 pixel wide images were interpolated to twice the magnification to produce 2048 pixel wide images. Interpolation was done using Adobe Photoshop for MacOS. Visual comparisons of interpolated and original images showed no significant alteration of small image features.

Manual tracing of 2048 pixel images

Sediment-water interface (SWI) profile contours were traced from digitized sediment profile images. Adobe Photoshop for MacOS running on an Apple Macintosh 7100/80 was used for the manual extraction of the SWI contours from images. Digitized SPI images were overlain with a transparent digital image layer which could be used to store the trace done using a mouse-controlled single pixel wide pen tool. Contours were traced from the 2048 pixel wide images. The image or the transparency layer could be viewed together or individually temporarily by displaying one or the other in order to confirm the accuracy of the trace. **Figure 6** displays an example trace overlaid on the original image.

Automated image processing routines

Digital image processing techniques allowing automated extraction of the sediment-water interface from digitized profile images were developed, although the interface contour may be

traced manually, consistency would be maintained if image processing routines were available to treat each image systematically.

Spatial domain processing

Sediment profile image processing for automated interface extraction (processing performed using Adobe Photoshop with the Image Processing Toolkit Plug-in modules) are demonstrated in **Table 2**.

Frequency Domain Processing

Applying a two-dimensional Fourier transform to images produces a wave-number domain image representing the image's wave-number spectrum. The gray scale intensities in this image represent the magnitude of the component wave-number, the distance from the origin represents the wave-number, and the polar angle represents orientation (see Russ, 1995). Segmenting the FT image is an operation involving selection of a grayscale range, deletion of all values outside the range, and thresholding the values within the range which sets them all to a single value. What this accomplishes is a filter mask which can be convolved with the two-dimensional FT image, or multiplication of the selected wave-number components by the chosen filter function and multiplying all other wave-number components by zero. After convolution, the inverse Fourier transform is applied, and the image produced returns to the spatial domain.

The wave-number components retained during the transformation and convolution will result in a modified spatial domain image. If low wave-number components are retained, blurring of major features results, and detailed feature variations are eliminated. This approach is utilized in the wave-number-based (or frequency-based) edge-finding techniques applied to images in this study. Segmentation by thresholding was done at a constant intensity level value in order to consistently apply the process to all images processed by the technique. This consistency in processing often resulted in inaccuracy of SWI selection since distinct surface morphologies and sediment types led to different wave-number spectra patterns.

After the inverse FT was applied, histogram stretching was applied or image pixel-neighborhood variance was calculated from the low- and high-pass filtered image, resulting in an image with grayscale values corresponding to the magnitude of variance within local pixel region. Thresholding the variance image increased contrast of the high variance areas and produced a binary image emphasizing the primary edges visible in the original image. Erosion operations removed macro-scale features and narrowed the edge range width. Skeletonization of this image produced a line representing the sediment-water interface profile contour. These steps are described in **Table 3**. The extracted SWI contour line was sometimes multivalued (**Figure 7**) because of subsurface or surface discontinuities which appeared very much like the sediment-water interface discontinuity. However, that line image was processed to produce a single-valued, piecewise continuous contour function (**Figure 7**) as were the original traced images so that one-dimensional signal processing could be applied to estimate roughness measures after satisfying Dirichlet conditions. This was done using NIH Image macro programming.

Imaging the sediment water interface

Traced sediment water interface (SWI) contours were used for the analyses since the traces always resulted in the most detailed and accurate depiction of the interface, whereas the automated routines often required excessive smoothing of the SWI contours in order to achieve continuity. Tracing was undesirable for many reasons, however, including subjectivity, mechanical limitations, and speed of implementation. The automated image processing routines overcame these problems at the expense of slightly less detailed data, except for small portions of the surface where the SWI variability is high or the image background is of high contrast. Edge finding is a frequently applied image processing routine, and many filters exist which accomplish the task relatively well. Edge features, however, can be difficult to separate if surrounded by like intensity or hue regions. If pixel intensities, hues and saturations are nearly the same on either side of a faint edge, none of the methods available are alone likely to accomplish successful edge-extraction. The processing routines applied included combinations of techniques which exploited image

attributes of the SWI. The spatial domain processing routine used filters and image combinations which contrasted the regions of highest local variation in pixels (**Table 3**). The spatial domain processing was successful for most of the images, but in some cases confused the SWI with subsurface discontinuities.

The frequency domain routine was less successful for a variety of images because of the way edge features were represented in the frequency domain. In the frequency domain a well-defined edge feature was represented by all frequencies, evident as the dark vertical line in the FT image (**Table 3**). The FT mask filter included a white vertical line which eliminated all those frequencies in the spatial domain at an orthogonal orientation, affecting any pronounced horizontal edges which separated the image from background fill. Less well-defined edge features in the images were not visually distinct in the FT image. The frequencies and orientations which described them are scattered throughout the FT image, and thus edge detection based upon frequency domain processing required elimination of the very low and middle frequency bands and enhancement of the low and high frequency bands. This can be seen in the structure of the FT mask filter (**Table 3**) where the lowest frequencies are represented by the center of the image and become higher with distance from the center. The dark annuli represent the frequencies which were retained across all orientations and the light annuli represent the frequencies which were eliminated. Although this processing was uniform and always enhanced the SWI, sometimes the enhancement was insufficient to provide enough contrast to immediately extract the SWI feature via thresholding operations, so that additional spatial domain steps would be necessary. The main problem involved the noisy sediment features which also would be enhanced by the processing. The heterogeneity of the subsurface sediments, biological features, and unconsolidated surface sediments all had aspects which resembled the SWI. The resultant image features may confound the automated extraction of an accurate SWI, however they also promise to provide a basis for additional integrative measures of biological sediment mixing applicable to sediment profile images and X-radiographs.

Roughness Measures Applied to Extracted Interface Contours

Images with SWI's which appeared to have been disturbed recently by mechanical forces were measured, but not included in later analyses. They were excluded because possibility of disturbance by the camera system impacting or dragging across the bottom could not be ruled out. Only two images were excluded for that reason.

Descriptive Statistics

Vertical linear extrema (surface relief) were calculated from digital image analysis data produced using NIH Image on a Macintosh 7100 computer (version 1.61: developed at the U.S. National Institutes of Health and available on the Internet at <http://rsb.info.nih.gov/nih-image/>) and standard deviations were calculated for SWI profile contours converted to scaled x, z values. Standard deviation (SD) is the same as root mean square (rms) when the predicted value is the mean of the series using

$$SD = rms = \left[\frac{\sum_{i=1}^n (Z_i - Z_i^*)^2}{(n-1)} \right]^{0.5} \quad (\text{Equation 4})$$

where $Z^* = \text{mean}(Z) = \text{predicted}(Z)$, and n is the number of observations. *Geostatistical Analysis Semivariogram*

The semivariogram technique measures spatial continuity and characterizes a variable's spatial behavior, as do the covariance function and power spectral density (Herzfeld, et al., 1996). The semivariance, $\gamma(h)$ used to construct the semivariogram (experimental variogram), may be calculated using

$$\gamma(h) = \frac{1}{2n} \sum_1^{n-h} [z(x_i) - z(x_{i+h})]^2 \quad (\text{Equation 5})$$

where h represents the spatial or temporal lag, or distance between successive data, which is incrementally increased by units i through the number of datapoints n (Journel and Huijbregts, 1978; Herzfeld, et al., 1993). The variogram of a function simply represents $2\gamma(h)$ for all h.

Semivariograms are generally described using one of a few basic models types or a combination of the basic models. The most commonly applied models are linear, parabolic, exponential, or some combination of those (Journel and Huijbregts, 1978; Davis, 1986). Semivariograms were calculated, using *Surface III+* for MacOS (Copyright Kansas Geological Survey), for sediment-water interface contours converted to scaled x, y, z values, where y values were set to zero, and were calculated for only one coordinate direction.

Semivariogram Components

Three primary components which relate the spatial continuity of the process examined may be observed in a graph of the semivariogram function. The nugget, the slope or shape, and the sill of the semivariogram describe the spatial variation of a process if the process exhibits second-order stationarity, in that the variance depends only upon the lag, or a weaker form of second order stationarity defined by the intrinsic hypothesis (Journel and Huijbregts, 1978). The nugget occurs as a y-axis intercept value which exceeds zero, and represents the lower resolution limit of the data as the variance at the smallest lag possible between data intervals, the lag being the spatial or temporal interval between data points. The slope or shape of the semivariogram represents the rate at which the variance of the data increases with increasing lag. The sill represents the observed sample variance of the process or data set, its limit being the population variance which would represent exhaustive data. A standard semivariogram appears in **Figure 8** with components depicted. Semivariance is inversely related to autocovariance and autocorrelation as shown in **Figure 9**. A few basic models or combinations of them are used most often to describe the observed semivariance (**Figure 10**).

Determination of Scaling Properties

The scaling property of a process may be determined directly from semivariogram. Self-similarity, self-affinity or scale-dependency will be evident in the shape and scale of the graph (Herzfeld, 1989). If the semivariogram displays a form which is mean-square differentiable at the origin, it represents strong or weak scale-invariance (**Figure 11**). Strongly scale-invariant, or

self-similar processes should have linear semivariograms, and weakly scale-invariant, or self-affine processes will result in approximately parabolic variograms or power law variograms at the origin (Cressie, 1993). Scale-dependent functions will result in a semivariogram which reaches a sill value and then decreases, possibly followed by periodicity or aperiodic cycling (Herzfeld, et al., 1993) (**Figure 12**).

Malinverno (1989) demonstrated that the seafloor possesses self-affinity for certain scales, however Herzfeld et al. (1993) contradict this observation, claiming that the seafloor possesses scale-dependent spatial structures which exhibit scaling behavior requiring more complex explanatory concepts, but also that the Hausdorff dimension does exceed the topological dimension for the seafloor, thereby possibly allowing the designation "fractal." These studies, however all consider the seafloor on very large scales, kilometers to hundreds of kilometers, whereas the macro-scale features they hoped to model using knowledge about large-scale features have not been examined in this way. Although Herzfeld et al. (1993) convincingly show that seafloor morphology is scale-dependent overall, their data do display scale-invariance for certain distance lags.

Scaling behavior may also be determined by direct examination of the properties of magnified portions of the original process. For example, in **Figure 13**, the lower box is a 7X magnification of the smaller box which encloses a 2 cm wide section of the sediment-water interface contour. The width of the entire upper contour is 14.8 cm, and the subsection was enlarged to match that width. Comparing the magnified vertical relief to the unmagnified surface relief reveals a self-affine structure, where the vertical scale in the exploded view is too large after a 1:1 (x:z) magnification ratio. The magnification ratio should be approximately 1.5:1 to achieve statistical consistency between the original and close-up images. This departure from a 1:1 ratio is indicative of self-affinity rather than self-similarity (cf. Malinverno, 1989). For a self-affine or similar process or object, the magnification would produce similar statistics as well. In other

words, stationarity may be considered a criteria for self-similarity, however scale distortions may occur for some processes such as natural or random fractals and produce only self-affinity.

Fractal Measures

Increasingly, fractals have been used to characterize large scale seafloor properties (Barenblatt et al, 1984; Fox and Hayes, 1985; Malinverno, 1989) as well as micro-scale properties of sediment grains (Frisch, et al., 1987) and as their functionality for describing natural surfaces has been realized (Mandelbrot, 1983). Fractal dimensions are efficient, single number parameters which characterize roughness and may be calculated for lines, surfaces, or volumes which are not easily defined or depicted in Euclidean geometrical terms or by trigonometric function approximations such as those employed by spectral techniques. Some fractal analysis techniques require the assumption that a function possesses self-similarity, or scale-invariance which is a property of ideal fractals, while other fractal techniques are suitable to functions or objects possessing only self-affinity (deemed random fractals), exhibited by most natural surfaces, including the large-scale (1 - 100 km) marine benthic landscape (Malinverno, 1989) and the sediment-water interface (0.1 - 150 mm). The semivariogram analyses applied revealed that the sediment-water interface in all profile images collected exhibited self-affinity over some length scale, typically up to 5 cm, though scale-dependency existed at scales of >5 to 15 cm. Fractal measures are applicable, however, for the scale ranges over which self-affinity exists (Russ, pers. comm.).

Several different, but related, depictions of dimension are commonly generalized as fractal dimensions (e.g. topological dimension, Hausdorff dimension, Minkowski dimension, self-similarity dimension, box-counting dimension, Euclidean dimension). All are attempts to explain the relationship between length, surface, or volume and scale by a power law containing a non-integer exponent. Fractal curves, for example differ from Euclidean curves in that a Euclidean curve length will approach a finite limit as step length (measurement) approaches zero (Russ,

1994) whereas a fractal curve length will continually increase, as step length approaches zero, according to a power law.

A basic fractal depiction or measure of a line will reveal that length varies with measurement scale except for smooth, or ideal Euclidean, curves, however the variation in length is dictated by the structure and scaling properties of the fractal line such that a dimension for the line may be calculated by several methods. The most basic relationship between scaling and precision may be expressed as

$$a = \frac{1}{s^D} \quad \text{(Equation 6)}$$

where a represents the number of scaled pieces, s represents scaling factor, and D is the fractal, or topological, dimension depending upon the object described (Pietgen et al., 1992). The rearranged log form of this relationship can be expressed as the similarity dimension, D_s , by

$$D_s = \frac{\log a}{\log(1/s)} \quad \text{(Equation 7)}$$

(Peitgen, et al., 1992) using the variables as above. Subscripts for D typically denote the particular dimension or measure used by the first initial of the name. The relationship expressed by Equation 7 is equivalent to the box-dimension, D_b , for self-similar objects when a is changed to $N(s)$ which represents the number of squares with side-length s intersected by a curve (Pietgen et al., 1992). The compass dimension, D_c , is sometimes used to represent the Hausdorff dimension, D_H , and can be estimated using the relationship

$$D_H = D_c = 1 + d \quad \text{(Equation 8)}$$

where d represents the slope of the line on a log-log plot for total length versus precision, or $1/s$, where s represents stride length or divider width, sometimes called the Richardson plot method of calculating the fractal dimension. Readers interested in the detailed set theory basis for the Hausdorff dimension are referred to Mandelbrot (1983) and Pietgen et al. (1992). The Minkowski dimension, D_M , which is calculated from the slope of a log-log plot of coverage area to coverage perimeter, where a coverage consists of a set of circles centered along every point on the line process (Russ, 1994). The relationship between the perimeter and area of the coverage as the

circles increase in diameter determine the slope and the dimension estimate. Implementation of the Hausdorff measure is common, and existing computer code was used for the calculation. The Minkowski dimension, likewise was able to be calculated using previously existing code (*Fractals* for MacOS, Russ, 1994) and by imaging macros (NIH Image fractal macros: available at <http://www.cee.cornell.edu/~mdw/fractech.html>). Both these fractal measures were implemented directly upon the sediment-water interface contours extracted from the SPI images using image processing and analysis software for the MacOS (NIH Image, and Adobe Photoshop with the Image Processing Toolkit Plug-in modules).

Theoretically, all fractal dimensions should express nearly the same value, however because they are implemented as measures upon discrete datasets, they do not. Different fractal measures approximate the theoretical construct to different degrees of accuracy.

Demonstration of Fractal Measures Using Fractal Lines Generated from Known Parameters

In order to demonstrate the information conveyed by fractal dimensions, or measures, several fractal lines were generated (**Table 4**) with known iteration parameters using *Fractals* for MacOS (Russ, 1994), and fractal dimension estimates were calculated. The fractal dimensions for fractal lines range from 1 to 2, non-inclusive, and higher values correspond to increasing complexity or roughness, as can be seen by comparing the lines in **Table 4**. Midpoint displacement iteration technique was chosen to generate the lines, since a single parameter, alpha, defines the degree of roughness with this method. Alpha is inversely related to the dimension measure value. Theoretically, for an alpha of 0.9, such as that used to generate, the fractal dimension will be 1.1. However, considerable variation exists in the actual measure of fractal objects (**Table 4**). This stems primarily from the means by which the dimensions, or measures, are calculated. Most of the measures rely upon some least-squares fit function, generally a slope, to incrementally increasing areal or volumetric covering or step-length sum of measure for a dataset. Errors in estimates are inevitable, but may be quantified, as reported by the "Fractal Surfaces" program. Also important is that the different measures do not produce the same exact

estimate. This is discussed in detail in Russ (1994) as are the conditions under which each of the fractal measures are applicable. Loehle and Li (1996) discuss the statistical properties and distributions of fractal measures.

Table 5 summarizes the information presented in Russ (1994), which describes necessary assumptions for each measure. Most of the assumptions relate to the scaling behavior of the process, generally whether the process is self-similar or self-affine. Scaling behavior of the seafloor profiles examined in this study was determined using semivariogram analysis, as described earlier.

Most of the seafloor profiles acquired using sediment profile imagery for this study could be described as generally smooth, comparable to fractal lines generated using midpoint displacement with $0.7 \leq \alpha \leq 0.9$. Few displayed the more extreme roughness such as that seen in the line generated using $\alpha = 0.5$. Using $\alpha = 0.5$ and midpoint displacement to generate a line should produce a profile which closely approximates random noise, or white noise, and a fractal dimension of 1.5. This is also closely related to actual fractal Brownian noise, which ideally has a fractal dimension of 1.5 (Pietgen et al., 1992) and a power spectra slope of -1. Power spectra slope relates to a fractal dimension as

$$D_{Fourier} = (4 + \beta) / 2 \quad \text{(Equation 9)}$$

where beta is the slope (Russ, 1994). $D > 1.5$ (i.e., $\beta < -1$) indicates that higher frequency variations are favored over lower frequencies, and a zero or positive power spectra slope, theoretically possible, but unobserved, would indicate higher magnitude variation at higher frequencies (Fox and Hayes, 1985), and also means a fractal Fourier dimension >2 for a line.

Description and Demonstration of Hausdorff Measure Implementation

The Hausdorff Measure may be calculated directly from digital images of disperse point sets, lines, or surfaces whose elevations are represented by image intensity values. The lengths of the measuring units to the overall length estimated for the curve are log transformed, and the slope of the log transformed data provides the Hausdorff Dimension estimate or Hausdorff measure

(**Figure 14**). The log-log plot is called a Richardson plot. Examples of the processing steps and details of the measurement technique are provided in Russ (1994, 1995). The Hausdorff Measure is applicable to self-similar objects (Russ, 1994).

Description and Demonstration of Minkowski Dimension Implementation

Calculation may be done directly from digital images of disperse point sets, lines, or surfaces whose elevations are represented by image intensity values. Minkowski coverages of the line or object are approximated either by erosion and dilation techniques or by the Euclidean Distance Map (EDM) transform (Russ, 1994). The EDM method was used in this study in addition to calculations made using the program "Fractal Surfaces." The EDM transforms a binary image, one with only black and white pixels where either the black or the white represent image features, into a grayscale image (Russ and Russ, 1989). The grayscale values in the new image directly represent the distance to the nearest feature in the image, therefore the features will be surrounded by bands of continually diminishing pixel values. Incremental areas of coverages and perimeters of coverages are measured. The slope of log transformed data produces the Minkowski Dimension (D_M). Example processing steps are shown in **Figure 15** and **Table 6**. The Minkowski Dimension is applicable to self-affine lines or objects (Russ, 1994).

Power Spectra Applied to Elevation Profiles

Fourier power spectra were calculated using the "Fractal Surfaces" program for piecewise continuous sediment-water interface contour profiles converted to scaled x, z values. Plots of the power spectra are presented in Appendix A.

Isotropy and Anisotropy

The profile camera system intersected the seafloor at varying azimuthal angles. Therefore, in locations where bedforms were encountered, some were imaged across ripple crests (**Figure 16**) and some nearly perpendicular to crests (**Figure 16**). Where no images revealed anisotropic bedforms, it was concluded that roughness was isotropic. The stations in the deposit area had isotropic roughness based upon this criteria. Characterization of the sediment-water interface was

conducted the same for isotropic and anisotropic roughness. Subsequent analyses were done assuming that the variances of data groupings was not influenced significantly by azimuthal angle of encounter with the bottom. No images were rejected from analyses because of particular orientation.

RESULTS

Benthic Habitat Characteristics

General description of sediments, evidence of depositional strata, fauna, biological structures, and roughness

Sediments along the SPI transect ranged from fine sands at the shallowest site (approximately 28 m water depth) to clay-silt at the deepest site (83 m) (**Tables 7 and 8**). Sand sediments at shallow sites all had surface bedforms, some symmetric and some asymmetric ripples. It was not always possible to determine wavelengths from the profile images since the prism window is only 15 cm wide, and often the image captured only part of the periodic structure or intersected it in a non-perpendicular orientation. Ripples which could be distinguished had wavelengths that averaged 10 to 15 cm, and heights of between 1 to 3 cm.

Infauna were visible in profile images from seven of the ten sample sites. The visible infauna were mostly small worms (< 1 mm wide), but a few large worms (>1 mm) were seen in images from Station 1 in 83 m water depth, and a large annelid or nemertean was visible in one image from 65 m. Epifauna on the sediment surface, within 1 to 2 cm of the prism window, were visible in profile images from six of the ten sites. Most were small gastropods (< 1 cm), but sea pens were evident in one image from the 28 m station.

Parameterizations by Water Depth, Sediment Type, and Biological Activity

Flood Deposit Layer Thickness

The thicknesses of the Eel River 1995 flood deposit were estimated from Wheatcroft et al. (1996) and from SPI images (**Figure 17**). The two estimates show good agreement. Where the SPI transect crossed the flood deposit, the two estimates of deposit thickness ranged from 0 to 5 cm. The deposit was thickest between 60 and 83 m. Three of the SPI stations (28 to 43 m) were inshore of the deposit layer.

Measured SPI Parameter Values

The parameter values obtained from analysis of the sediment profile images are presented in the following sections as mean (\pm standard error (SE)).

Apparent Color RPD

The average apparent color redox potential discontinuity (RPD) depth was greater in the sandy inshore sediments and less in sediments from 48 to 83 m water depth (**Figure 18**). Deepest RPD layer thicknesses were observed in images with fine sand to very fine sand sediments which occurred in the shallower water depths (28 to 43 m) (**Table 7, Figure 18**). Shallowest RPD depths occurred in the transition zone sediments where the substrate consisted of silty sand. RPD depths decrease with increasing water depth from 28 to 50 m, then increase with increasing water depth from 50 to 83 m.

SPI prism penetration

The overall mean prism penetration was 8.8 cm (\pm 5.4 cm) (**Table 7**). Prism penetration, which is associated with certain sediment mechanical properties, especially hardness and surface cohesion (Bokuniewicz et al., 1975), increased with water depth and distance offshore and was significantly correlated ($r = 0.97$) with sediment phi (**Table 7**), as well as depositional strata ($r = 0.94$) (**Figure 19**). That the number of strata correlated with prism penetration implies more than simply that more strata could be seen in images with deeper penetration depths. The maximum thickness of the most recently deposited layer, deposited in 1995, occurred in the 60 m depth range, at the latitude of the study area, while deepest penetration occurred at the station in deepest water.

Sediment Grain Size

Sediments encountered along the SPI transect ranged from approximately 0.3 mm diameter sands at the shallowest nearshore sites to 0.005 mm (approximate modal value) clayey silts at the deepest offshore sites (**Figure 20**). Grain size diminished nearly linearly with depth to 60 m, and

was constant at deeper depths (**Figure 20**). Mean grain size for all stations was approximately 0.09 mm (± 0.1) (**Table 7**).

Bioturbation and Sediment Mixing

Bioturbation was very low (trace) in the sand sediments, and increased from 48 to 65 m water depth, decreasing slightly at 83 m (**Figure 21**). Apparent biological sediment mixing depth was zero in the shallow water sandy sediments, and was indeterminate in images from the intermediate water depths, but rapidly increased from 4 to 12 cm with increasing water depth from 50 m and deeper (**Figure 22**) and with decreasing grain-size or varying sediment type (**Figure 23**). The indeterminate values might be translated to values of 0 cm.

Examination of parameters by flood deposit thickness

Figure 24 depicts several SPI parameters in relation to 1995 flood deposit layer thickness. Since deposit thickness varied non-linearly with water depth and distance offshore, this presentation elucidates patterns for some of the sediment characters related to the depositional processes. The apparent inversion of the trends in many of the parameters coincident with the 2 cm deposit thickness may result from the 2 cm class existing in the transition from primarily non-cohesive sand to partially cohesive silty sands. Apparent color RPD was deepest in non-deposit sediments (1.53 ± 0.16 cm). Within the deposit region, RPD depth tended to increase with increasing deposit layer thickness. Prism penetration depth was low in non-depositional sands and tended to increase with increasing deposit layer thickness, though deepest penetration (16.7 ± 1.4 cm) occurred in the 1 cm thick layer. The number of depositional layers tended to increase with increasing 1995 deposit layer thickness, ranging from an average of 1 (± 0) to 6 (± 0.5). The number of infaunal feeding voids increased with increasing deposit thickness, ranging from 0 (± 0) to 4 (± 0.6). The number of infaunal worms visible was zero in non-depositional sediments, and highest in the 1 cm thick deposit layer (4 ± 3). The number of burrows increased with increasing deposit, ranging from 0 (± 0) to 2 (± 0.4) per image. The number of infaunal tubes evident at the sediment-water interface tended to increase with increasing deposit thickness, ranging from an

average of $0 (\pm 0)$ to $0.3 (\pm 0.3)$ per image. The number of epifauna tended to decrease with increasing deposit thickness, ranging from an average of $1.3 (\pm 0.5)$ to $0 (\pm 0)$ (**Figure 24**).

SPI parameters were also examined in relation to the degree of bioturbation. Apparent color RPD was deepest in non-bioturbational sediments (1.47 ± 0.26 cm). In bioturbational sediments, RPD was deep where bioturbation was negligible (trace), shallow in low bioturbational sediments, and then increased with increasing bioturbation. Prism penetration depth increased with increasing bioturbation. The number of depositional layers increased with increasing bioturbation. The number of infaunal feeding voids tended to increase with increasing bioturbation, though highest numbers of voids (3 ± 0.5) were present in moderately (category 2) bioturbated sediments. The number of infaunal worms visible was zero in non-bioturbational sediments, and tended to increase with increasing bioturbation, though highest (3 ± 2) in moderately (category 2) bioturbated sediments. The number of burrows increased with increasing bioturbation, ranging from $0 (\pm 0)$ to $2 (\pm 0.4)$ per image. The number of infaunal tubes evident at the sediment-water interface tended to decrease with increasing bioturbation, though peaking in sediments with low degree of bioturbation (0.3 ± 0.3). The number of epifauna tended to be low sediments which were low (0.2 ± 0.1), moderately (0.1 ± 0.1) and highly (0.3 ± 0.3) bioturbated, higher (0.7 ± 0.6) in non-bioturbational sediments, and highest (1.4 ± 0.7) in sediments with trace levels of bioturbation (**Figure 25**).

Sediment-Water Interface Spatial Analysis and Roughness Measures

Semivariance of microtopographical elevations

Most of the semivariograms (Appendix B) reveal the presence of scale-dependent structures for the 15 cm wide surface sections examined. All the semivariograms also showed approximately parabolic or power function, mean-square differentiable behavior at the origin to some lag (**Figure 26**). This behavior will be referred to as parabolic from here. On average, parabolic behavior existed up to 5 cm, and ranged from 1 to 10 cm. Greatest lags over which parabolic behavior was apparent occurred in shallow (28 m to 43 m) and deep stations (64 m to 83 m). Apparently

periodic waveforms or partial waveforms can also be detected in many of the semivariograms. This suggests either scale-dependent behavior of the SWI, in the form of bedforms or macro-scale biogenic roughness (Herzfeld, et al., 1993; Robert and Richards, 1988), or alternatively may represent fractal behavior.

The mean distance lag over which semivariance was parabolic was nearly constant across sediment types (**Figure 27**). No particular model seemed best suited to describe most of the semivariograms, except for the parabolic model from the origin to some lag. Some of the semivariograms exhibited periodic behavior beyond the range, while others approached the sill asymptotically.

Surface Relief

Overall mean surface relief was 1.44 cm (± 0.60 cm), ranging from 0.4 to 3.5 cm. Mean surface relief was highest at the shallowest sample site where fine sand ripples were present. Lowest surface relief was measured at two of the shallow sites with very fine sand sediments (38 and 42 m water depth) and at the 65 m water depth site which had clayey silt sediments (**Figure 28**).

Standard Deviation of the Sediment-Water Interface (SWI)

The overall mean standard deviation of the SWI (SWI SD) was 3.8 mm (± 0.3 mm) when sea pens in image 8-5 (28 m) were not included as part of the SWI, and 4.1 mm (± 0.4 mm), ranging from 0.25 to 16.1 mm when the sea pens in image 8-5 were included. Standard deviation of sediment-water interface elevation profiles were highest in shallow water depths, then decreased and increased twice as water depth increased. The depth related pattern of SWI SD was that of an inverse bimodal curve, or a "W" shaped curve approaching a trimodal function (**Figure 29**). The SWI SD was highest in sand sediments (4.3 ± 0.7 mm), and lower in both muddy-sand (3.7 ± 0.3 mm) and mud sediments (3.7 ± 0.4) (**Figure 30**). SWI SD was highest (6.0 ± 1.0 mm) where there was no bioturbation, lowest in sediments with trace (3.5 ± 1.1 mm) to low (3.3 ± 0.3 mm) levels of bioturbation, and slightly higher when bioturbation was medium (4.0 ± 0.7 mm) to high

(3.9 ± 0.6 mm) (**Figure 31**). SWI SD was highest (4.5 ± 0.6) in the 2 cm and 0 cm (4.3 ± 1.0) deposit thicknesses. There was nearly continual decrease in SWI SD with increasing 1995 flood deposit thickness, except for the high value in the 2 cm category (**Figure 32**).

Fractal Dimensions or Measures

The different calculated fractal measures behave similarly overall, and display a pattern somewhat inverse to that observed for standard deviation. The fractal dimensions were low at the shallowest sampled site, then increased to high values, then decreased to minimum values typically between 50 and 60 m water depth, then increased and decreased again in deeper water (**Figure 33**).

Hausdorff Dimension

The overall mean Hausdorff dimension was $1.22 (\pm 0.12)$, ranging from 1.058 to 1.52. Behavior in relation to depth: From 28 m to 43 m water depth, the Hausdorff dimension increased from $1.095 (\pm 0.014)$ to $1.44 (\pm 0.042)$, decreased to $1.12 (\pm 0.018)$ from 43 m to 55 m water depth, increased to $1.28 (\pm 0.022)$ from 55 m to 64 m water depth, then decreased to $1.22 (\pm 0.050)$ in 83 m water depth (**Figure 34**). Hausdorff dimension was higher in sandy sediments (1.26 ± 0.040) than muddy-sand (1.19 ± 0.016) and mud (1.19 ± 0.015) where values were similar (**Figure 30**). The Hausdorff dimension was highest in sediments with trace levels of bioturbation (1.29 ± 0.070) and lower in sediments with none (1.18 ± 0.051) low (1.18 ± 0.012), medium (1.21 ± 0.029) and high (1.19 ± 0.025) bioturbation (**Figure 31**). The Hausdorff dimension was highest in sediments with no flood deposit (1.29 ± 0.057), and tended to decrease with increasing flood deposit thickness, except for a marked increase where the deposit was 4 cm (1.24 ± 0.020) (**Figure 32**).

Minkowski Dimension

The overall mean Minkowski dimension was $1.22 (\pm 0.06)$, ranging from 1.072 to 1.56. From 28 m to 36 m water depth, the Minkowski dimension increased from $1.12 (\pm 0.020)$ to $1.36 (\pm 0)$, decreased to $1.16 (\pm 0.009)$ in 55 m water depth, increased to $1.28 (\pm 0.030)$ in 64 m water

depth, then decreased to $1.24 (\pm 0.039)$ in 83 m water depth (**Figure 35**). The Minkowski dimension was highest in sand sediments (1.23 ± 0.024) and lower in muddy-sand (1.22 ± 0.019) and mud (1.21 ± 0.013) (**Figure 30**). The Minkowski dimension was highest in sediments with trace (1.24 ± 0.040) and medium (1.23 ± 0.023) levels of bioturbation and lower in sediments with none (1.19 ± 0.042) low (1.20 ± 0.014), and high (1.21 ± 0.021) bioturbation (**Figure 31**). The Minkowski dimension was higher where the 1995 deposit was 0 cm (1.24 ± 0.035), 2 cm (1.24 ± 0.039), and 4 cm (1.25 ± 0.018) thick and lower where the deposit thickness was 0.5 cm (1.22 ± 0.018) and 2 cm (1.18 ± 0.014) thick (**Figure 32**). Minkowski dimensions for piecewise and multivalued profile contours were identical, or nearly so, for images from most depths. Minkowski dimension estimates for piecewise continuous SWI contours were lower than those for multivalued contours in deeper waters where sediments were muddy and cohesive allowing small overhanging features to persist (**Figure 36**). The Minkowski dimension calculated using NIH Image macros versus depth shows similar pattern to that of the dimension calculated using fractals, but lower values overall (**Figure 37**). The similar patterns in the different estimates for Minkowski dimension can be seen in **Figure 38**. Differences are likely due to the dilation techniques used by the imaging macros which employed isotropic Euclidean Distance Mapping in all directions rather than just along the horizontal which should be done for affine objects (Russ, 1994).

Power Spectra Slopes

The overall mean power spectrum slope was $-0.78 (\pm 0.18)$, ranging from -0.983 to -0.331 . The slopes of the power spectra for SWI contours tended to diminish in magnitude (become less negative) with increasing water depth (**Figure 39**: note negative scale) Between 50 and 60 m water depth, there was a marked diminishment and then increase in slope magnitudes. This corresponded to the latitudinal gradient between the stations clustered near 50 m water depth. Power spectral slopes converted to Fourier fractal dimensions versus water depth behaved just as

spectral slopes (**Figure 40**). Spectral slopes were highest in magnitude (most negative) in sand sediments (-0.86 ± 0.022) and diminished in magnitude in muddy-sand (-0.79 ± 0.064) and mud (-0.73 ± 0.044) sediments (**Figure 30**). Spectral slopes were typically lower magnitude (less negative) with increased bioturbation, and lowest in magnitude (-0.69 ± 0.069) in sediments with low bioturbation, and greatest in magnitude with no (-0.86 ± 0.028) and trace (-0.90 ± 0.035) levels of bioturbation (**Figure 31**). Spectral slopes were greatest in magnitude outside the deposit area (-0.85 ± 0.027) and where the 1995 deposit was 0.5 cm thick (-0.83 ± 0.039). Lowest magnitude spectral slopes were observed in the 1 cm thick deposit (-0.63 ± 0.13) and then magnitudes increased with increasing deposit thickness (**Figure 32**). Power spectra are included in Appendix A.

Comparison of traced and auto-extracted contour parameterizations

Some SWI contours from each method were tested to determine potential difference in results. Traced SWI contours resulted in higher roughness measure values than contours extracted by spatial-domain processing, which resulted in higher roughness measures than contours extracted by frequency-domain processing (**Table 9**). The higher roughness values were indicative of better representation of the actual surface since smoothing occurred in both of the processing routines in order to provide continuity for the SWI contour. For this reason traced contours were used for analyses.

Isotropy of micro-scale roughness

Comparison of parameters from cross-crest versus crest-parallel images

Certain roughness parameters were found to differ between replicate images from the same site which sampled isotropic roughness features at different angles. For example, the variation between surface relief measurements from images 8-3 (3.5 cm), 8-4 (2.8 cm), and 8-5 (2.1 cm) could not be attributed to the angle at which the camera intersected the bedforms since all were intersected cross-crest, nearly perpendicular. However, variation between surface relief measurement from images 7-1 (0.4 cm) and 7-4 (0.9 cm) were caused by parallel-crest and cross-

crest intersection with the bottom. The bedforms at Station 7 had very small heights (approximately 1 cm), and therefore the magnitude of the possible difference was limited. The camera system's orientation upon the bottom elsewhere was not considered because roughness feature configurations were more isotropic in appearance. Gross morphologies were equally apparent despite camera orientation angles. Although isotropy may sometimes be determined by directional estimates of fractal dimensions (Russ, 1994), object orientation appears to have limited effect upon the estimate of fractal dimension in some cases (Pentland, 1984). The micro-scale roughness features observed in sediment profile images appear isotropic across the study area based upon the variograms, even though the macro-scale features may not be isotropic.

Statistical tests comparing roughness measures grouped by habitat characteristics

In order to assess gross differences in the distributions of the roughness parameters (surface relief, standard deviation, Minkowski dimension, and spectra slope) in relation to habitat parameters of possible direct influence, they were grouped into deposit/non-deposit, and bioturbational/non-bioturbational sets and compared using nonparametric Wilcoxon / Kruskal-Wallis rank sums test. RPD depth ($p = 0.03$) was significantly lower in the deposit region, whereas number of voids ($p = 0.03$), biological mixing depth ($p = 0.04$), number of worms ($p = 0.02$), and number of burrows ($p = 0.03$) all were significantly higher in the deposit region. Number of tubes and number of epifauna were not significantly different across depositional groups. Power spectral slopes ($p = 0.046$) were significantly higher in bioturbational sediments, though surface relief, standard deviation, and Minkowski dimension were not significantly different in bioturbational sediments or in depositional sediments. The biological parameters were not tested for differences between bioturbational and non-bioturbational sediments because of their collinearity.

Multiple regression

Multiple linear regression models were calculated for untransformed, continuous interval values of the Minkowski dimension versus habitat parameters (sediment grain size, biological

sediment mixing depth, flood deposit thickness) and other roughness parameters (standard deviation, and surface relief) . Similarly a regression model was calculated for power spectra slope versus sediment grain size, biological sediment mixing depth, and flood deposit thickness, and surface relief. Standard deviation (cm) of the SWI, surface relief, biological sediment mixing depth, sediment grain-size and 1995 flood deposit thickness had a non-significant factor effect (at $\alpha = 0.05$) on the Minkowski dimension and on spectral slope. None of the habitat parameters chosen accounted significantly for variation in slopes of power spectra.

DISCUSSION

Habitat characteristics and the influence of Eel River flood deposit

The biological and sedimentological parameters described using standard sediment profile image analysis (Rhoads and Germano, 1982, 1986; Diaz and Schaffner, 1988) appear to vary in accordance with the sediment layer deposited from Eel River floods upon the continental shelf as estimated from Wheatcroft et al. (1996). In other words, the flood deposit appeared to influence sediment parameters detectable by SPI (**Figure 24**). Two major floods were documented in 1995 (Wheatcroft, et al., 1996) but were not differentiated by core sample analyses; the 1995 deposit refers to material deposited during all flood events from that year. Most SPI stations located in heterogeneous sediments which could be generalized as muds, showed signs of recent deposition, either as small light tan colored particulates in the surface layer (Wheatcroft, et al., 1996) or as a series of subsurface laminations, generally 1 to 2 cm thick extending to the bottom of the images.

The 1995 Eel River flood deposit thickness estimated from Wheatcroft et al. (1996) agreed well with the thicknesses determined from the profile images (**Figure 17**). Both estimates of deposit thickness reveal that the most recent layer thickness did not start until 50 m water, and increased in thickness to a maximum at 60 to 65 m. SPI estimates were greater than Wheatcroft, et al. (1996) for the 83 m station. The high degree of bioturbation may have homogenized the two uppermost layers and made them visually indistinct. Similarly, lower estimates based upon SPI in the 60 to 65 m range may have been a result of sub-lamina induced by geochemistry rather than different depositional events. What appeared to be two layers may have been only one layer undergoing early diagenetic processes. Alternatively, the two floods in 1995 could have resulted in deposits which were visually distinct and separable by SPI but not core analyses. Overall, the two independent estimates of the cross-shelf character of the flood were similar.

The SPI analysis was also able to clearly distinguish layer thicknesses from previous depositional events, therefore hindcasting of previous depositional volumes may be possible based upon coherent cross-depth strata thicknesses and some assumptions about compaction. The

episodic character of the deposition has apparently allowed infauna to persist, even thrive in the depositional region. The activities of the infauna were apparently responsible for the unconsolidated sediment surface layer in the deposit muds (**Figure 5**). As shown by Wright, et al. (in press), the presence of an unconsolidated layer in the muddy sediments of the deposit allowed boundary layer stratification by suspended sediment to partially suppress turbulence and bed stress. High bioturbational activities and large, deep infaunal structures resemble those of a near-equilibrium type community structure (Pearson and Rosenberg, 1978) in the areas with highest deposition.

Several of the parameters had distinctly different behavior in the flood deposits relative to the inner shelf sands (**Figure 24**). For example, the redox potential discontinuity depth (RPD) generally is directly related to sediment grain size and flow-induced diffusion of oxygen into the sediments and also to the intensity of biological sediment-mixing activities, and to surface roughness structures (Ziebis et al, 1996; Rhoads and Germano, 1986). Apparent color RPD values were significantly less ($p = 0.03$) between the flood deposit and sediments inshore of the deposit, when images from transitional sediments were excluded. RPD depth, however did increase nearly linearly with water depth within the deposit region (Figure 19), greatest at the deepest station, apparently related to bioturbational activities. In addition, the biological mixing depth and number of voids, infaunal worms and burrows all were significantly higher in the deposit region. Numbers of epifaunal organisms and biogenic surface tubes were not different between deposit and non-deposit regions. However, this is likely a result of the few number of epifauna and tubes seen overall. All these differences suggest that the geophysical forcings controls the distribution of habitat type and benthic community structure and function.

Spatial processes of the seafloor at micro-scales

The semivariograms (experimental variograms) showed no detectable nugget effect and resembled the form of a mean-square differentiable function at the origin, apparently best fit by a parabolic or power law variogram model. Therefore microtopographical seafloor roughness may

be considered scale-invariant for the lag range over which this form of the variograms was evident. The scaling behavior exhibited was weak scale-invariance, or self-affinity, rather than self-similarity. This scaling behavior applied to an overall scale range of approximately 0.1 to 5 cm. Vertical elevation profiles of the seafloor on the Eel Margin appear to be self-affine over limited distances, and scale-dependent beyond those distances.

Variation in the scaling behavior was likely related to orientation of the camera in relation to bed features in certain areas. Roughness features at some sample sites appeared isotropic, while at others, especially in shallower water, anisotropic ripples were present. Azimuth angle of the camera in relation to the bedform strike was non-uniform, therefore some images represent the bedform structures more than others from the same sites as demonstrated in **Figure 16**. The presence of periodic waveforms or partial waveforms which can also be detected in many of the semivariograms does not accurately portray the regions influenced by sand ripples, because the apparent periodicity represented in some semivariograms sometimes reflects biologically-derived structures or simply bottom heterogeneity. A wider prism may have represented bedforms better, and a continuous transect image may have allowed determination of the scaling behavior for features > 5 to 10 cm. A continuous profile image or other high resolution representation of surface features covering several meters of bottom could confirm whether seafloor roughness is actually a scale-dependent or a self-affine fractal process. Based upon SPI, it appears as though small-scale seafloor roughness may be best represented by a self-affine fractal process superimposed upon a scale-dependent periodic process.

Generalized biologically-influenced roughness in the area

Seafloor microtopographical roughness was not generally associated with the presence of fauna or biological surface structures since few were present in the SPI images. Thus, biological roughness, per se, was low, as was physical roughness in most of the images. Biological roughness should not simply be considered inconsequential because surficial structures or epifauna were generally absent. The structure of the surface layer can be strongly influenced by infaunal

organisms and their activities (**Figure 5**) as has been shown by Bokuniewicz et al. (1975) and Wright, et al. (in press). Thus, the microtopography of the sediment-water interface which appears physically structured may, in fact, be bioturbated and possess both macro-scale roughness features and microscopic variability, which may be attributed to the benthic faunal activities.

When present, the epifaunal were important to roughness, however in the study area low epifaunal densities limited their overall effect. A profile image from Station 8 (28 m of water) did reveal epifauna (sea pens) which extended far above the SWI. Several parameters were calculated with the sea pens included and excluded for comparisons which might elucidate effects of biological forms upon roughness measures (**Figure 41** and **Table 10**).

Subsurface sediments in much of the study area were highly bioturbated, so much so that evidence of depositional strata at some of the deepest water sites was nearly completely obliterated and indistinguishable because of mottling resultant of infaunal feeding and burrowing activities. Although surface roughness could be only indirectly linked to these biological activities, the evidence supporting the effects was strong. The types and numbers of infaunal structures present indicated a change in functional biological characteristics across the flood deposit region which may have influenced the surface morphology in different ways. The structures suggest a possible shift from surface deposit-feeding and filter feeding epifauna and small burrowing, scavenging infauna, to tube-dwelling surface deposit-feeding and deep burrow dwelling deposit feeding infauna and head-down excavating deposit feeders.

The sedimentary laminations, or strata, obvious in the images are consistent with the thicknesses reported by Wheatcroft et al. (1996) (**Figure 20**). Stations 2 (64 m) and 3 (60 m) exhibited the highest number of strata, and finest sediments, and also the highest number of infauna and subsurface biological structures (**Tables 7 - 8**). The roughness in this depth range is dominated by macro-scale features and is attributed primarily to benthic biology. These observations are consistent with Wheatcroft (1994), who described the rapid development of biological roughness features and erosion of physical roughness features in moderate flow

conditions. Bedforms would not be expected in the region of highest deposition because of the grain sizes present since the height and wavelength of flow-constructed roughness features is directly proportional to grain size (Wiberg and Harris, 1994). Inshore from the region of highest deposition, in 50 m of water or less, roughness features were well-defined sand ripples which were of greater magnitude than the biological roughness features, except when the sea pens were present.

The study area might be classified overall as possessing relatively smooth macro-scale roughness, where the standard deviation (SD) of the surface elevational features averaged 0.4 cm, the surface relief (extrema) averaged 1.4 cm, and the mean slope of Fourier power spectra (FPS) generated from surface elevations was -0.78 (1 SD = ± 0.18). However, at micro-scales, part of the area may be considered relatively rough, with combined roughness greatest in the very fine sand sediments and clayey silt sediments where the Minkowski and Hausdorff fractal measures are highest (**Figure 42**). If the data from the sampled sites with sand sediments are excluded from analysis, the fractal measures are more negatively correlated with the other roughness measures, thus where micro-scale roughness was high, macro-scale roughness was low and vice-versa. Bioturbational eradication of larger roughness features may be responsible, as described by Wheatcroft (1994). Wheatcroft (1994), however, examined changes in surface roughness at individual points over time, whereas this study examined several locations over only one time period. The timing of sampling however, coincided with a relatively calm period just prior to a severe storm period, and thus represented the end of a bioturbation cycle during which biological activities would have restructured surface morphology. Storms would then smooth small, high-frequency (high wave-number) biological roughness features (Wheatcroft, 1994) by bottom stresses induced by waves and currents (Wright, et al., in press) or erosion/deposition of sediments.

Spatial aspects of roughness

Semivariogram analysis provided a means to determine the spatial relationships and the physical characteristics of the roughness features (Robert and Richards, 1988), and corroborated the apparent reason behind the micro to macro-scale roughness measure differences. For example, the highest relief, SD, and FPS slopes were obtained at 50 to 60 m water depth, where there was some depositional layering, moderate to high levels of biological mixing activity, and sandy silt sediment. The roughness in this region is dominated by features on the order of 5 to 10 cm, as seen by the semivariograms from Stations 3, 10, and 4 (60, 55, and 52 m water depth). These sample sites exhibited many of the highest overall semivariances at lags of 5 to 10 cm, exceeded only by the nearshore sample sites where well-defined sand ripples were present. The 5 to 10 cm roughness features in the 50 to 60 m water depth range appear to be a combination of physical and biological reworking of material recently deposited from Eel River floods. The material in the 50 to 60 m range appears relatively unconsolidated, based upon the penetration of the sediment profile prism (**Figure 19**) (Bokuniewicz et al., 1975) and by the consistency of the strata thicknesses below the sediment surface.

The semivariograms show that, in general, broader macro-scale (5 to 15 cm) seafloor roughness is a scale-dependent process. However, all of the semivariograms showed parabolic behavior at the origin up to some distance lag. The semivariance resembled a mean-square differentiable function which indicates strong spatial continuity in the variable (Journel and Huijbregts, 1978), which may be interpreted as weak scale-invariance (Herzfeld et al., 1993). Thus, although seafloor roughness may be a scale-dependent process at 5 to 15 cm scales, and in general (over hundreds of km: Herzfeld et al., 1993), it may also be considered a scale-invariant process at scales below the ranges at which geological or physical processes form deterministic structures or extremely different topographical features. Therefore, microtopographical seafloor roughness (<0.1 to 5 cm) may be considered weakly scale-invariant.

The non-asymptotic behavior of the semivariograms after the initial apparent range has two possible origins. It suggests either scale-dependent behavior of the SWI, in the form of periodic bedforms or macro-scale biogenic roughness elements (Herzfeld, et al., 1993; Robert and Richards, 1988), or fractal behavior of the SWI. It can be shown that a fractal process can result in a semivariogram which fluctuates beyond the initial apparent range, and never actually reaches a sill, but continues to increase in semivariance with additional fluctuations. Examination of only the first of these cyclings does not provide sufficient detail to determine the process responsible (**Figure 43**).

Certain fractal measures, such as the Minkowski dimension and Korcak dimension, were appropriate since self-affinity existed for some scale range (Russ, pers. comm.). Hausdorff dimension estimates was made for comparison with previous studies, though with questionable accuracy since the surfaces were only affine (Russ, 1994). The Hausdorff, Minkowski, and Korcak dimensions all followed the same pattern over the study area (**Figure 33**). The different dimension measures were applied to discrete data, and would not be expected to agree exactly, however for relative depictions of roughness, any of the Minkowski, Hausdorff, or Korcak dimensions could be used to describe the study region. The Fourier fractal dimension exhibited a pattern distinct from the others, and if applied it should be qualified. It appears that seafloor roughness might be best defined at micro to macro scales as a periodic process superimposed by a fractal process. Minkowski and Hausdorff dimensions both depict the study area microtopography as generally relatively smooth, where the average Minkowski and Hausdorff dimension estimates were both approximately 1.2. Synthetic generation of combined periodic and fractal data is possible, however determination and measurement of those generated combined process attributes requires more than one quantitative procedure. Such processes are probably best defined using several parameters, requiring multiple analyses. Thus, defining a characteristic roughness height becomes complicated if it is to be considered integrative.

The mean of the power spectral slopes (-0.78) was close to the average value (-0.6) reported by Fox and Hayes (1985) for scales of 200 m to 3000 m and closer to the slightly more negative slope (approximately -0.65) obtained from millimeters-scale resolution stereogrammetric analysis of a small area of the Atlantic Ocean bottom (see Figure 45 in Fox and Hayes, 1985). The variation in the power spectra slopes and the different forms observed, and changes in slopes, indicate that the distribution of micro and macro-scale roughness features is quite heterogeneous over the study area, and that regional variabilities exist. The Fourier fractal dimension, calculated using the slope of a power spectrum which normally will agree with other fractal dimension estimates was distinct from the other fractal measures. The Fourier fractal dimension, D_{Fourier} , is less sensitive to noise (Russ, 1994), thus would appear more useful for analysis of *in situ* data. However, the agreement of D_{Fourier} with the others depends upon the behavior of the object analyzed. If the object is a true fractal, the phase values for the terms in the Fourier series will be random (Russ, 1994). If the phase values are not uniformly random, then the object cannot be considered fractal over all scales examined. Examination of the phase values distribution is another test of the suitability of fractal measures in addition to the semivariogram analysis or direct multi-scalar examination, and in this case attested to the limited scale-invariance of the seafloor. Non-random distributions of the phase values were evident in most of the Fourier power spectrum plots calculated (Appendix A). This may explain why D_{Fourier} behaves differently from the other fractal roughness measures and why the Fourier power spectral slope values follow a trend similar to standard deviation (**Figure 42**).

The FPS were calculated for entire profiles, as were the other measures, but the FPS appears to have been more sensitive to macro-scale variabilities and especially periodicities. Camera orientation may have affected this parameter most obviously. Where sand ripples were present (at the 28 m station), and where the interface possessed relatively high ripple-shaped structures which may have been sedimentary or biologically-induced (at the 60 m station), the FPS slopes were most negative, influenced more by low frequency variation. Although the Fourier

fractal dimension may seem the logical choice for describing fractals, which ideally possess information at all frequencies because of self-similarity (Russ, 1994) it may not be best in general. Using the FPS slopes to estimate the fractal dimension for only self-affine data, such as the sediment-water interface profile contours, should be limited to scale ranges for which self-affinity is observed in the data. However, it may be more effective for the initial FPS calculated for entire profiles to be used as a criterion for determining when measures of micro-scale roughness such as fractal dimensions should be emphasized, versus when macro-scale roughness measures are sufficient description.

Linear extrema measures such as the surface relief values over the maximum range of observation conveys only gross morphological character. Seafloor roughness is spatially variable, and therefore at most scales a single extrema measurement will convey very little about the local or regional roughness or spatial variabilities of the surface. The extrema measurement value might be considered as one of the many values expressed by semivariance, but a measurement able to convey only the maximum range of variation. Such measurements are still useful in some circumstances.

More informative single number parameters include the fractal dimension estimates and Fourier power spectrum slope. Both convey how measured variations change across spatial ranges. Power spectrum is especially useful in that a single power law relationship, expressed by the slope, has been shown to apply over a very broad range of scales, including those examined in this study. The difference between the mean FPS slope here and that reported for the broad range of scales by Fox and Hayes (1985) could not be explained as a result of their pre-whitening of spectra which tended to make slopes more negative. It does suggest that data from lower resolution sources may overestimate micro-scale seafloor roughness as Fox and Hayes (1985) suggest. The scopes of the several roughness measures applied are comparable to the distinctions between form drag and skin friction roughness, which may be defined separately, but bear close association.

Fractal measures are able to convey information which is pertinent to shear flow. A fractal dimension can be interpreted as expressing apparent length per length scale. An exact measurement may not be achieved for the length of a fractal line because it becomes longer as the measurement unit becomes smaller. However a measurement may be made of the line which expresses the scale of the measurement unit. The measurement unit may then be chosen according to the process of interest. For example, consider 1 cm diameter turbulent eddies. Their generation, persistence, and decay depends upon the interaction of the water motion with the bottom. How much bottom does the particle encounter? According to fractal theory, the length or area is technically undefined. An approximation may be made of the length of the pathline or area of the surface encountered by knowledge of one number, the fractal dimension, and choice of a measurement length. The dimension will allow conversion to length in terms of what the parcel actually "sees." For example, suppose the sediment-water interface observed by the 15 cm width SPI prism is the path over which a small turbulent eddy parcel crosses. Assume isotropy in the eddy dimensions, then it may be represented as a circle. The circle traces out a path as it crosses the line. The distance travelled can be estimated as the traced area divided by diameter. Doing the same below the SWI results in a traced area the same as one of those used to calculate the Minkowski dimension. The dimension represents the relationship between measure and scale, therefore may be used to recover a distance from any desired length scale. The previously discussed concepts concerning the strengths and weaknesses of the different measures are demonstrated in **Table 11**.

These concepts are analogous to the geometrical measures derived by dimensional analysis by Wooding et al. (1973), but require much less restrictive descriptions of the roughness elements. The fractal, geostatistical, and spectral depictions of the geometry all provide simple representations which may be used to produce statistical models of roughness elements. The applicability and validity of the models produced must be qualified by testable assumptions, however at least one of the three types of measure is likely to apply to most seafloor geometries

encountered. Similarly, the measures applied in this study allow extrapolation to many length scales, with or without adherence to assumptions, and therefore incorporate spatial notions similar to those expressed by Paola (1985). The efficacy of these measures, individually or combined, may then reside not in their discriminatory capabilities, but in their conveyence of cross-spatial-scale information. The application and interpretation of the spectral slopes must be qualified here. Since the camera prism window was limited to 15 cm, the image width was unable to accurately represent the larger roughness features. It is necessary to observe at least one full wavelength in order to produce a valid spectrum, therefore the slopes of the spectra from some SWI's may be misrepresentative of some of the roughness distributions.

ACKNOWLEDGEMENTS

The Virginia Institute of Marine Science, and Marine Geology and Geophysics at the Office of Naval Research provided support for this work. Many thanks to R. J. Diaz for all the opportunities and support. Thanks to the Captain and crew of the Research Vessel *Pacific Hunter* for the safe journey, and R. Gammisch for making deployments successful and recording positions. Thanks to J. C. Russ for many answers to obscure questions via e-mail. Thanks to Debbie Mondeel-Jarvis for the biological data from the area. Thanks to the members of V.I.M.S. Publications Center, library, ITNS, and most other departments for resources and support. Thanks to the faculty, staff, and students of V.I.M.S. for providing resources and thoughts.

REFERENCES

- Arakawa, K. and Krotkov, E., 1991. Estimating fractal dimension from range images of natural terrain. NASA report CMU-CS-91-156
- Austin, Jr., J. A., Fulthorpe, C. S., Mountain, G. S., Orange, D. L., Field, M. E., 1996. Continental-margin seismic stratigraphy: assessing the preservation potential of heterogeneous geologic processes operating on continental shelves and slopes. *Oceanography*, 9, 173-182.
- Barenblatt, G.I., Zhivago, A.V., Neprochnov, Yu.P., Ostrovskiy, A.A., 1984. The fractal dimension: a quantitative characteristic of ocean-bottom relief. *Marine Geology*, 24, #6, 695-697.
- Bokuniewicz, H. J., Gordon, R. B., Rhoads, D. C., 1975. Mechanical properties of the sediment-water interface. *Marine Geology*, 18, #4, 263-278.
- Bonsdorff, E., Diaz, R. J., Rosenberg, R., Norkko, A., Cutter Jr., G. R., 1996. Characterization of soft-bottom benthic habitats of the Aland Islands, northern Baltic Sea. *Mar. Ecol. Prog. Ser.*, 142, 235-245.
- Briggs, K. B., Stanic, S., 1988. Use of high-resolution roughness power spectra in predicting bottom backscattering. *J. Acoust. Soc. Am. (Suppl.)*, 84, no. suppl. 1, S122.
- Cressie, N. A. C., 1993. *Statistics for spatial data*. J. Wiley, New York.
- Cutler, C. D., Dawson, D. A., 1990. Nearest-neighbor analysis of a family of fractal distributions. *The Annals of Probability*, 18, #1, 256-271.
- Davis, J. C., 1986. *Statistics and data analysis in geology*. John Wiley and Sons, New York.
- Diaz, R. J., Cutter, G. R., Rhoads, D. C., 1994. The importance of bioturbation to continental slope sediment structure and benthic processes. *Deep-Sea Research II*, 41, 719-734.
- Diaz, R. J., Schaffner, L. C., 1988. Comparison of sediment landscapes in Chesapeake Bay as seen by surface and profile imaging; in: *Understanding the estuary: Advances in Chesapeake Bay research. Proceedings of a conference. 29-31 March 1988. Baltimore Maryland. Chesapeake Research Consortium Publication 129. CBP/TRS 24/88.*
- Folk, R. L., 1974. *Petrology of sedimentary rocks*. Hemphill Publ. Co., Austin, TX.
- Fox, C.G., Hayes, D.E., 1985. Quantitative methods for analyzing the roughness of the sea floor. *Reviews of Geophysics*, 23, 1-48.
- Frisch, A. A., Evans, D. A., Hudson, J. P., Boon III, J. D., 1987. Shape discrimination of sand samples using the fractal dimension. In: O. T. Magoon, et al., editors, *Coastal Zone '87*.
- Goff, J. A., Mayer, L. A., Hughes-Clarke, J., Pratson, L. F., 1996. Swath mapping on the continental shelf and slope: the Eel River Basin, northern California. *Oceanography*, 9, 178-182.

- Grant, W.D, Madsen, O.S., 1986. The continental-shelf bottom boundary layer. *Ann. Rev. Fluid Mech.*, 18, 265-305.
- Hastings, H. M., Sugihara, G., 1993. *Fractals: a user's guide to the natural sciences*. Oxford Univ. Press, New York.
- Herzfeld, U. C., 1989. Variography of submarine morphology: problems of deregularization, and cartographical implications. *Mathematical Geol.*, 21, 693-713.
- Herzfeld, U. C., Kim, I. I., Orcutt, J. A., and Fox, C. G., 1993. Fractal geometry and seafloor topography: theoretical concepts versus data analysis for the Juan de Fuca Ridge and the East Pacific Rise. *Ann. Geophysicae*, 11, 532-541.
- Journel, A. G., Huijbregts, C. J., 1978. *Mining geostatistics*. Academic Press, London.
- Lissner, A., Barnett, A., Johnson, T., Kanter, R., Smith, R., Diener, D., Ljubenkov, J., Watson, W., Phillips, C., Roberts, D., Benech, S., 1989. Benthic Reconnaissance of central and northern California OCS areas. OCS Study: MMS 89-0039, Final Report 1989, Volume 1.
- Loehle, C., Li, B., 1996. Statistical properties of ecological and geologic fractals. *Ecol. Modeling*, 85, 271-284.
- Malinverno, A., 1989. Segmentation of topographic profiles of the seafloor based on a self-affine model. *IEEE Jour. of Oceanic Engr.*, 14, 348-359.
- Mandelbrot, B. B., 1983. *The fractal geometry of nature*. Pergammon.
- Nittrouer, C. A., Kravitz, J. H., 1996. STRATAFORM: a program to study the creation and interpretation of sedimentary strata on continental margins. *Oceanography*, 9, 146-152.
- Paola, C., 1985. A method for spatially averaging small-scale bottom roughness. *Mar. Geol.*, 66, 291-301.
- Pearson, T. H., Rosenberg, R., 1978. Macrobenthic succession in relation to organic enrichment and pollution of the marine environment. *Oceanography and Marine Biology: an Annual Review*, 16, 229-311.
- Peitgen, H.-O., Jurgens, H., Saupe, D., 1992. *Chaos and fractals: new frontiers of science*. Springer-Verlag, New York. 984 pp.
- Pentland, A. P., 1984. Fractal-based description of natural scenes. *IEEE Trans. on Pattern Analy. and Machine Intelligence*, vol. PAMI-6, 661-674.
- Pequegnat, J. E., Mondeel-Jarvis, D., Borgeld, J. C., Bott, L., 1990. Sediment characteristics, benthic infauna, demersal fish and macroinvertebrates: analysis of communities found offshore in water between 18 and 73 meters deep west of Humbolt Bay, California, and at the nearshore disposal site (August 1989, November 1989, and March 1990). Ocean baseline survey report, Oct. 25 1990, to U.S. Army Corps of Engineers, San Francisco District.

- Pfeifer, P., 1984. Fractal dimension as a working tool for surface-roughness problems. *Applications of Surface Science*, 18, 146-164.
- Pratson, L. F., Lee, H. J., Parker, G., Garcia, M. H., Coakley, B. J., Mohrig, D., Locat, J., Mello, U., Parsons, J. D., Choi, S.-U., Isreal, K., 1996. Studies of mass-movement processes on submarine slopes. *Oceanography*, 9, 168-172.
- Ramsey, J. B., Yuan, H.-J., 1990. The statistical properties of dimension calculations using small data sets. *Nonlinearity*, 3, 155-176
- Rhoads, D.C., Cande, S., 1971. Sediment profile camera for in-situ study of organism-sediment relations. *Limnology and Oceanography*, 16, 110-114.
- Rhoads, D.C., Germano, J.D., 1982. Characterization of organism-sediment relations using sediment profile imaging: an efficient method of remote ecological monitoring of the seafloor (Remots(Trademark) system). *Mar. Ecol. Prog. Ser.*, 8, 115-128.
- Rhoads, D.C., Germano, J.D., 1986. Interpreting long-term changes in benthic community structure: A new protocol. *Hydrobiologia*, 142, 291-308.
- Robert, A, Richards, K. S., 1988. On the modeling of sand bedforms using the semivariogram. *Earth Surface Processes and Landforms*, 13, 459-473.
- Russ, J. C., Russ, J. C., 1989. Uses of Euclidean distance map for the measurement of features in images. *Jour. of Computer-Assisted Microscopy*, 1, 343-375.
- Russ, J. C., 1994. *Fractal surfaces*. Plenum Press, New York. 309 pp.
- Russ, J. C., 1995. *The image processing handbook*. CRC Press, Boca Raton, FL. 2nd ed.
- Steckler, M. S., Swift, D. J. P., Syvitski, J. P., Goff, J. A., Niedoroda, A. W., 1996. Modelling the sedimentology and stratigraphy of continental margins. *Oceanography*, 9, 183-188.
- Syvitski, J. P., Alexander, C. R., Field, M. E., Gardner, J. V., Orange, D. L., Yun, J. W., 1996. Continental-slope sedimentation: the view from northern California. *Oceanography*, 9, 163-167.
- Taylor, S. J., 1986. The measure theory of random fractals. *Mathematical Proceedings of the Cambridge Philosophical Society*, 100, 383-406.
- Theiler, J., 1990. Statistical precision of dimension estimators. *Physical Review A*, 41, 3038-3051.
- Vogel, S., 1994. *Life in moving fluids: the physical biology of flow*. Princeton Univ. Press, Princeton. NJ.
- Wheatcroft, R.A., 1994. Temporal variation in bed configuration and one-dimensional bottom roughness at the mid-shelf STRESS site. *Cont. Shelf Res.*, 14, 1167-1190.
- Wheatcroft, R.A., Borgeld, J.C., Born, R.S., Drake, D.E., Leithold, E.L., Nittrouer, C.A., Sommerfield, C.K., 1996. The anatomy of an oceanic flood deposit. *Oceanography*, 9, 158-162.

- Wiberg, P. L., Harris, C. K., 1994. Ripple geometry in wave-dominated environments. *J. of Geophys. Res.*, 99, 775-789.
- Wiberg, P. L., Cacchione, D. A., Sternberg, R. W., Wright, L. D., 1996. Linking sediment transport and stratigraphy on the continental shelf. *Oceanography*, 9, 153-157.
- Wooding, R. A., Bradley, E. F., and Marshall, J. K., 1973. Drag due to regular arrays of roughness elements of varying geometry. *Boundary-Layer Meteorol.*, 5, 285-308.
- Wright, L. D., Prior, D. B., Hobbs, C. H., Byrne, R. J., Boon, J. D., Schaffner, L. C., and Green, M. O., 1987. Spatial variability of bottom types in the lower Chesapeake Bay and adjoining estuaries and inner shelf. *Estuarine, Coastal and Shelf Science*, 24, 765-784.
- Wright, L. D., 1993. Micromorphodynamics of the inner continental shelf: a Middle Atlantic Bight case study. *Journal of Coastal Research*, Special Issue Number 15, 93-124.
- Wright, L. D., 1995. *Morphodynamics of inner continental shelves*. CRC Press, Boca Raton, FL.
- Wright, L. D., Friedrichs, C. T., Hepworth, D. A., in press. Effects of benthic biology on bottom boundary layer processes, Dry Tortugas Bank, Florida Keys. *Geo-Marine Letters*, 17.
- Wright, L. D., Schaffner, L. C., Maa, J. P.-Y., 1997. Biological mediation of bottom boundary layer processes and sediment suspension in the lower Chesapeake Bay. *Mar. Geol.* 141, 27-50.
- Yokoya, N., Yamamoto, K., Funakubo, N., 1989. Fractal-based analysis and interpolation of 3D natural surface shapes and their application to terrain modeling. *Computer Vision, Graphics, and Image Processing*, 46, 284-302.
- Ziebis, W., Huettel, M., Forster, S., 1996. Impact of biogenic sediment topography on oxygen fluxes in permeable seabeds. *Mar. Ecol. Prog. Ser.*, 140, 227-237.

Table 1. STRATAFORM (1995) sediment profile image station positions.

Station#	rep	#prof	#surf	Date	Time(GMT)	lat (deg min.min)	lon (deg min.min)
1	1	5	6	12/6/95	222443	40 57.801	124 16.927
1	2					40 57.781	124 16.897
1	3					40 57.799	124 16.872
1	4					40 57.797	124 16.87
1	5					40 57.783	124 16.877
1	6					40 57.78?	124 16.87?
2	1	5	5	12/6/95	231847	40 53.62	124 15.852
2	2					40 53.624	124 15.801
2	3					40 53.619	124 15.801
2	4					40 53.611	124 15.792
2	5					40 53.616	124 15.799
3	1	5	5	12/6/95	233122	40 53.427	124 15.418
3	2					40 53.365	124 15.408
3	3					40 53.364	124 15.395
3	4					40 53.353	124 15.381
3	5					40 53.339	124 15.366
10	1	5	5	12/7/95	221223	40 52.977	124 14.822
10	2					40 52.954	124 14.825
10	3					40 52.951	124 14.822
10	4					40 52.953	124 14.827
10	5					40 52.947	124 14.841
4	1	5	5	12/6/95	000026	40 52.96	124 14.501
4	2					40 52.968	124 14.483
4	3					40 52.975	124 14.485
4	4					40 52.98	124 14.482
4	5					40 52.974	124 14.476
5	1	5	5	12/7/95	191453	40 53.131	124 13.875
5	2					40 53.123	124 13.894
5	3					40 53.124	124 13.895
5	4					40 53.138	124 13.887
5	5					40 53.148	124 13.867
6	1	5	5	12/7/95	193535	40 52.962	124 13.805
6	2					40 52.968	124 13.785
6	3					40 52.969	124 13.78
6	4					40 52.969	124 13.747
6	5					40 52.967	124 13.746
7	1	5	5	12/7/95	205531	40 51.988	124 13.762
7	2					40 52.001	124 13.771
7	3					40 51.998	124 13.776
7	4					40 51.994	124 13.774
7	5					40 51.995	124 13.769
9	1	1	6	12/7/95	213858	40 52.194	124 12.867
9	2					40 52.188	124 12.851
9	3					40 52.193	124 12.855
9	4					40 52.191	124 12.861
9	5					40 52.179	124 12.864
9	6					40 52.17?	124 12.86?
8	1	5	5	12/7/95	211642	40 51.651	124 12.723
8	2			12/7/95	211730	40 51.65	124 12.736
8	3					40 51.663	124 12.744
8	4					40 51.663	124 12.746
8	5					40 51.668	124 12.727
TRIPODS							
VIMS(S-70)						40 53.648	124 16.993
VIMS(S-60)						40 53.434	124 15.158
UW(S-60)						40 53.395	124 15.333
USGS(S-50)						40 53.82	124 13.82

Table 2. Spatial domain image processing procedures. See internet homepage: <http://www.vims.edu/~cutter/im.html> for links to this routine and original color images.

The region of the image containing the entire sediment-water interface was selected from the digitized sediment profile image to reduce calculation time required for full image manipulation, and the cropped image was stored in RGB mode PICT files.

Filtering was applied to enhance the overall intensity level distribution based upon the intensity values in all of the color channels using the Image Processing Toolkit (IPTK) filter "Optimal Gray." The Look-Up Table Mode was then changed to Grayscale, since all image channels had been converted to an identical result.

The edge features were enhanced by applying a derivative-based convolution kernel matrix (an expanded version of the Grad N or Sobel kernel) to 7 X 7 pixel neighborhoods (See Russ, 1995 for a description of how kernels are applied):

The Grad N kernel (in canonical form):

$$\begin{matrix} -1 & -2 & -1 \\ 0 & 0 & 0 \\ 1 & 2 & 1 \end{matrix}$$

The image was thresholded, duplicated and image histogram inverted.

Images were combined using: Apply Filter \ Boolean operator \ Feature And.

The image histogram was inverted again.

Small, disjunct, noise-related features were removed by: Apply Filter \ Select (adjusting shape factor to <1) or Cutoff filter (features < approx. 100 pixels were deleted).

The remaining features were made 1 pixel-wide features by skeletonization (parameters: 4 coefficient = 3, depth = 2).

The intensity values were thresholded.

Visual inspection of the result compared to the original image was done by overlaying the thresholded image on the original "surfsect" image, and using Image \ Apply Image \ Multiply (100% opacity).

If the extracted contour was not continuous, it was made so by overlapping features by blurring using Gaussian blurring or a Euclidean distance map, thresholding, then contracting to single-pixel features by skeletonization.

Visual inspection of the overlain result upon the original sediment-water interface section image was done again to verify improvement.

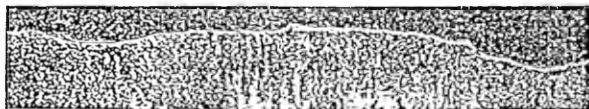
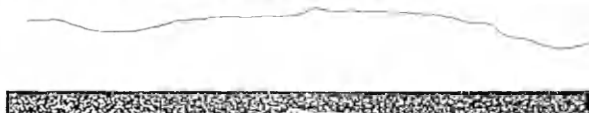
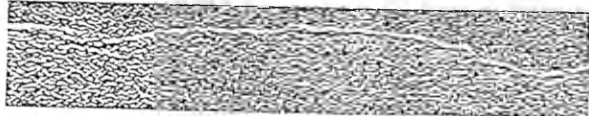
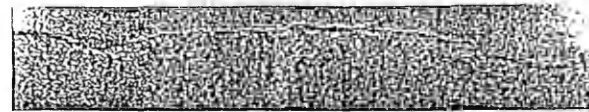
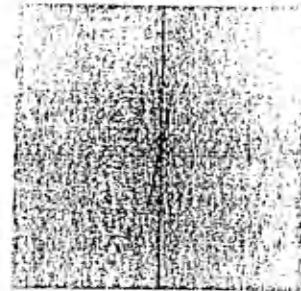


Table 3. Frequency domain image processing procedures. See internet homepage: <http://www.vims.edu/~cutter/im.html> for links to this routine and original color images.

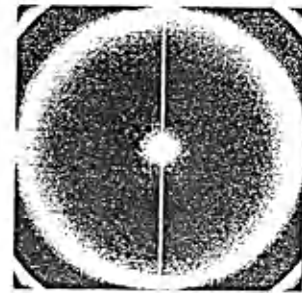
- The region of the image containing just the sediment-water interface and nearby area was selected from the digitized sediment profile image and then converted by expansion of background to a square image with pixel width and height equal to a power of 2.



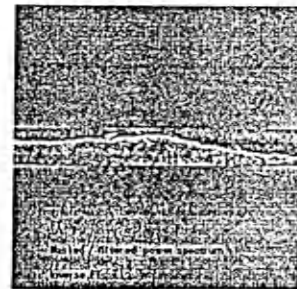
- Frequency transformation was done using Fast Fourier Transform techniques via the Image Processing Toolkit (IPTK) Filter: Forward FT



- The power spectrum image was filtered using a combination of a Hamming filter and an annulus approximately with inner and outer radii of about 90 and 110 % of half the image width.



- An inverse Fourier Transform was applied to convert the image to the spatial domain.



- The result was thresholded to extract the enhanced sediment-water interface profile contour.



- Small noise-related features were removed using the Cutoff filter of the IPTK. Then continuity was achieved via slight blurring using Gaussian blur or EDM filtering, thresholding, and skeletonizing to produce the resultant SWI profile contour.



Sediment (cm) (1.4)

Table 4. Theoretical and calculated fractal dimensions for generated fractal lines.

Method	α	Theoretical	Hausdorff	Minkowski	Kolmogorov	Korcak
midpoint displacement	0.9	1.1	1.0639	1.092	1.1101	1.0
midpoint displacement	0.8	1.2	1.1712	1.19	1.2073	1.0573
midpoint displacement	0.7	1.3	1.2332	1.245	1.2823	1.3825
midpoint displacement	0.6	1.4	1.4074	1.341	1.3928	1.4172
midpoint displacement	0.5	1.5	1.4781	1.383	1.4539	1.4735

Table 5. Assumptions concerning scaling behavior required for dimension estimators.

Dimension	Implementation	Scaling behavior required
Hausdorff	Richardson plot	Self-similar data or zerosets
Minkowski	Successive coverings to produce Minkowski comfoter	Self-similar or self-affine
Kolmogorov	Box counting	Self-similar only
Korcak	Relationship between spacing of zero crossings for line profiles	Self-affine
Fourier	Power spectral slope relationship	Self-similar or self affine

Table 6. Minkowski Dimension estimation data for selected coverages.

Image	Pixel Intensity Level	Distance by Level (cm)	Number of Pixels	Area (cm ²)
a	10	0.07	269	1.8
b	27	0.18	771	5.1
c	72	0.48	2091	13.9
d	170	1.13	5177	34.5

Dimension estimate using slope of log transformed data: 1.04

DEPTH	STA	REP	RPD	PEN	SURE	BIOTURB	MIXDEP	LAYERS	BEDFORMS	TYPE	WAVEL	HI	SEDTYPE	SEDTYPE2	PHIMED	PHIRNG	WORMS	VOIDS	BURR	TUBES	EPIFAUNA
			(cm)	(cm)	(cm)	(cm)	(cm)	(#)	(#)		(cm)	(cm)					(#)	(#)	(#)	(#)	(#)
28	8	1	1.4	1.4	1.6	NONE	0	1	Y	IND	NA	IND	SAND	VFS	1.75	1-4	0	0	0	0	0
28	8	2	2.0	2.2	2.2	NONE	0	1	Y	SYM	12.4	2.5	SAND	FS	1.75	1-4	0	0	0	0	1
28	8	3	1.7	1.7	3.5	NONE	0	1	Y	SYM	15.0	2.5	SAND	FS	1.75	1-4	0	0	0	0	0
28	8	4	1.6	1.6	2.8	NONE	0	1	Y	IND	NA	2.5	SAND	FS	1.75	1-4	0	0	0	0	0
28	8	5	2.2	2.2	2.1	NONE	0	1	Y	SYM	NA	2.5	SAND	FS	1.75	1-4	0	0	0	0	3
36	9	1	1.4	1.4	1.0	NONE	0	1	Y	IND	>>157	IND	SAND	FS	2	1-4	0	0	0	0	0
43	7	1	2.0	2.0	0.4	TRACE	IND	1	Y	IND	NA	IND	SAND	VFS	2.5	1-9	0	0	0	0	4
43	7	2	1.1	1.1	0.5	IND	IND	1	Y	IND	NA	IND	SAND	VFS	2.5	1-9	0	0	0	0	0
43	7	3	1.6	1.6	0.8	IND	IND	1	Y	IND	NA	1.0	SAND	VFS	2.5	1-9	0	0	0	0	2
43	7	4	0.3	0.3	0.9	IND	IND	1	Y	SYM	10.0	1.5	SAND	VFS	2.5	1-9	0	0	0	0	0
43	7	5	IND	2.5	1.7	IND	IND	1	Y	IND	NA	1.5	SAND	VFS	2.5	1-9	0	0	0	0	3
48	6	1	0.1	3.2	1.6	TRACE	IND	1	Y	ASYM	>15	1.5	SAND	VFS	3	2-8	0	0	0	0	2
48	6	2	0.2	5.9	1.6	TRACE	IND	1	IND	NA	NA	NA	SAND	VFS	3	2-8	1	0	0	0	0
48	6	3	IND	5.9	0.7	TRACE	IND	1	IND	NA	NA	NA	SAND	VFS	3	2-8	2	0	0	1	1
48	6	4	IND	5.2	1.4	IND	IND	1	IND	NA	NA	NA	SAND	VFS	3	2-8	1	0	0	0	1
48	6	5	IND	4.1	2.2	TRACE	IND	1	Y	ASYM	10.5	2.5	SAND	VFS	3	2-8	0	0	0	0	0
50	5	1	0.3	8.1	1.1	LOW	IND	3	Y	ASYM	>15	1.0	MUDDY-SAND	SASI	3.5	2-9	0	1	0	0	0
50	5	2	0.1	8.4	1.5	MED	8	3	Y	ASYM	IND	1.5	MUDDY-SAND	SASI	3.5	2-9	8	1	1	0	0
50	5	3	0.1	8.5	1.2	LOW	IND	4	Y	ASYM	IND	1.5	MUDDY-SAND	SASI	3.5	2-9	1	0	0	0	1
50	5	4	0.0	5.6	1.0	NONE	0	2	Y	ASYM	IND	IND	MUDDY-SAND	SISA	3.5	2-9	0	0	0	0	0
50	5	5	0.0	5.2	1.2	LOW	5	2	Y	ASYM	NA (>15)	1.5	MUDDY-SAND	SISA	3.5	2-9	0	0	0	0	1
52	4	1	0.2	7.8	1.4	LOW	5	3	N				MUD	CLSI	4.5	3-9	0	0	1	0	0
52	4	2	0.1	5.7	1.3	LOW	4	3	N				MUD	CLSI	4.5	3-9	2	0	0	0	0
52	4	3	0.3	10.0	1.1	LOW	5	3	N				MUD	CLSI	4.5	3-9	1	1	1	0	0
52	4	4	0.2	8.8	1.6	HIGH	8	3	N				MUD	CLSI	4.5	3-9	3	2	2	0	0
52	4	5	0.4	8.7	1.8	HIGH	8	4	IND	IND	157	IND	MUD	CLSI	4.5	3-9	1	2	4	0	0
55	10	1	0.6	14.4	2.0	HIGH	14	6	N				MUD	SASICL	5	3-10	2	2	1	0	0
55	10	2	0.2	11.6	2.1	HIGH	11	5	N				MUD	SASICL	5	3-10	2	1	0	0	0
55	10	3	0.2	11.6	1.6	LOW	5	5	Y	ASYM	IND	2.0	MUD	SASICL	5	3-10	1	1	0	0	0
55	10	4	0.3	10.7	2.0	MED	5	4	N				MUD	SASICL	5	3-10	0	3	0	0	0
55	10	5	0.4	9.6	1.1	LOW	5	3	N				MUD	SASICL	5	3-10	3	3	1	3	0
60	3	1	0.3	15.3	1.5	HIGH	10	7	N	IND	11.4	IND	MUD	SICL	7	6-10	3	2	3	1	2
60	3	2	0.4	16.1	1.5	LOW	5	7	N		13.0		MUD	SICL	7	6-10	0	4	3	0	0
60	3	3	0.3	15.5	1.1	MED	10	6	N				MUD	SICL	7	6-10	0	4	1	0	0
60	3	4	0.2	15.9	1.2	MED	8	7	N	IND	11.0	IND	MUD	SICL	7	6-10	0	5	0	0	0
60	3	5	0.2	16.3	1.5	HIGH	15	8	N				MUD	SICL	7	6-10	2	3	3	0	0
64	2	1	0.3	13.0	0.8	HIGH	12	5	N				MUD	SASICL	7	5-9	1	7	2	0	0
64	2	2	0.3	12.1	0.9	MED	10	4	N				MUD	SASICL	7	5-9	2	2	3	1	0
64	2	3	0.0	13.6	2.5	HIGH	10	4	N				MUD	SASICL	7	5-9	2	2	1	0	0
64	2	4	0.5	11.4	1.2	HIGH	10	4	N				MUD	SASICL	7	5-9	1	2	4	0	0
64	2	5	0.7	12.8	0.8	HIGH	10	4	N				MUD	SASICL	7	5-9	1	3	2	1	0
83	1	1	0.8	20.0	1.2	HIGH	15	5	N				MUD	SICL	7	5-9	0	4	1	0	0
83	1	2	0.9	15.9	2.0	HIGH	15	5	N				MUD	SICL	7	5-9	2	2	1	0	0
83	1	3	IND	13.2	2.2	HIGH	10	4	N				MUD	SICL	7	5-9	1	6	0	0	0
83	1	4	0.5	17.7	1.1	MED	10	5	N				MUD	SICL	7	5-9	12	2	1	0	0
83	1	6	0.5	13.1	1.1	MED	10	4	N				MUD	SICL	7	5-9	0	4	1	1	0

Table 8. Summary sediment profile image (SPI) feature measurements from computerized and visual analyses.

DEPTH (m)	STATION	N	STAT	RPD (cm)	PEN (cm)	SURF (cm)	SD (cm)	PHIMED (approx.)	GRSIZE (mm)	LAYERS (#)	MIXDEPTH (cm)	WORMS (#)	VOIDS (#)	BURR (#)	TUBES (#)	EPIFAUNA (#)	Deposit (cm)	SPI Layer 1 (cm)
28	8	5	mean	1.8	1.8	2.4	0.77	1.8	0.3	1.0	0.0	0	0	0	0	1	0.0	0.0
28	8	5	SD	0.3	0.3	0.8	0.21	0.0	0.0	0.0	0.0	0	0	0	0	2	0.0	0.0
28	8	5	min	1.4	1.4	1.6	0.62	1.8	0.3	1.0	0.0	0	0	0	0	0	0.0	0.0
28	8	5	max	2.2	2.2	3.5	1.01	1.8	0.3	1.0	0.0	0	0	0	0	4	0.0	0.0
36	9	1	mean	1.4	1.4	1.0	0.34	2.0	0.3	1.0	0.0	0	0	0	0	0	0.0	0.0
36	9	1	SD	•	•	•	•	•	•	•	•	•	•	•	•	•	•	•
36	9	1	min	1.4	1.4	1.0	0.34	2.0	0.3	1.0	0.0	0	0	0	0	0	0.0	0.0
36	9	1	max	1.4	1.4	1.0	0.34	2.0	0.3	1.0	0.0	0	0	0	0	0	0.0	0.0
43	7	5	mean	1.3	1.5	0.9	0.13	2.5	0.2	1.0	•	0	0	0	0	2	0.0	0.0
43	7	5	SD	0.7	0.9	0.5	0.07	0.0	0.0	0.0	•	0	0	0	0	2	0.0	0.0
43	7	5	min	0.3	0.3	0.4	0.06	2.5	0.2	1.0	•	0	0	0	0	0	0.0	0.0
43	7	5	max	2.0	2.5	1.7	0.17	2.5	0.2	1.0	•	0	0	0	4	0.0	0.0	
48	6	5	mean	0.1	4.9	1.5	0.41	3.0	0.1	2.0	•	1	0	0	0	1	0.5	0.9
48	6	5	SD	0.1	1.2	0.5	0.19	0.0	0.0	0.0	•	1	0	0	0	1	0.0	1.3
48	6	5	min	0.1	3.2	0.7	0.21	3.0	0.1	2.0	•	0	0	0	0	0	0.5	0.0
48	6	5	max	0.2	5.9	2.2	0.73	3.0	0.1	2.0	•	2	0	0	1	2	0.5	2.9
50	5	5	mean	0.1	7.2	1.2	0.37	3.5	0.1	2.8	4.3	2	0	0	0	0	0.5	2.6
50	5	5	SD	0.1	1.6	0.2	0.06	0.0	0.0	0.8	4.0	3	1	0	0	1	0.0	0.4
50	5	5	min	0.0	5.2	1.0	0.27	3.5	0.1	2.0	0.0	0	0	0	0	0	0.5	2.0
50	5	5	max	0.3	8.5	1.5	0.44	3.5	0.1	4.0	8.0	8	1	1	0	1	0.5	3.0
52	4	5	mean	0.2	8.2	1.4	0.37	4.5	0.0	3.2	6.0	1	1	2	0	0	2.0	2.4
52	4	5	SD	0.1	1.6	0.3	0.13	0.0	0.0	0.4	1.9	1	1	2	0	0	0.0	0.5
52	4	5	min	0.1	5.7	1.1	0.23	4.5	0.0	3.0	4.0	0	0	0	0	0	2.0	1.7
52	4	5	max	0.4	10.0	1.8	0.55	4.5	0.0	4.0	8.0	3	2	4	0	0	2.0	2.9
55	10	5	mean	0.3	11.6	1.8	0.54	5.0	0.0	4.6	8.0	2	2	1	1	0	2.0	2.3
55	10	5	SD	0.2	1.8	0.4	0.22	0.0	0.0	1.1	4.2	1	1	1	1	0	0.0	0.3
55	10	5	min	0.2	9.6	1.1	0.20	5.0	0.0	3.0	5.0	0	1	0	0	0	2.0	2.1
55	10	5	max	0.6	14.4	2.1	0.78	5.0	0.0	6.0	14.0	3	3	1	3	1	2.0	2.8
60	3	5	mean	0.3	15.8	1.3	0.37	7.0	0.0	7.0	9.6	1	4	2	0	1	4.0	2.1
60	3	5	SD	0.1	0.4	0.2	0.10	0.0	0.0	0.7	3.6	1	1	1	0	1	0.0	0.2
60	3	5	min	0.2	15.3	1.1	0.22	7.0	0.0	6.0	5.0	0	2	0	0	0	4.0	1.8
60	3	5	max	0.4	16.3	1.5	0.48	7.0	0.0	8.0	15.0	3	5	3	0	3	4.0	2.4
64	2	4	mean	0.4	12.3	0.9	0.21	7.0	0.0	4.3	10.5	1	4	3	1	0	4.0	2.8
64	2	4	SD	0.2	0.7	0.2	0.12	0.0	0.0	0.6	1.0	1	3	1	1	0	0.0	0.3
64	2	4	min	0.3	11.4	0.8	0.02	7.0	0.0	4.0	10.0	1	2	2	0	0	4.0	2.5
64	2	4	max	0.7	13.0	1.2	0.30	7.0	0.0	5.0	12.0	2	7	4	1	0	4.0	3.1
83	1	4	mean	0.7	16.7	1.4	0.33	7.0	0.0	4.8	12.5	4	3	1	0	0	1.0	2.9
83	1	4	SD	0.2	2.9	0.4	0.04	0.0	0.0	0.5	2.9	6	1	0	1	0	0.0	0.5
83	1	4	min	0.5	13.1	1.1	0.28	7.0	0.0	4.0	10.0	0	2	1	0	0	1.0	2.4
83	1	4	max	0.9	20.0	2.0	0.36	7.0	0.0	5.0	15.0	12	4	1	1	0	1.0	3.5

Legend of terms for Tables 7 and 8.

<u>Term</u>	<u>Meaning and (units)</u>
DEPTH	Water depth in meters (m)
STA or STATION	Station number
REP	“Replicate” deployment number
N	Number of cases
STAT	Summary statistic (mean = arithmetic mean, SD = standard deviation, min = minimum value, max = maximum value)
RPD	Average depth of the apparent color redox potential discontinuity layer (cm), IND = indeterminate (generally because of surface layer disturbance or shallow penetration)
PEN	Sediment profile camera prism penetration depth (cm)
SURF	Sediment surface relief as elevational extrema (cm)
SD	Standard deviation of the sediment water interface elevations (cm)
BIOTURB	Apparent degree of bioturbation (category level: NONE = no visible signs, TRACE = very small amount of signs of bioturbation, LOW = relatively small amount of signs of bioturbation, MED = moderate amount of bioturbational signs, HIGH = predominance of bioturbational signs)
MIXDEPTH	Apparent biological mixing depth (cm), • = missing
LAYERS	Number of depositional layers apparent (#)
BEDFORMS	Presence (Y) or absence (N) of sediment bedforms, IND = indeterminate
TYPE	Type of bedforms, if present: SYM = symmetric, ASYM = asymmetric, IND = indeterminate
WAVEL	Wavelength of bedforms (cm), if present: NA = not available from image due to wavelength magnitude or image orientation, IND = indeterminate
HT	Height of bedforms, if present
SEDTYPE	Gross sediment type, mud or sand
SEDTYPE2	Apparent sediment type, VFS = very fine sand, FS = fine sand, SASI = sandy silt, SISA = silty sand, CLSI = clayey silt, SASICL = sandy silty clay, SICL = silty clay
PHIMED	Apparent median sediment phi (see Folk, 1974)
PHIRNG	Apparent phi range
GRSIZE	Apparent mean sediment grain size (mm)
VOIDS	Number of water-filled biogenic voids (#)
WORMS	Number of infaunal worms: annelids or nemerteans (#)
BURR	Number of infaunal burrow structures (#)
TUBES	Number of surficial biogenic tubes (#)
EPIFAUNA	Number of epifaunal organisms (#)
Deposit	Eel River 1995 flood deposit thickness (cm) estimated from Wheatcroft, et al. (1996)
SPILayer1	Mean thickness (cm) of the uppermost layer in sediment profile images

Table 9. Comparison of fractal measures for sediment water interface profile contours obtained by manual tracing (TRACE) and spatial (SPAT) and frequency (FREQ) domain image processing routines. Rich = Hausdorff dimension estimate from Richardson plot method, Mink = Minkowski dimension estimate, Kolm = Kolmogorov dimension estimate, FPS slope = slope of the Fourier power spectrum, Four = Fourier fractal dimension estimate, SD = standard deviation.

Image	Method	Rich	(SD)	Mink	(SD)	Kolm	(SD)	Korc	(SD)	FPS slope	(SD)	Four
1-4	TRACE	1.3318	0.0089	1.327	0.0019	1.3145	0.0103	1.5138	0.0306	-0.9088	0.0155	1.5456
	SPAT	1.1491	0.0076	1.106	0.0084	1.1367	0.0153	1.0560	0.0140	-0.7230	0.0137	1.6385
	FREQ	1.1392	0.0083	1.096	0.0070	1.1355	0.0168	NA	NA	-0.6488	0.0152	1.6756
10-1	TRACE	1.0877	0.0024	1.150	0.0014	1.1399	0.0224	1.0674	0.0237	-0.9332	0.0073	1.5334
	SPAT	1.0410	0.0013	1.082	0.0043	1.0814	0.0234	1.0339	0.0087	-0.8700	0.0086	1.5650
	FREQ	1.0337	0.0020	1.096	0.0077	1.0647	0.0163	NA	NA	-0.7082	0.0115	1.6459
4-1	TRACE	1.1770	0.0056	1.177	0.0036	1.2226	0.0188	1.2450	0.0318	-0.7335	0.0133	1.6333
	SPAT	1.0657	0.0031	1.078	0.0037	1.1044	0.0139	NA	NA	-0.6448	0.0121	1.6776
	FREQ	1.0843	0.0027	1.082	0.0015	1.1029	0.0197	1.0884	0.0226	-0.5820	0.0134	1.7090

Table 10. Comparison of relief and roughness measurements from image 8-5, including and excluding epifaunal seapens. SD = standard deviation, D = dimension, mv = multivalued function form, and pc = piecewise continuous form of the sediment-water interface profile contour line.

Epifaunal Sea Pens	Surface Relief (cm)	SD (cm)	Power Spectral Slope	Hausdorff D	Minkowski D (mv)	Minkowski D (pc)	Fourier D
Included	10.1	1.6	-0.98	1.52	1.56	1.17	1.51
Excluded	2.1	0.7	-0.94	1.11	1.16	1.15	1.53

Table 11. Strengths and weaknesses of measures applied.

Measure	Strength	Weakness
Relief	Ease of calculation	May be completely determined by two extreme values in an otherwise uniform series
Standard Deviation (or RMS)	Relative ease of calculation, and generality of application	Unable to express wavelength(-like) information or discern scale of dominant features
Fractal Dimension	Able to express roughness information for series resembling multivalued or non-differentiable functions, and able to convey roughness independent of scale	Must have or assume self-similar or self-affine data
Spectral Slope	Able to discern and convey information about roughness element wavelengths and the relative contribution of different scale roughness elements	Must have piecewise continuous data series, and linear slope only conveys a single fit to data from a spectrum which may be even more useful in other terms

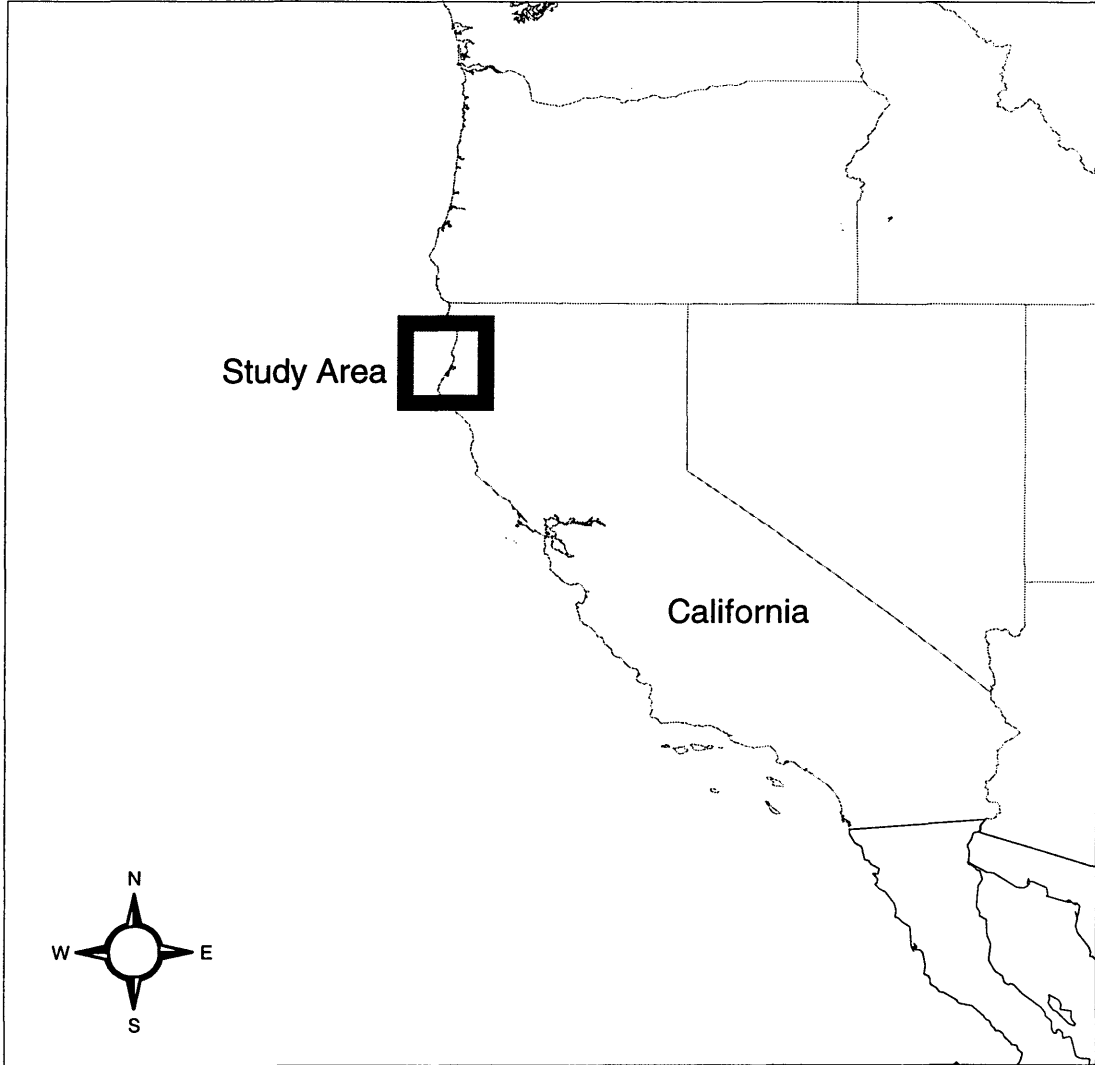


Figure 1. STRATAFORM study area off northern California.

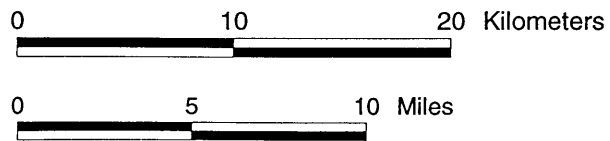
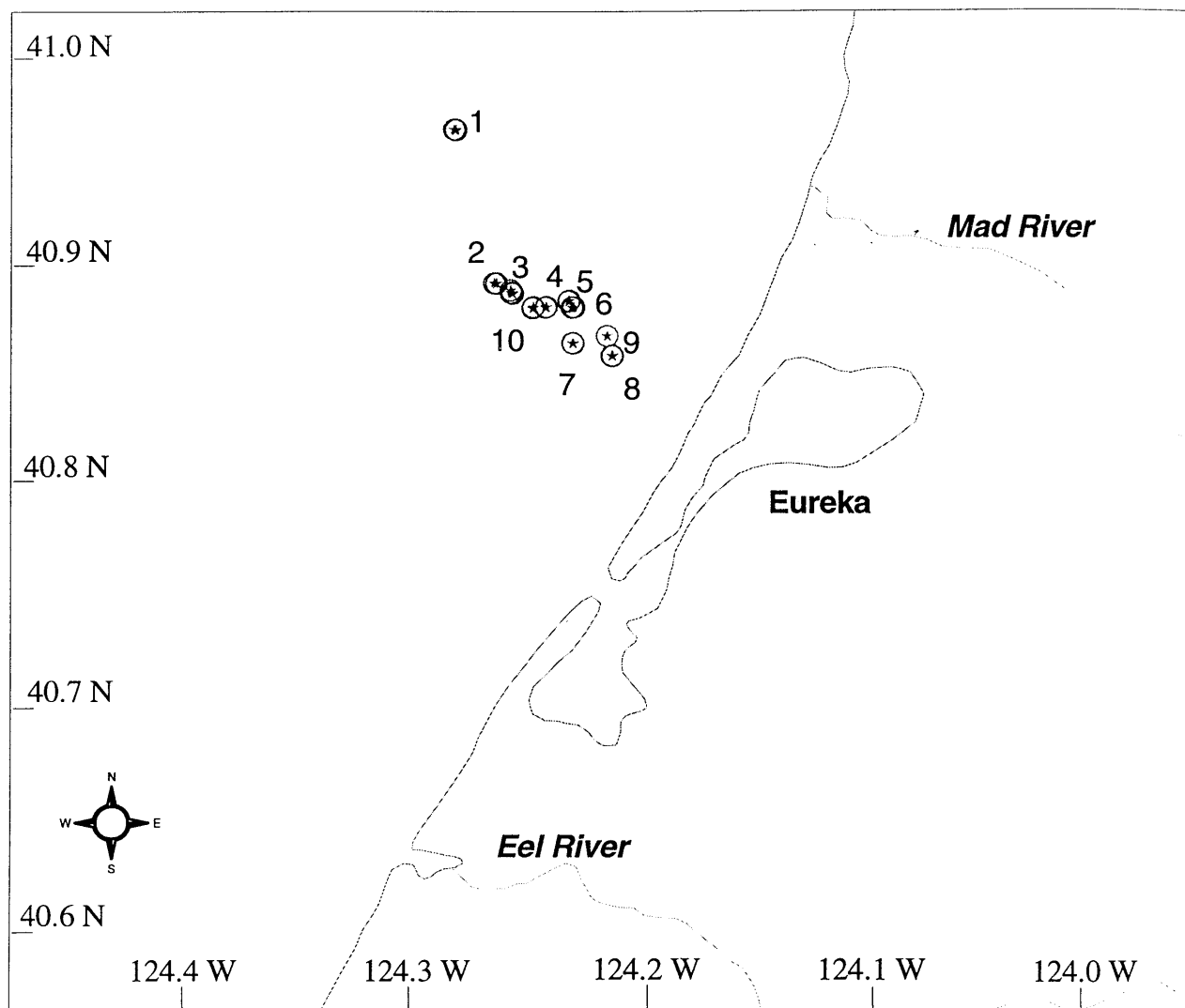


Figure 2. SPI study transect on the Eel margin, off Eureka, California. Station markers are labelled with station numbers.

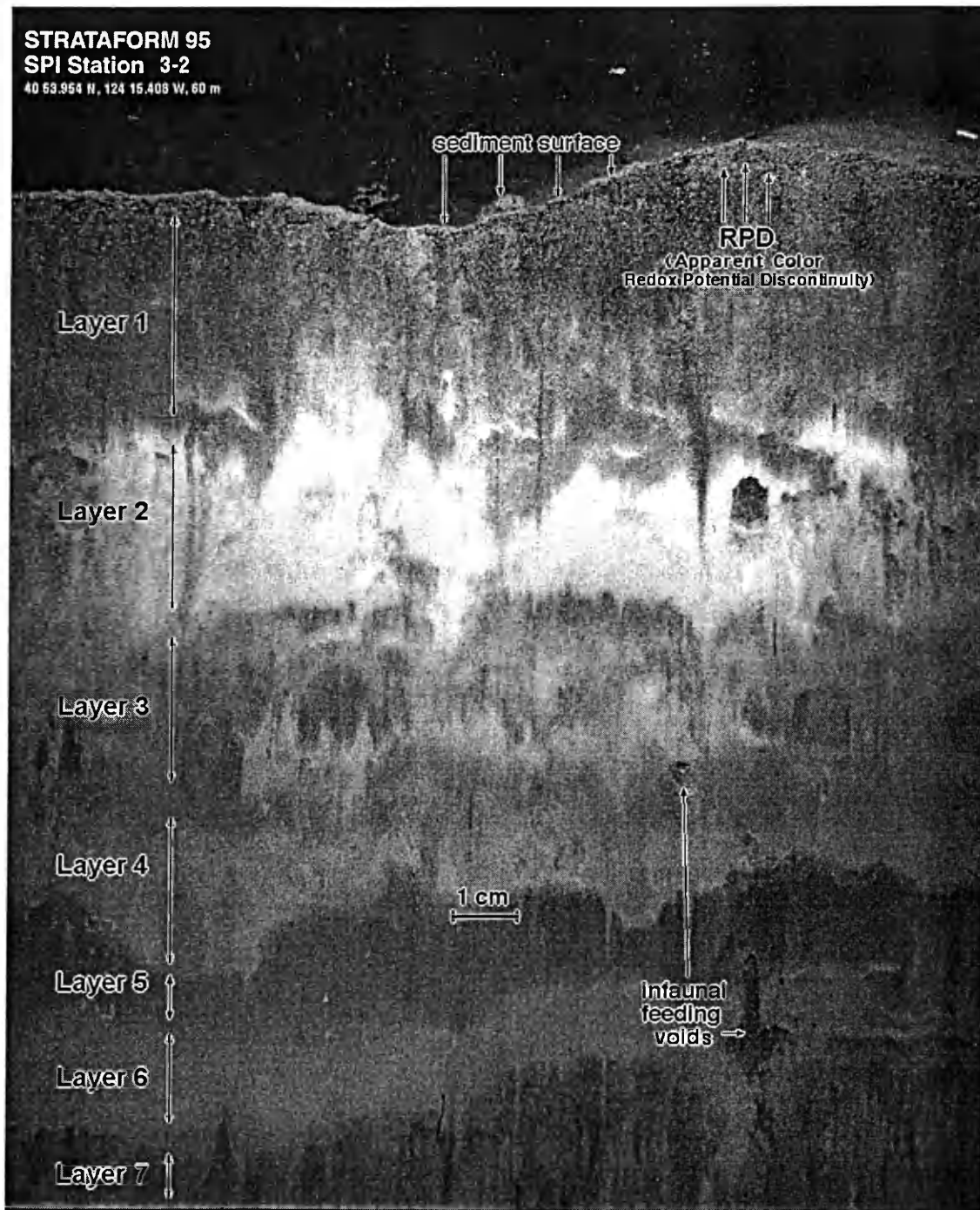


Figure 3. Sediment profile image from 60 m water depth (Station 3) revealing several sedimentary and biological features. The depositional layering is clearly evident as distinct color laminations. This station was closest to the VIMS physical data pod deployed Jan. 1996.

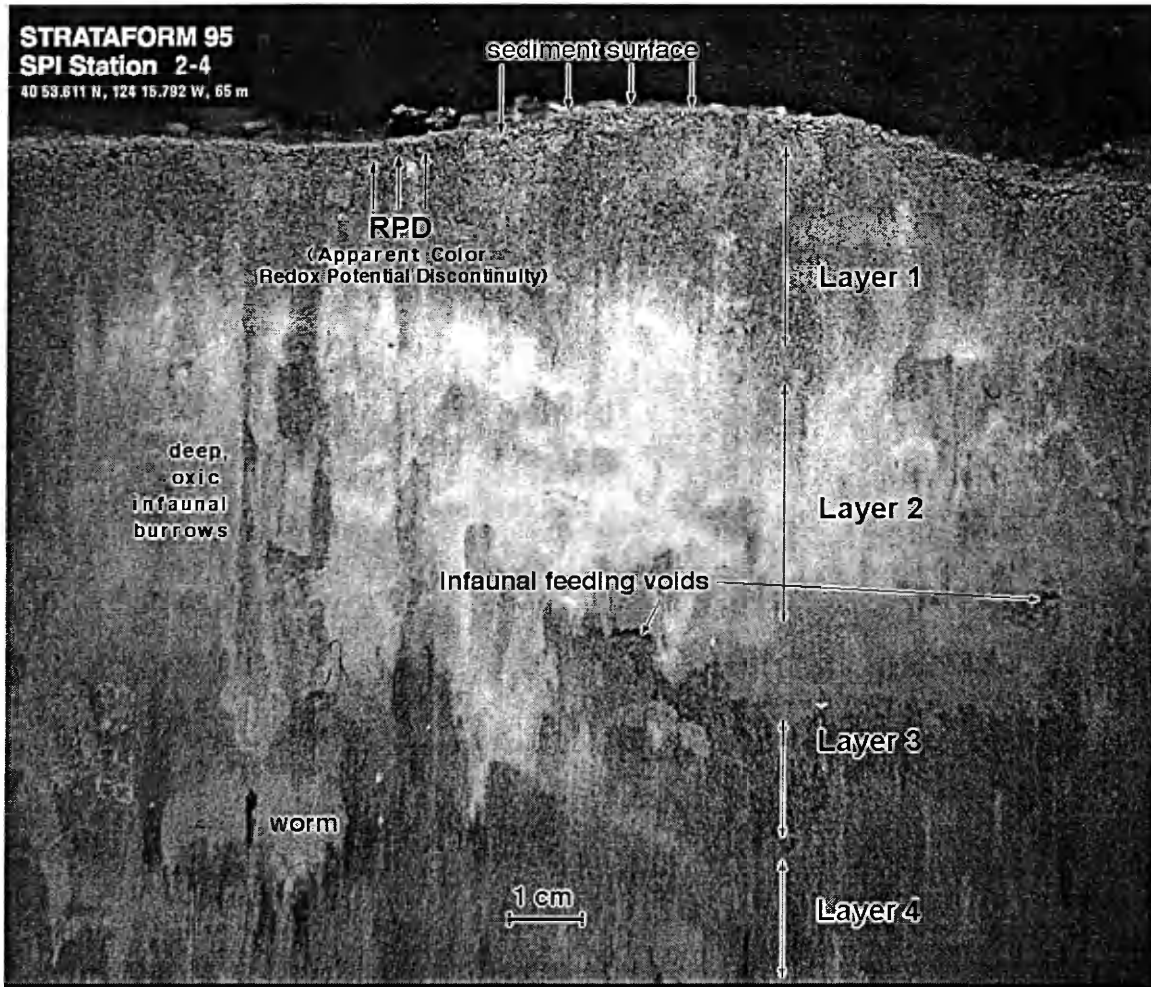


Figure 4. Sediment profile image from 65 m water depth (Station 2) revealing several sedimentary and biological features.

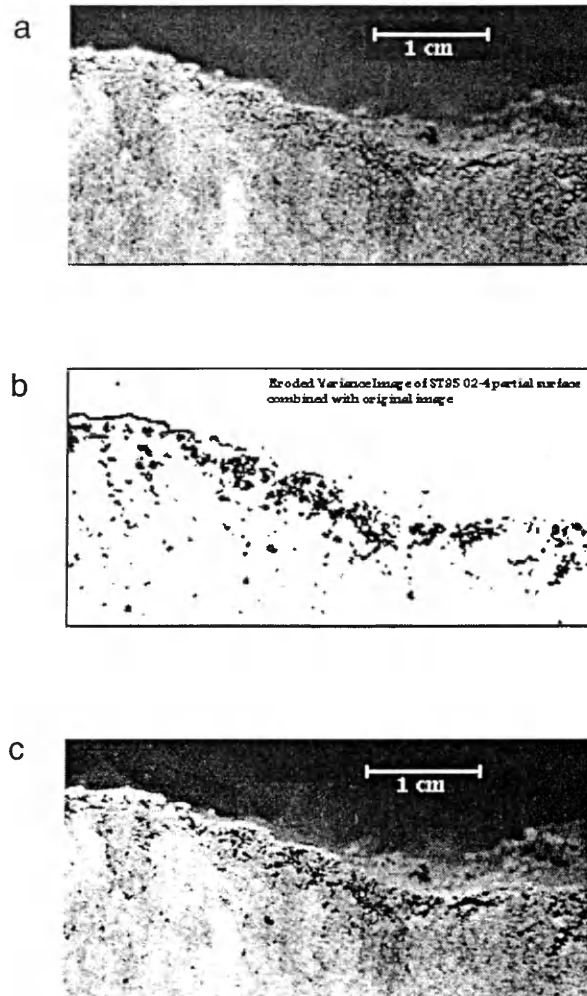
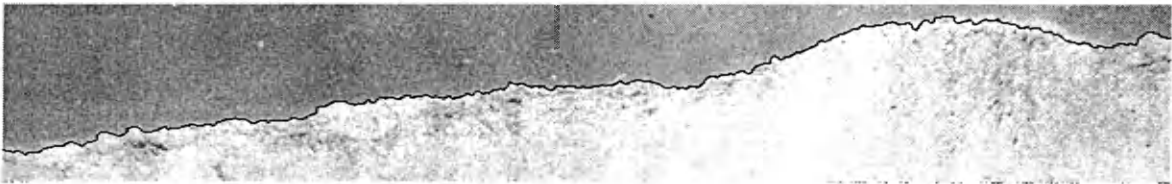


Figure 5. Close-up view of a section of the sediment-water interface from a profile image from 65 m water depth (Station 2). The unconsolidated surface layer results from bioturbational activities of benthic infauna which are abundant in the sediments of the Eel River deposits. The magnified section of the original image (a), was processed digitally using spatial filters to exploit the regions of high variance in the image (b) which represented the large sediment pore spaces. The variance image was combined with a grayscale version of the original (c) to allow comparison.

a



b



c



Figure 6. (a) Sediment-water interface section from image 3-5 (60 m water depth), (b) traced SWI contour overlaid, and (c) just the SWI contour used for roughness measures.

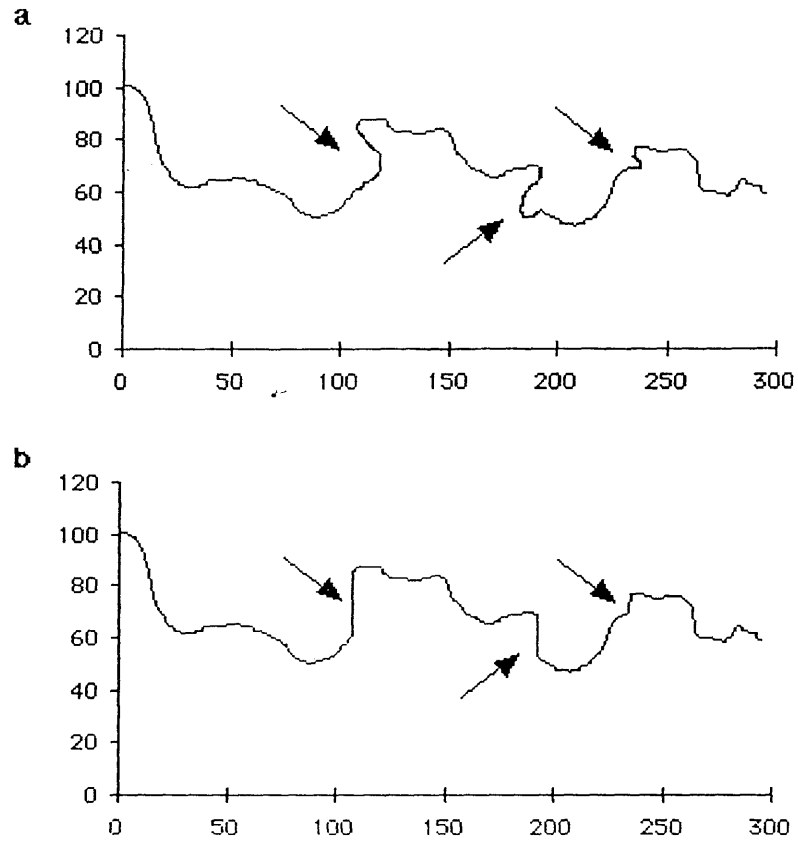


Figure 7. Examples of multivalued (a) and piecewise continuous (b) series. Arrows indicate portions of series a which must be modified in order to achieve continuous data which does not have more than one vertical coordinate for any point along the horizontal axes in order to use certain roughness measures.

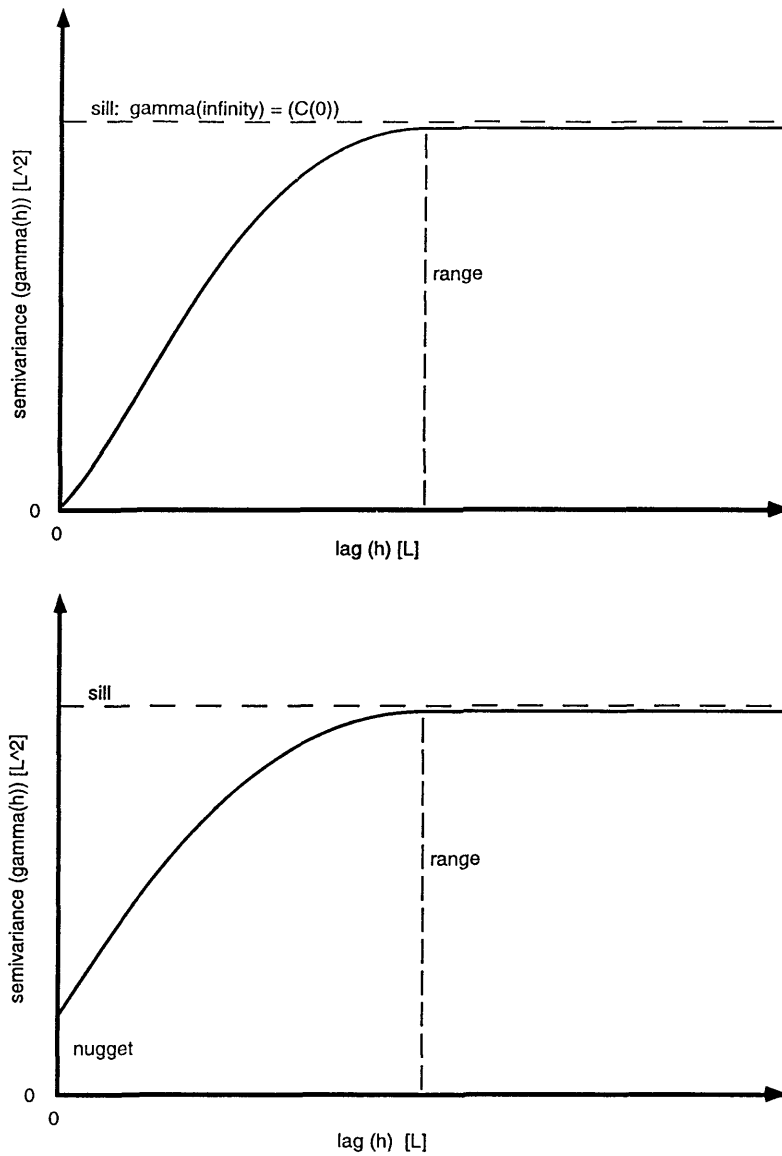


Figure 8. Features of semivariograms. The semivariance ($\gamma(h)$) of a variable with some spatial continuity will increase with increasing lag. The lag (h) is the interval between samples of the variable. Semivariance for a particular h is half the sum of all variances of the data separated by that distance or time h . The nugget effect indicates non-zero semivariance at the smallest lag, and suggests that the data resolution was insufficient to detect the smallest variability of the series. The range is the distance lag over which the semivariance reaches the sill, the overall variance of the series. Beyond the sill, the variable is no longer considered correlated if the semivariogram behaves asymptotically. Redrawn from Davis (1986).

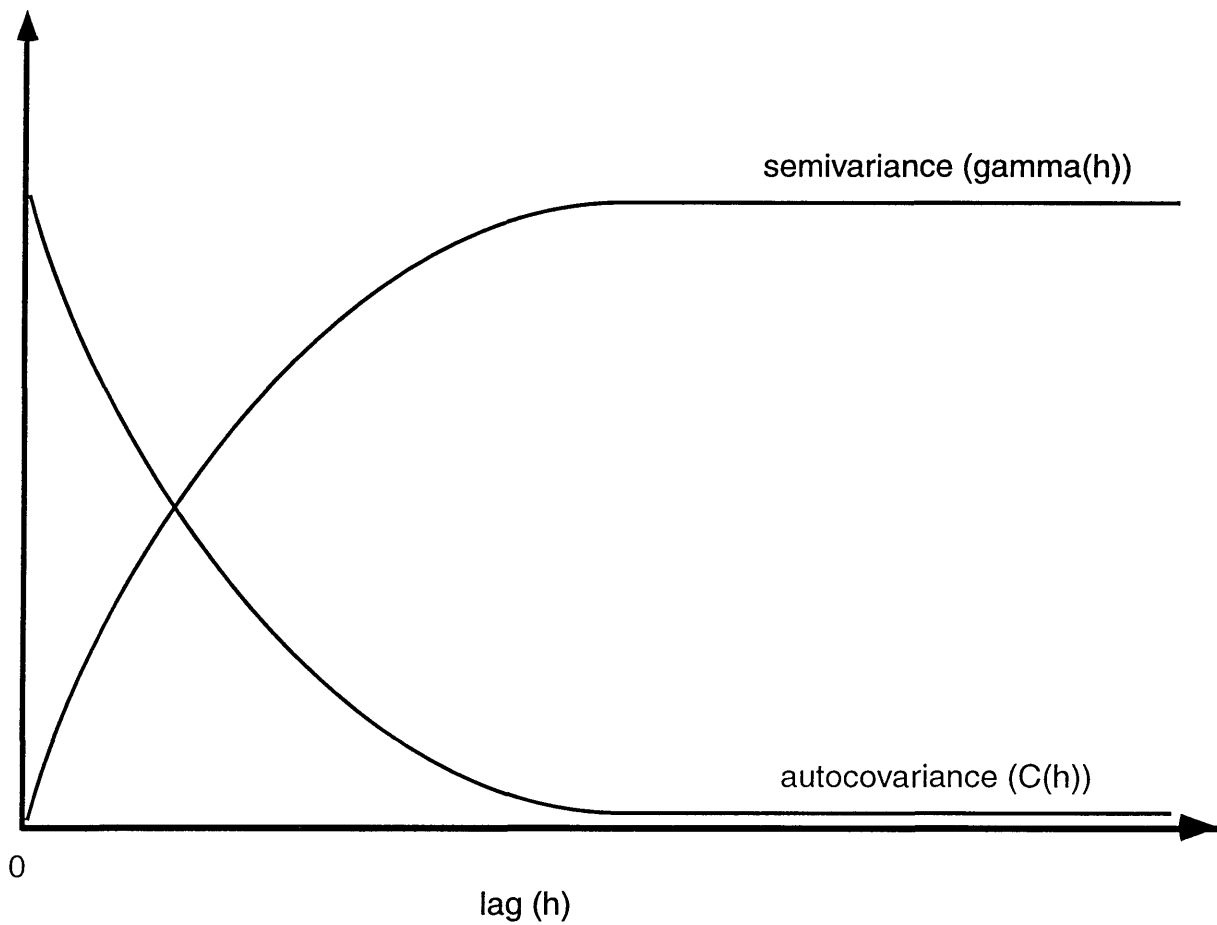
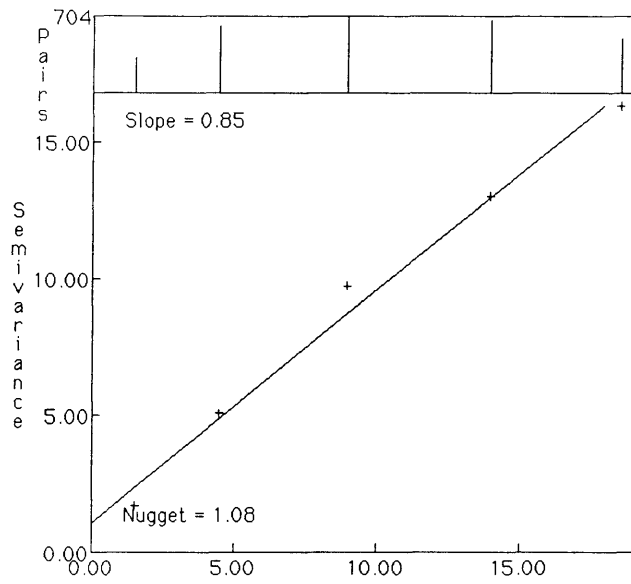
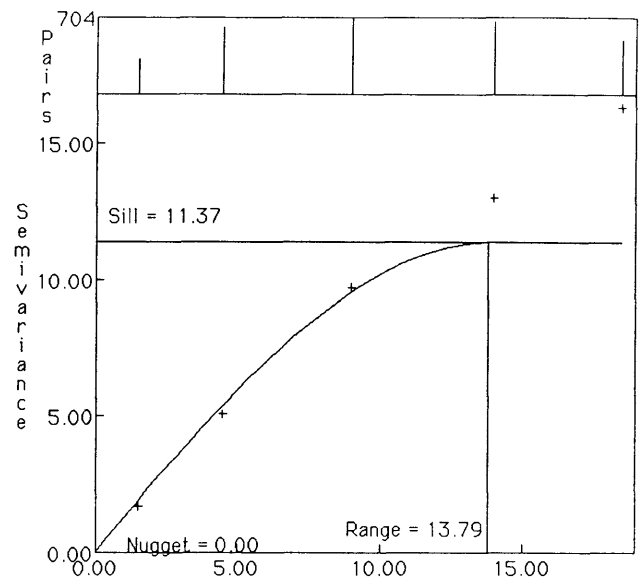


Figure 9. Relationship between the semivariance and autocovariance of a series. Autocorrelation will behave as autocovariance, however the vertical scale will be standardized $\{0 \leq y \leq 1\}$. Redrawn from Journel and Huijbregts (1978).

(a) linear model



(b) spherical model



(c) exponential model

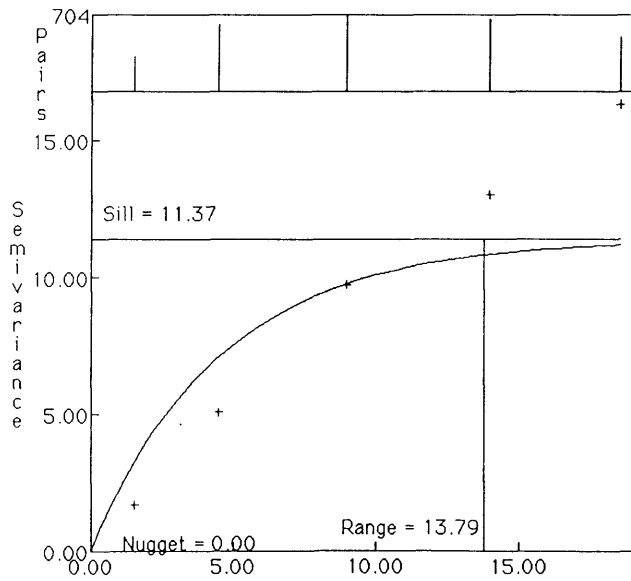


Figure 10. Models commonly applied to describe the semivariogram function: (a) linear, (b) spherical, and (c) exponential.

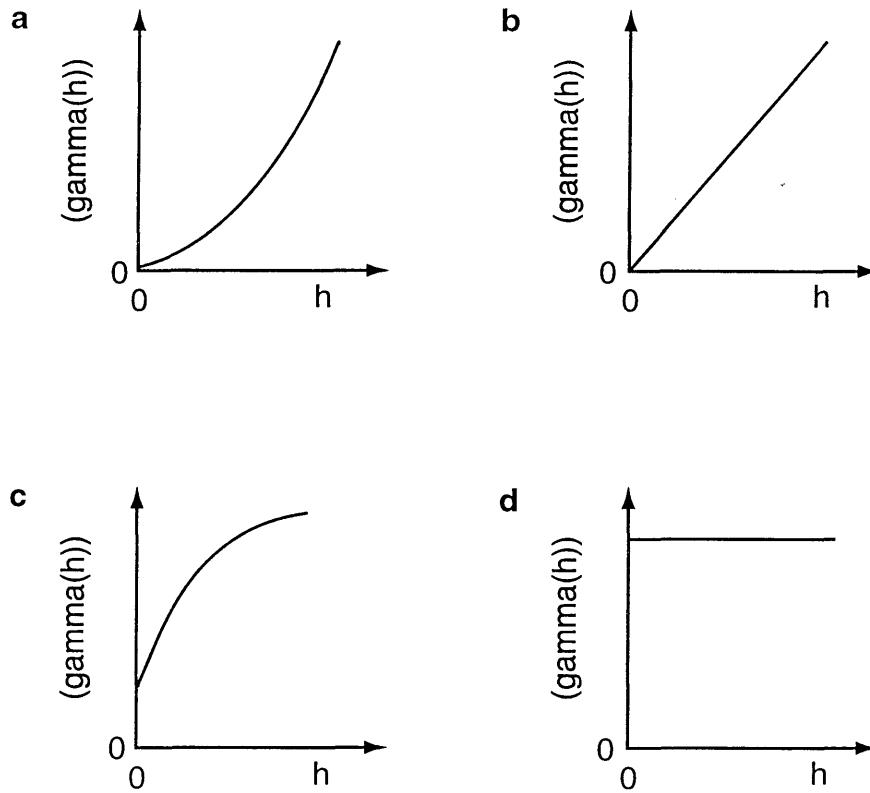


Figure 11. Semivariogram behavior at the origin, representing (a) parabolic model indicative of high degree of spatial continuity and self-affinity; (b) linear model; (c) spherical model with nugget effect; and (d) pure nugget effect. Redrawn from Journel and Huijbregts (1978).

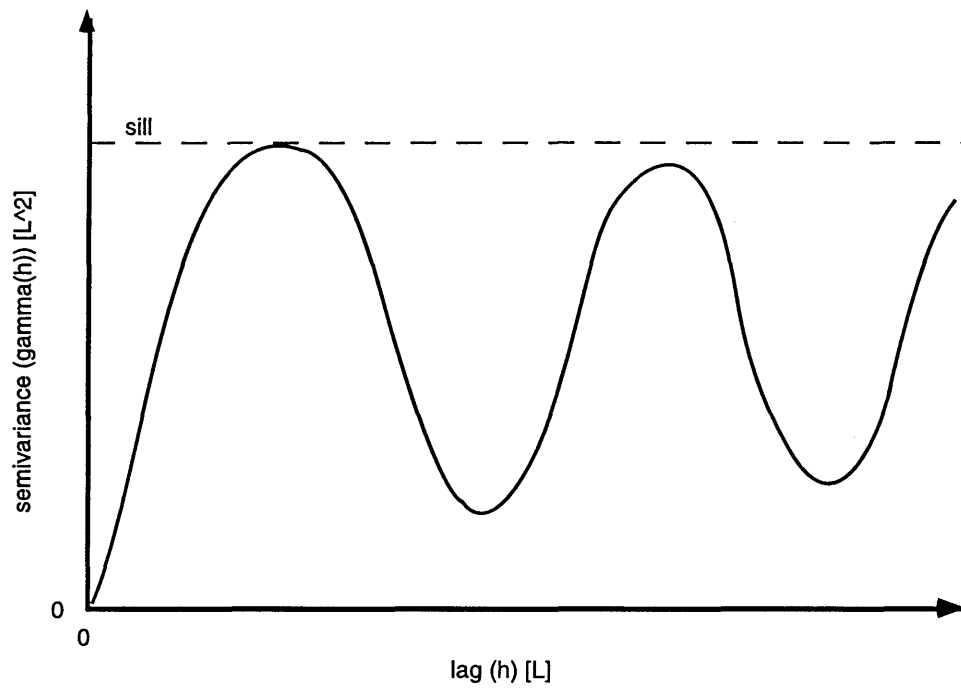


Figure 12. Semivariogram function for a periodic series revealing departure from the sill beyond the initially apparent range, and periodic semivariance.

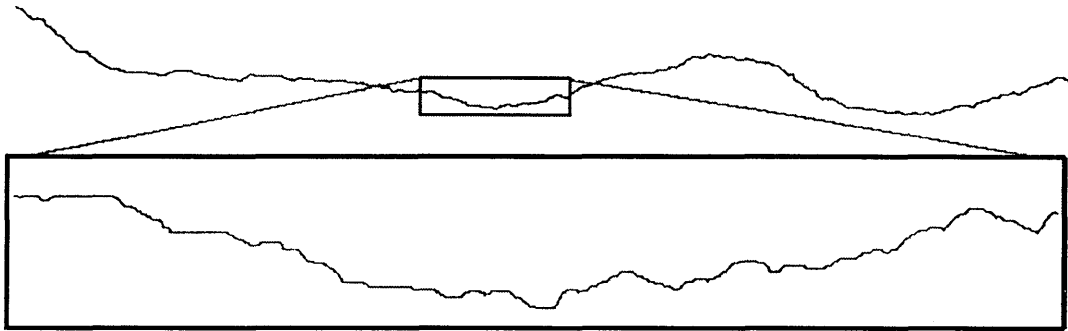


Figure 13. Direct determination of scaling behavior by comparing statistics of magnified portions of the original line to the original. Consistency between the two indicate self-similarity, whereas if an adjustment factor is necessary to rectify the two, self-affinity may hold (see Malinverno, 1989). The lower box is a 7X magnification of the smaller box which encloses a 2 cm wide section of the sediment-water interface contour.

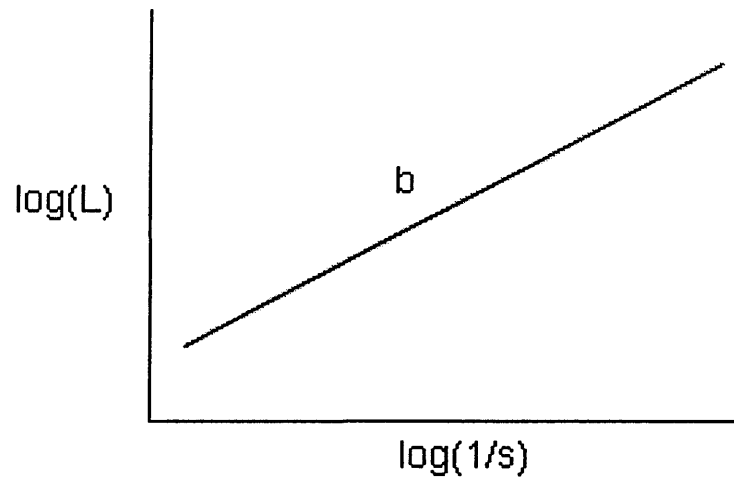


Figure 14. Idealized Richardson plot used to estimate the compass, or Hausdorff dimension (D_H). The slope of the log transformed total length (L) versus the inverse of the increment (s) used to build the measurement, gives D_H by $D_H = 1 + b$ (see Pietgen, et al., 1992).

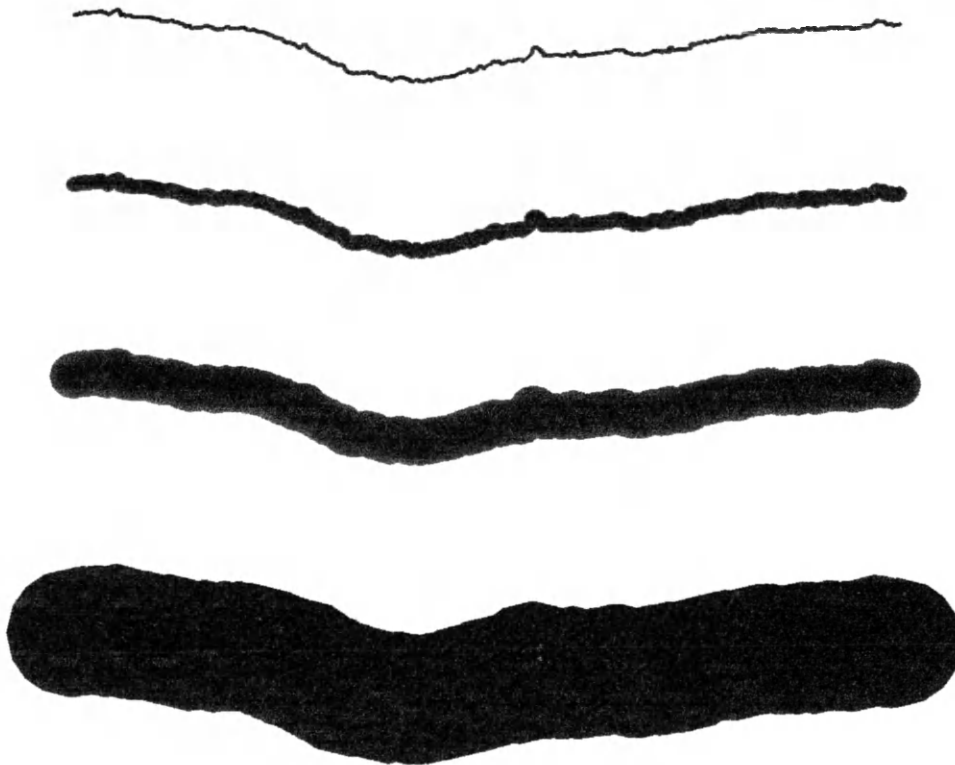
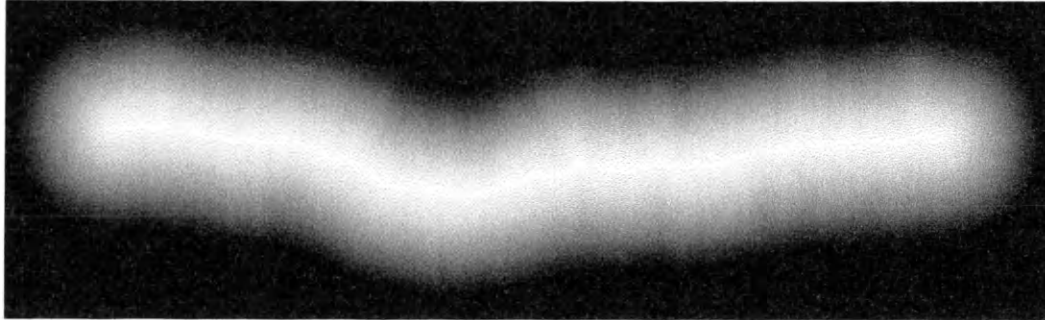
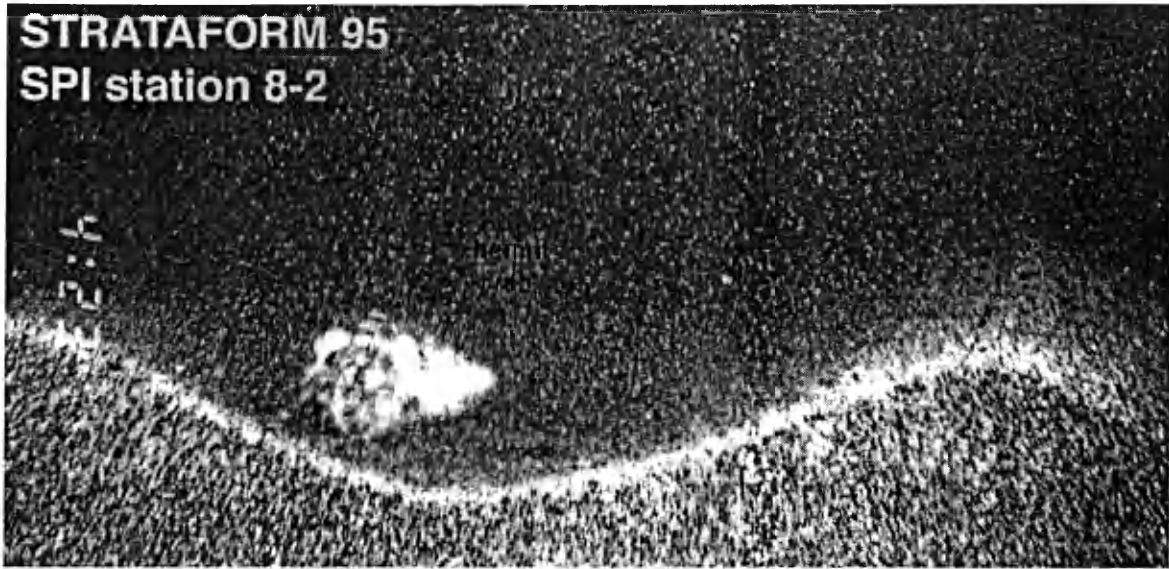


Figure 15. Procedure for estimating the Minkowski Dimension using the Euclidean distance map (EDM).

a



b

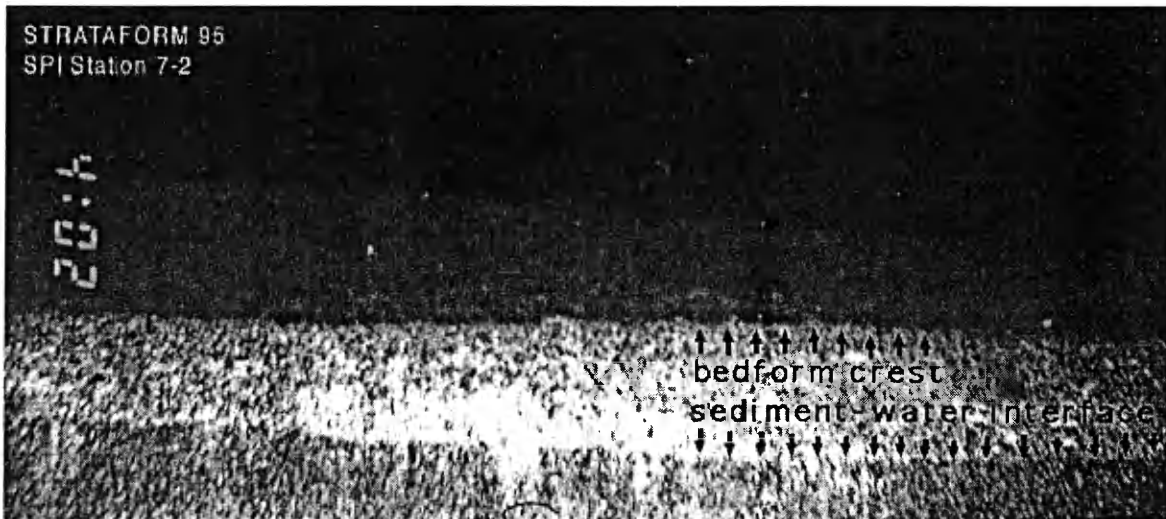


Figure 16. Sediment profile images from different azimuthal angles with the seafloor, indicative of anisotropic roughness features at some locations: (a) perpendicular to and (b) parallel to crest strike.

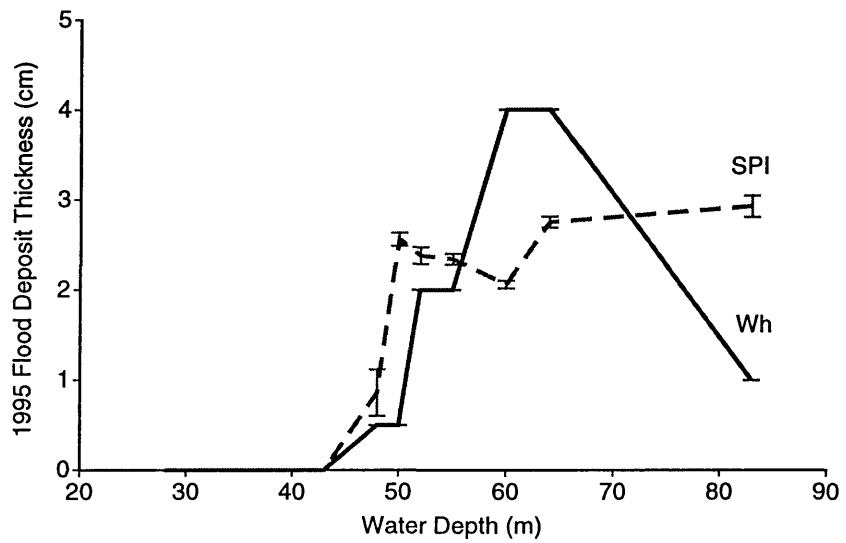


Figure 17. 1995 Eel River flood deposit layer thickness estimated from Wheatcroft (1996) (Wh) and sediment profile images (SPI). Error bars indicate +/- one standard error on the mean.

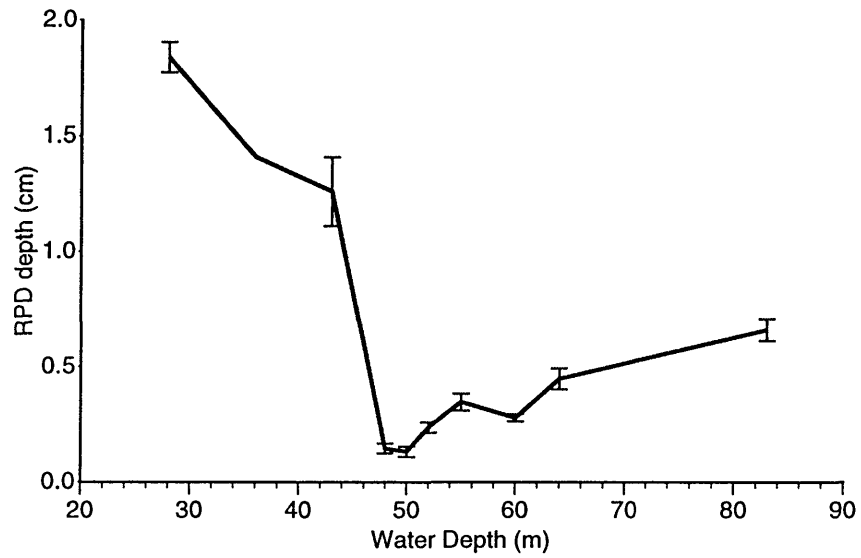


Figure 18. Apparent color redox potential discontinuity layer (RPD) depth by water depth. Error bars indicate +/- one standard error on the mean.

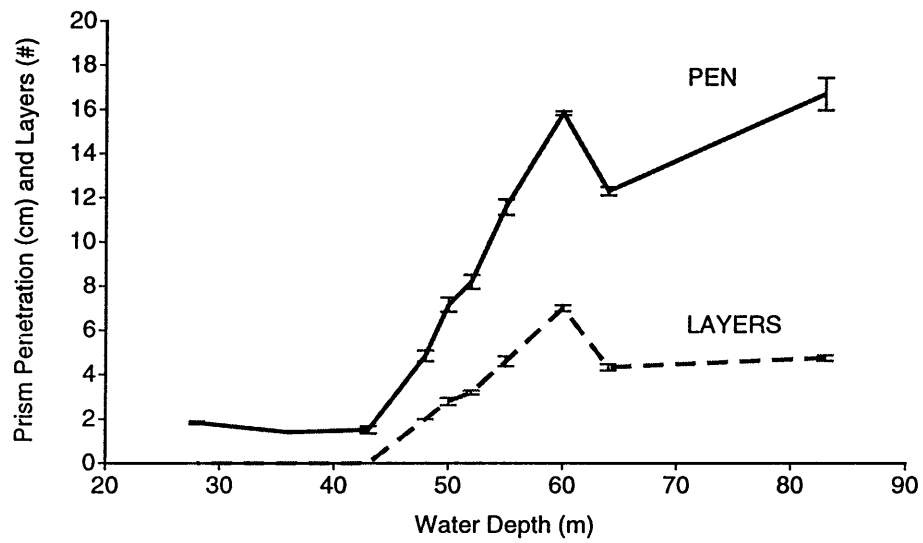


Figure 19. SPI prism penetration depth (PEN) and number of depositional layers visible (LAYERS) by water depth. Error bars indicate +/- one standard error on the mean.

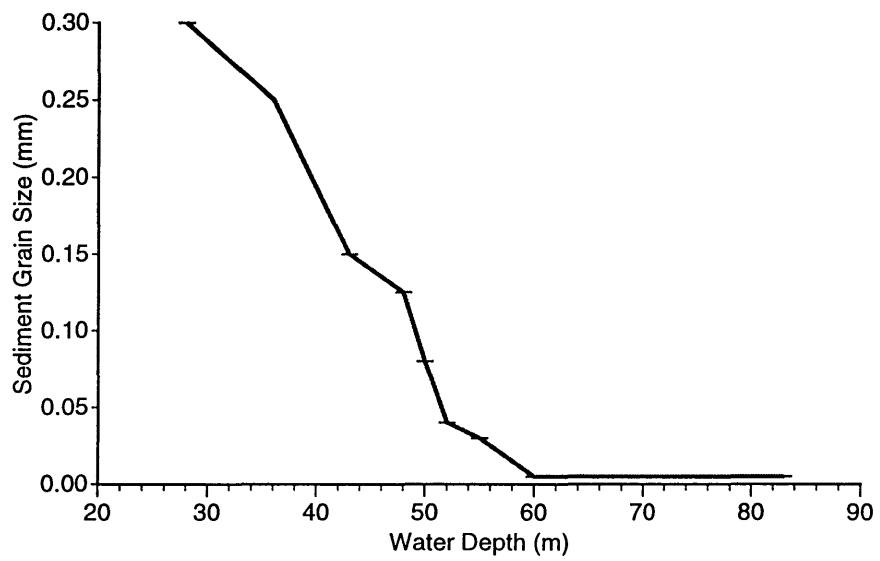


Figure 20. Approximate modal sediment grain size (mm) determined from SPI by water depth. Error bars indicate +/- one standard error on the mean.

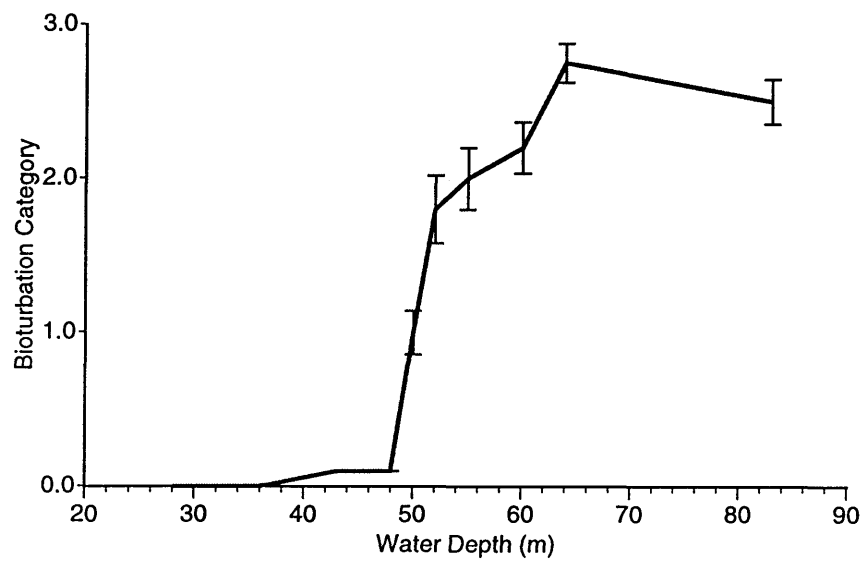


Figure 21. Degree of bioturbation by water depth. Category values indicate: 0 = none, 0.1 = trace or negligible, 1 = low, 2 = moderate, 3 = high. Error bars indicate +/- one standard error on the mean.

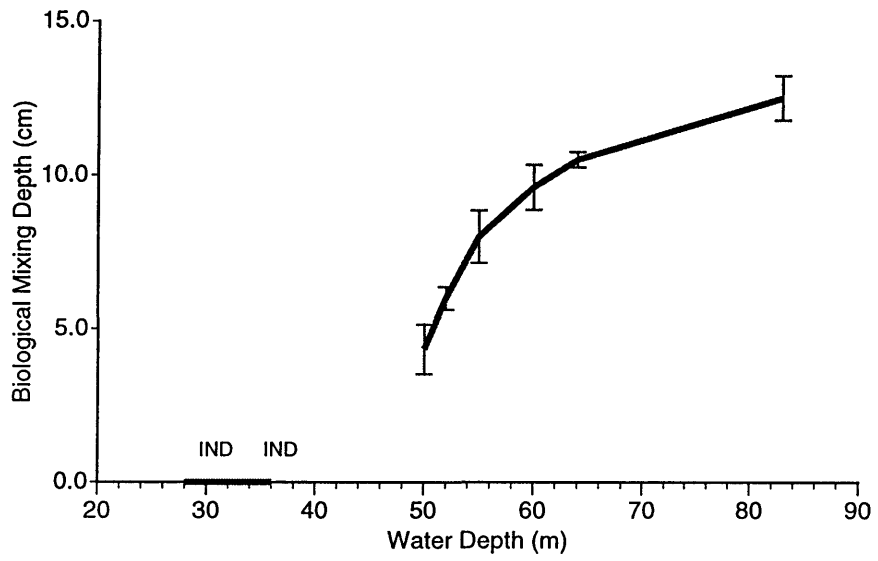


Figure 22. Biologically mixed depth (cm) of sediments determined from SPI. Error bars indicate +/- one standard error on the mean.

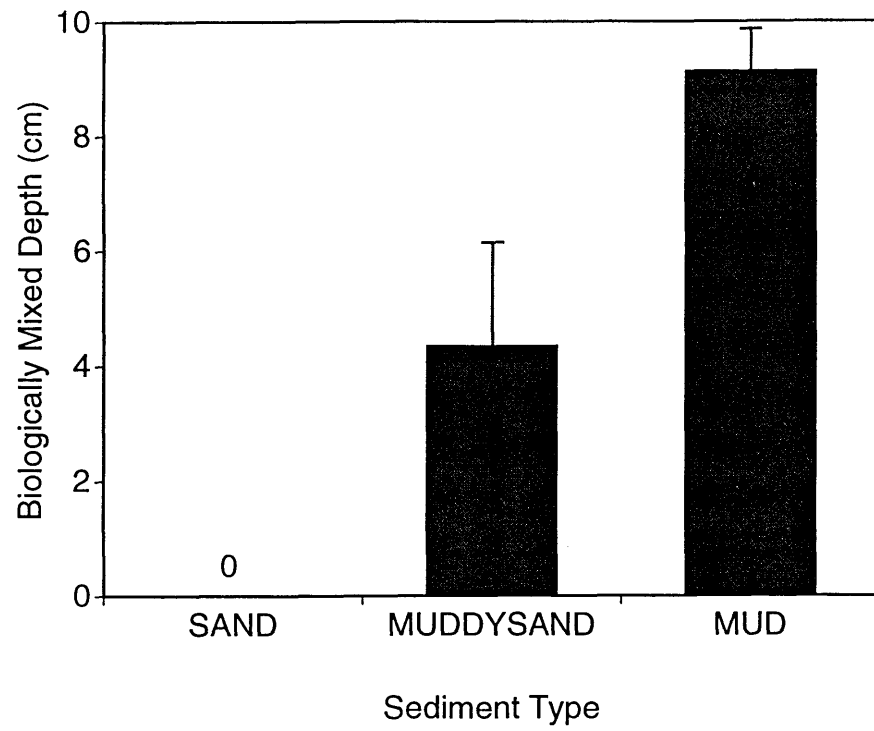


Figure 23. Biologically mixed depth (cm) by sediment type. Error bars indicate +/- one standard error on the mean.

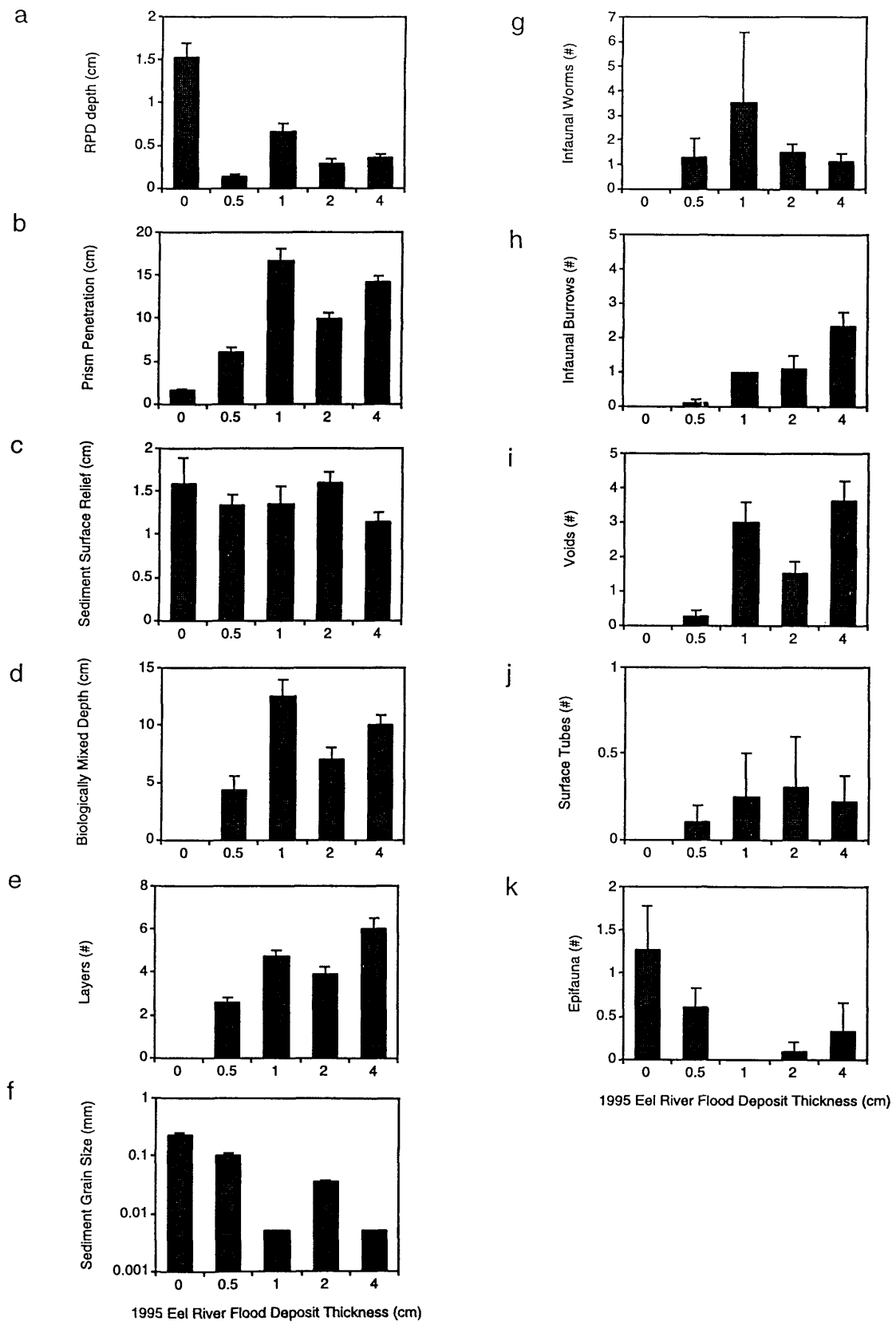


Figure 24. SPI habitat parameters by Eel River 1995 flood deposit layer thickness.

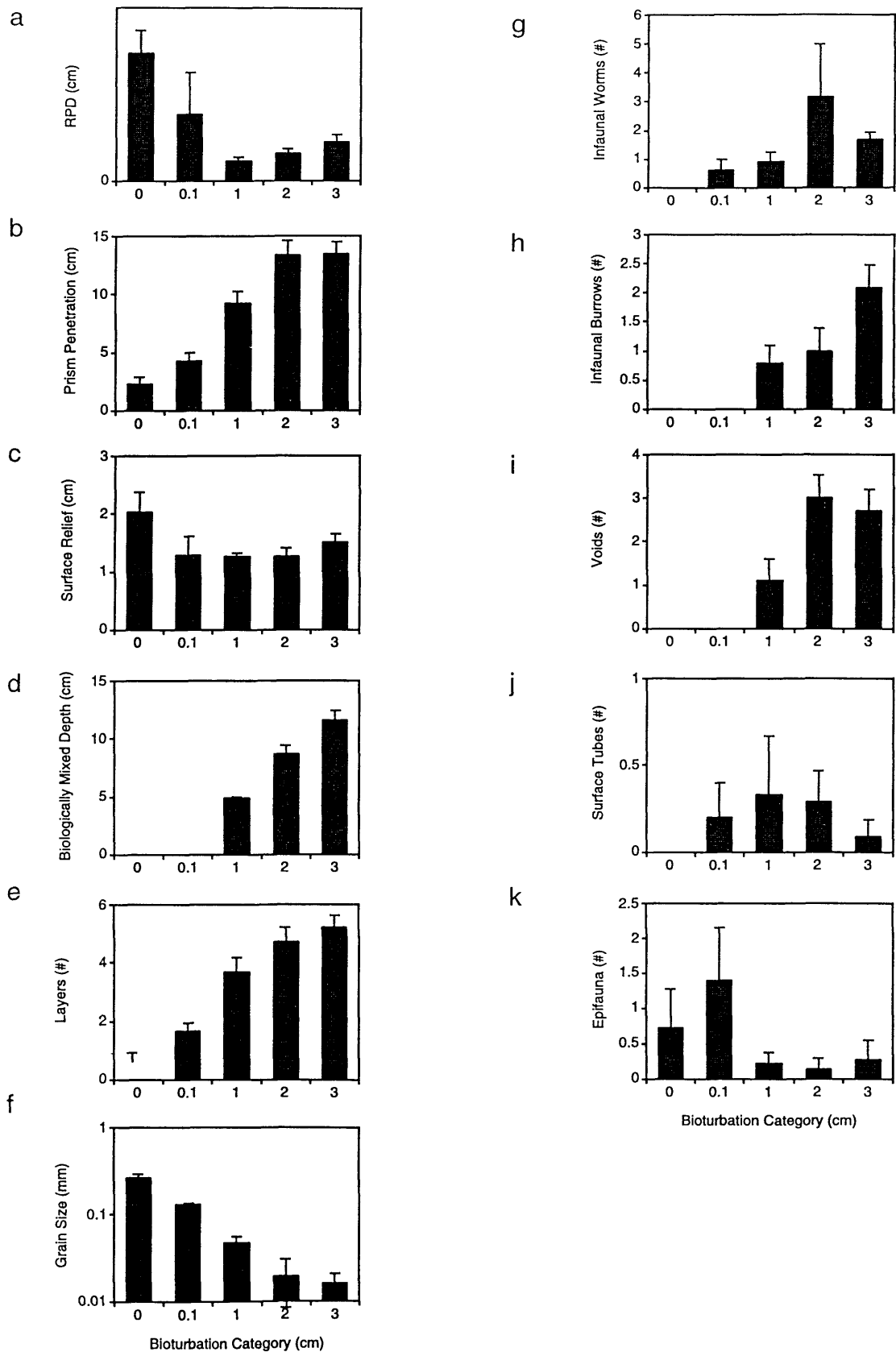


Figure 25. SPI habitat parameters in relation to bioturbation category.

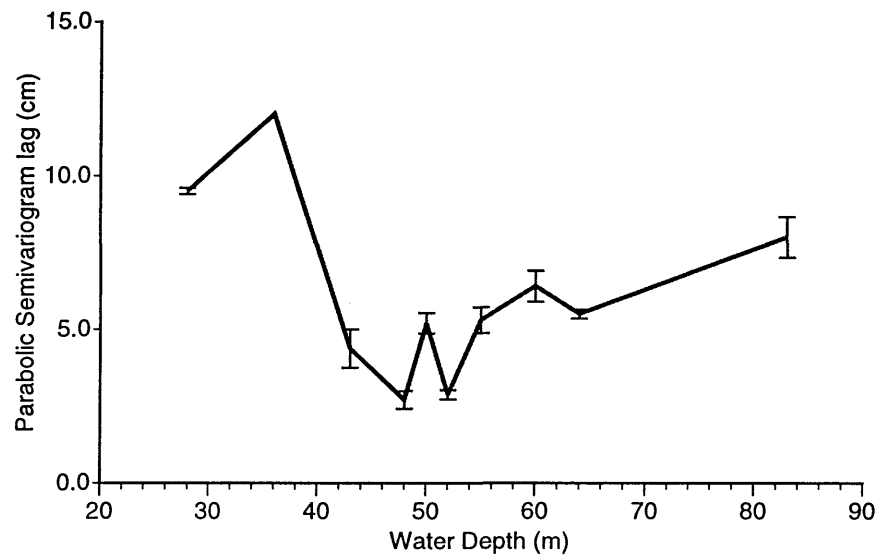


Figure 26. Distance lag over which parabolic or power-law behavior of the semivariogram function was observed by water depth. Error bars indicate +/- one standard error on the mean.

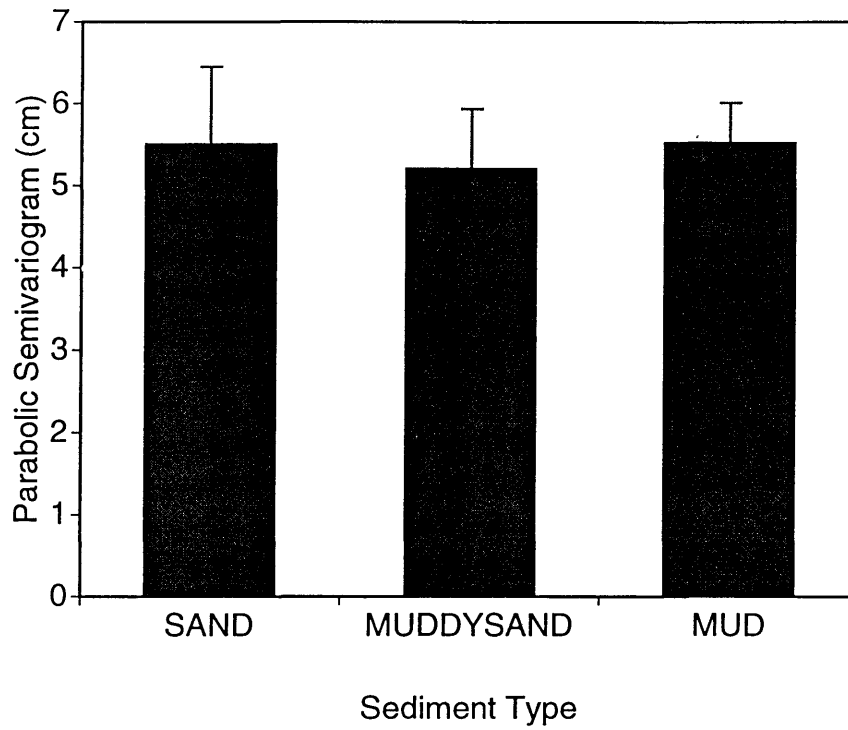


Figure 27. Distance lag over which parabolic or power-law behavior of the semivariogram function was observed by sediment type. Error bars indicate +/- one standard error on the mean.

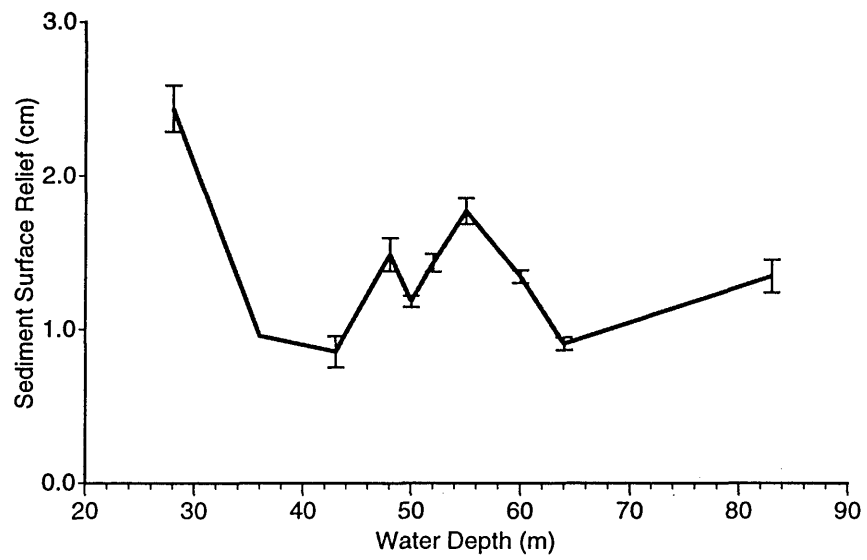


Figure 28. Surface relief (vertical linear extrema) (cm) of sediment-water interface elevations by water depth. Error bars indicate +/- one standard error on the mean.

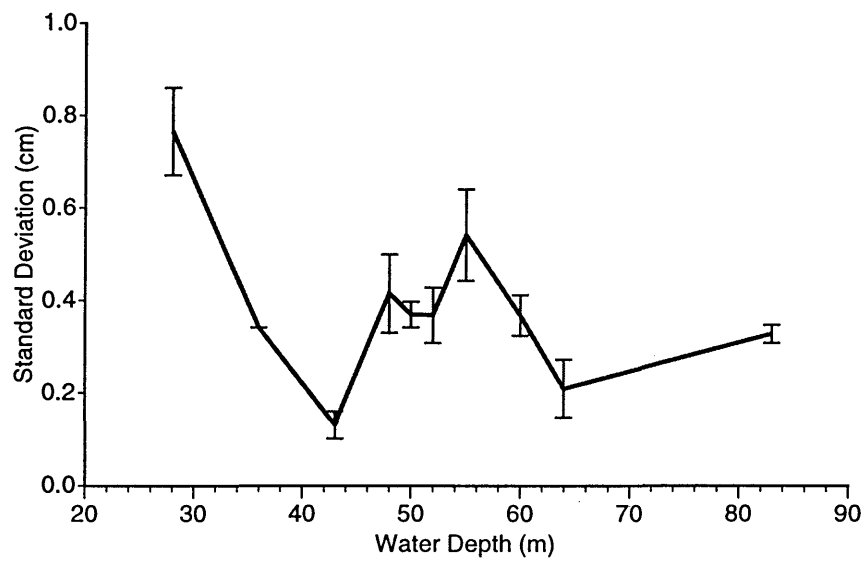


Figure 29. Standard deviation (cm) of sediment-water interface elevations by water depth. Error bars indicate +/- one standard error on the mean.

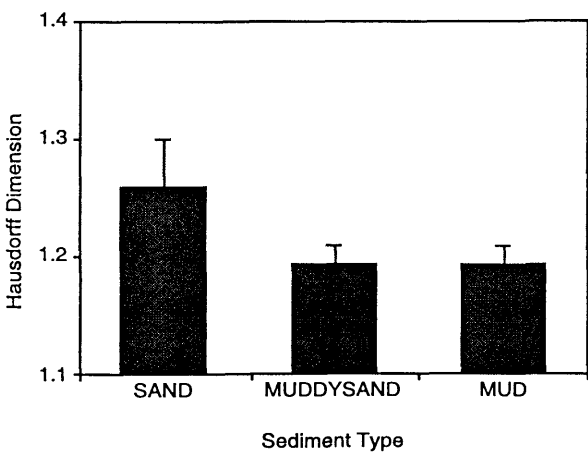
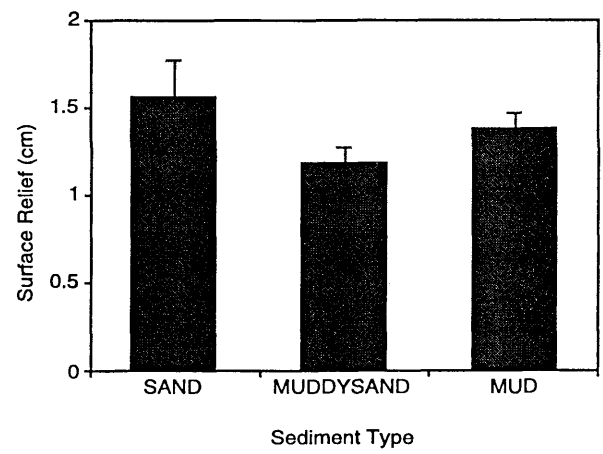
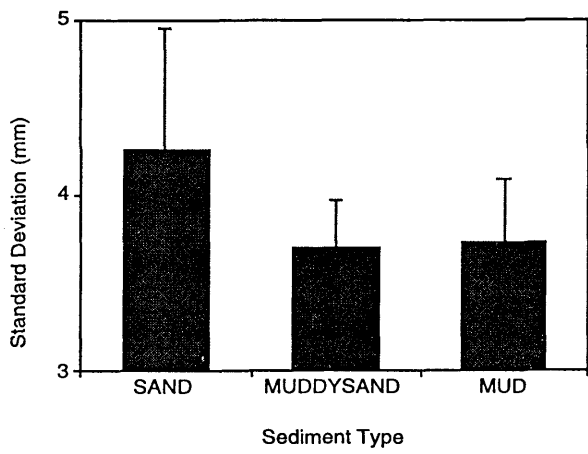
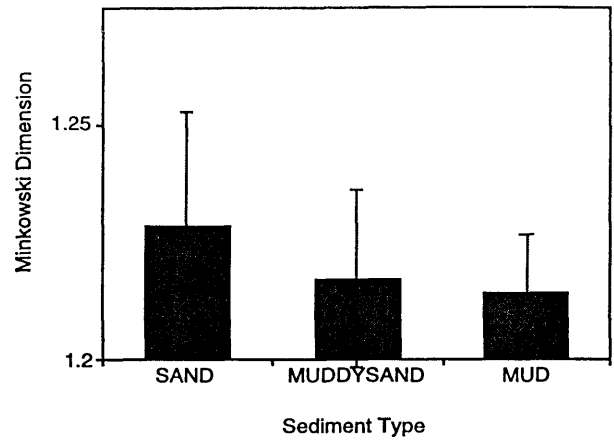
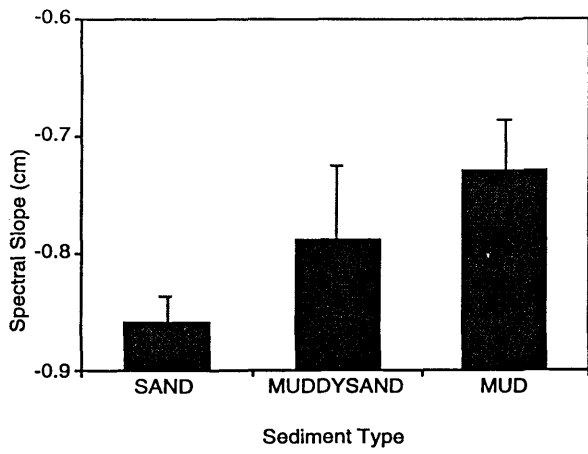


Figure 30. Sediment-water interface roughness parameters by sediment type.

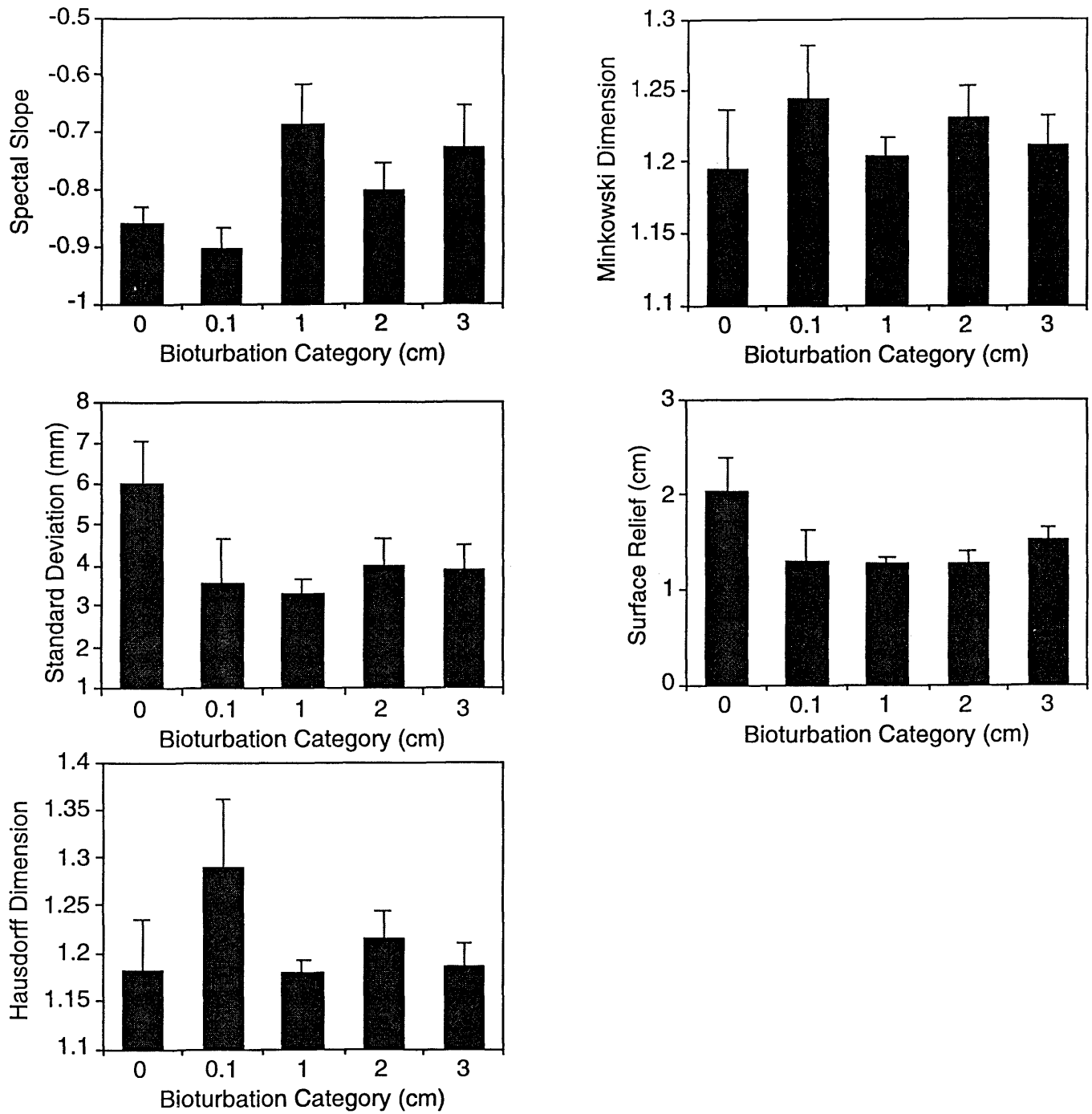


Figure 31. Sediment-water interface roughness parameters by degree of bioturbation.

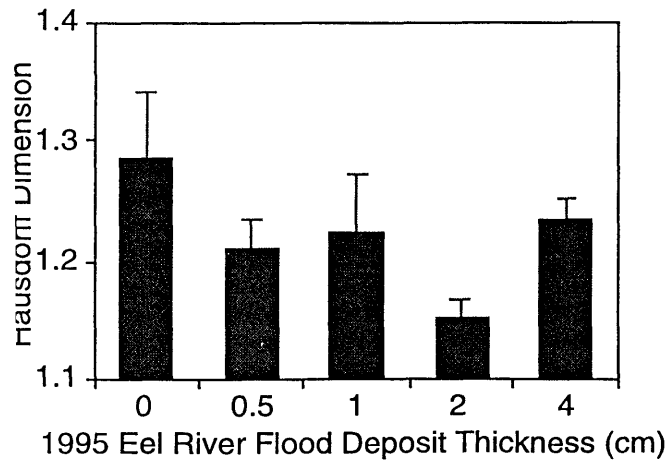
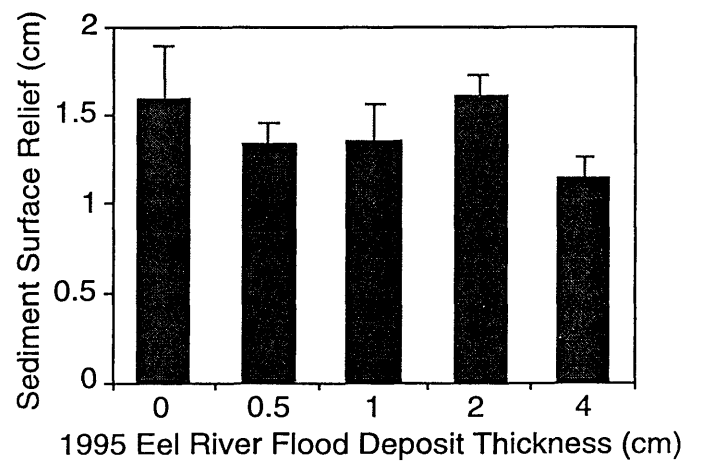
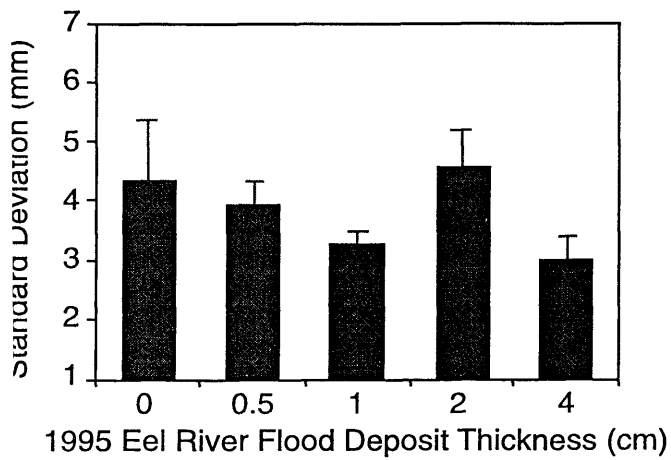
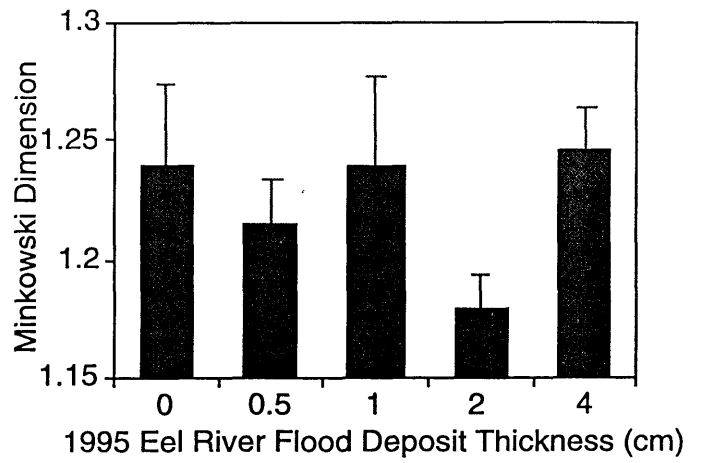
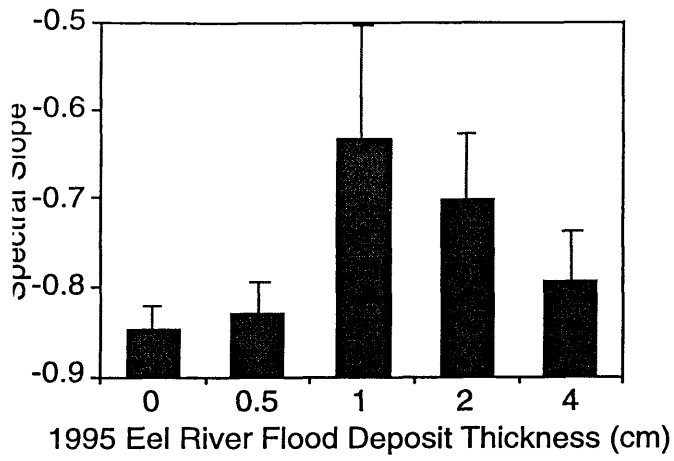


Figure 32. Sediment-water interface roughness parameters by 1995 Eel River Flood deposit thickness.

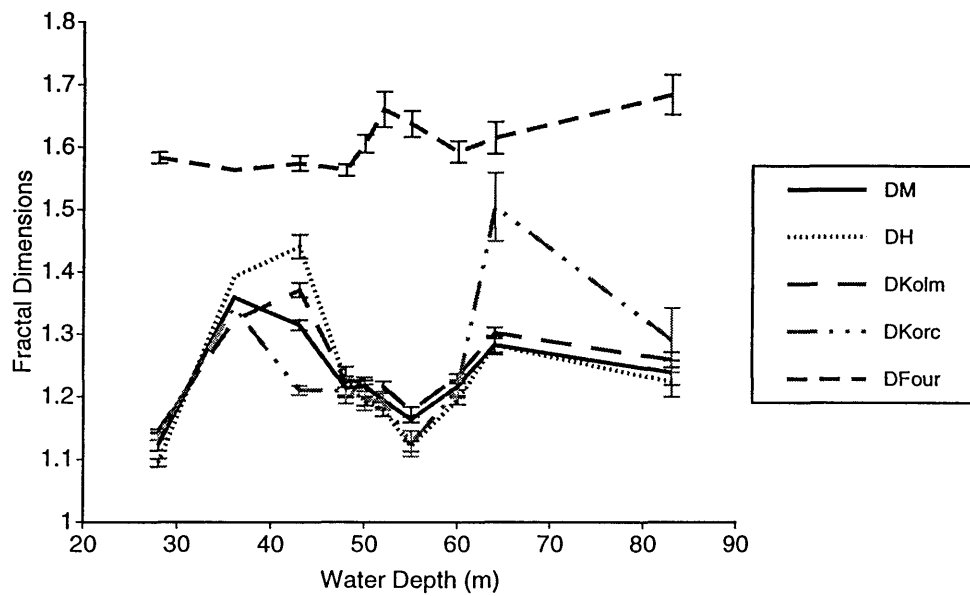


Figure 33. Fractal dimension estimates by water depth: Minkowski dimension (DMink), Hausdorff dimension (DH), Kolmogorov dimension (DKolm), Korcak dimension (DKorc), and Fourier fractal dimension (DFour). Error bars indicate +/- one standard error on the mean.

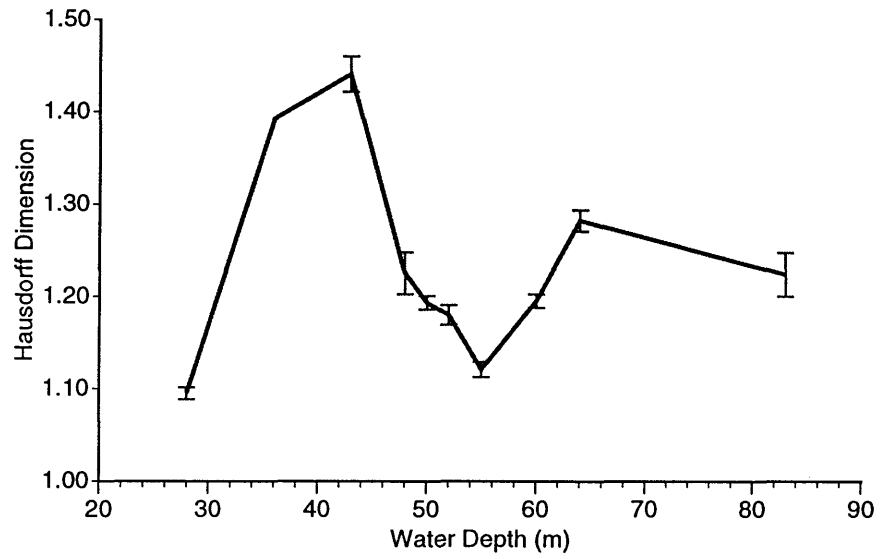


Figure 34. Hausdorff dimension estimates by water depth. Error bars indicate +/- one standard error on the mean.

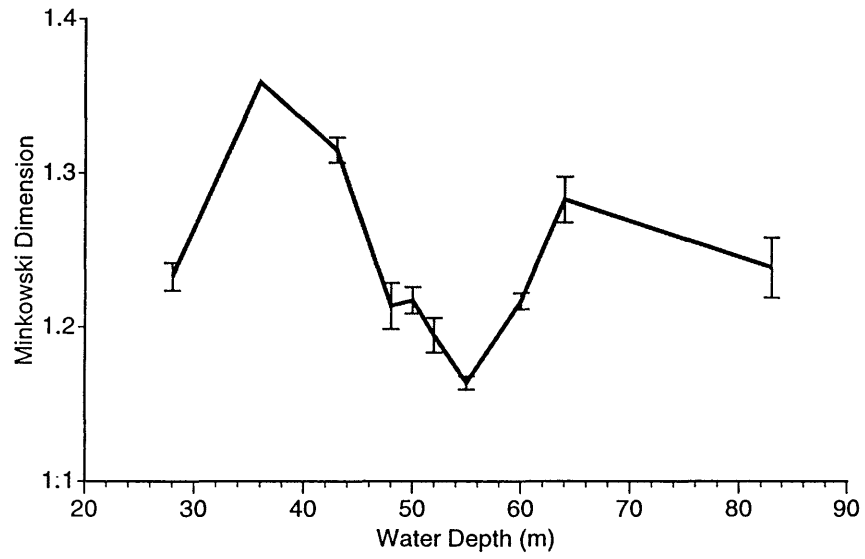


Figure 35. Minkowski dimension estimates by water depth. Error bars indicate +/- one standard error on the mean.

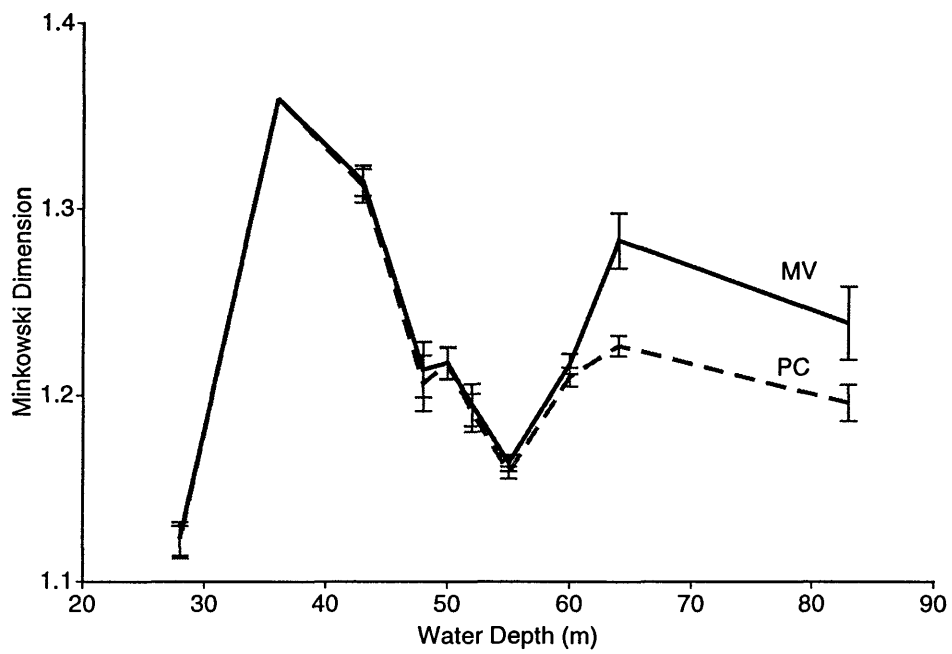


Figure 36. Minkowski dimension estimates for multivalued (MV) and piecewise continuous (PC) sediment-water interface contours by water depth. Error bars indicate +/- one standard error on the mean.

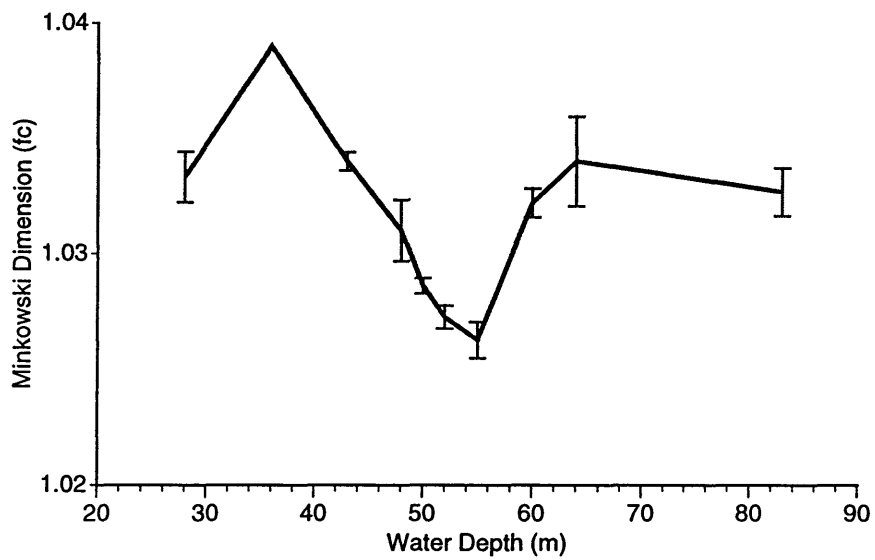


Figure 37. Minkowski dimension estimates calculated using Fractal Calculator macros for *NIH Image* by water depth. Error bars indicate +/- one standard error on the mean.

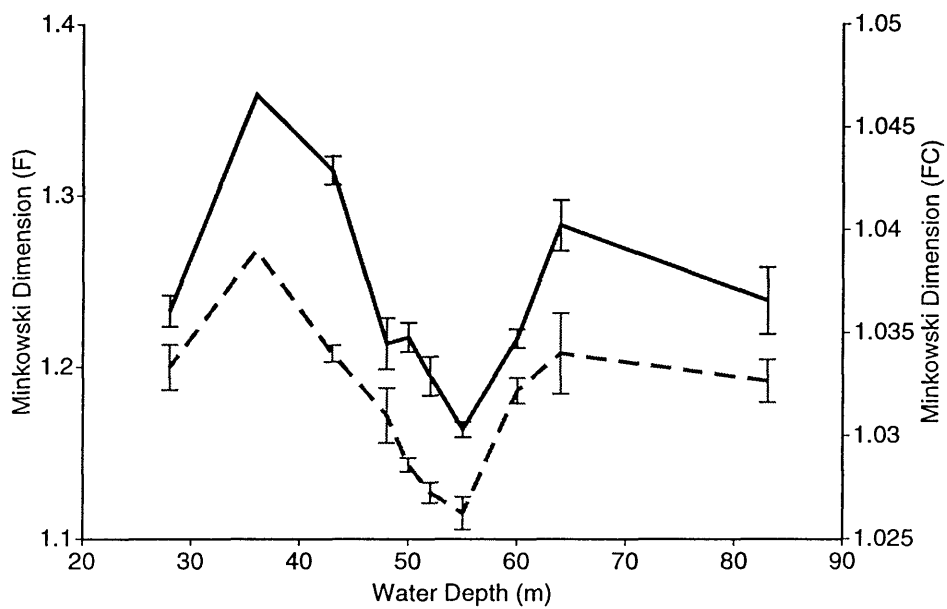


Figure 38. Minkowski dimension estimates by water depth. Minkowski dimension (F) calculated using *Fractals* (Russ, 1995), and Minkowski dimension (FC) calculated using Fractal Calculator macros for *NIH Image* employing Euclidean Distance Map method. Error bars indicate +/- one standard error on the mean.

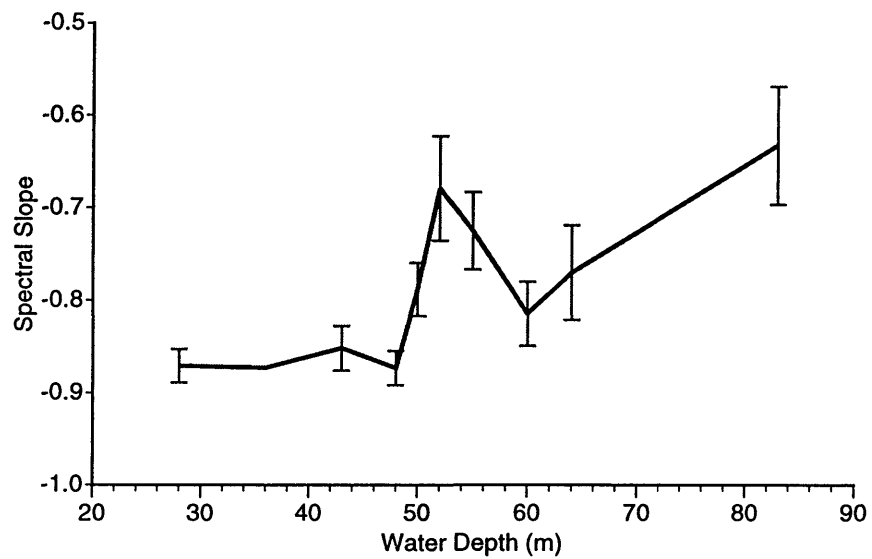


Figure 39. Fourier spectral slope for sediment-water interface profiles by water depth. Error bars indicate +/- one standard error on the mean.

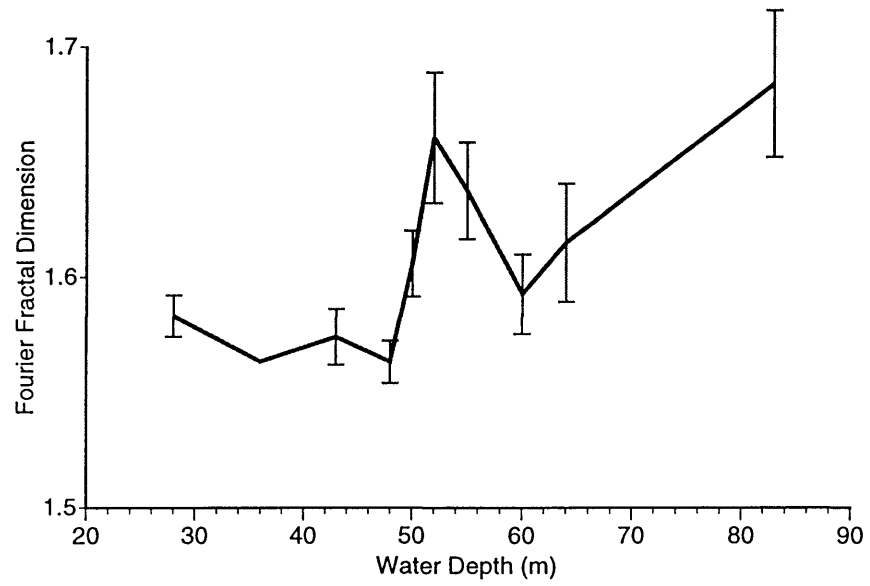


Figure 40. Fourier fractal dimension estimates using slopes of spectra by water depth. Error bars indicate +/- one standard error on the mean.

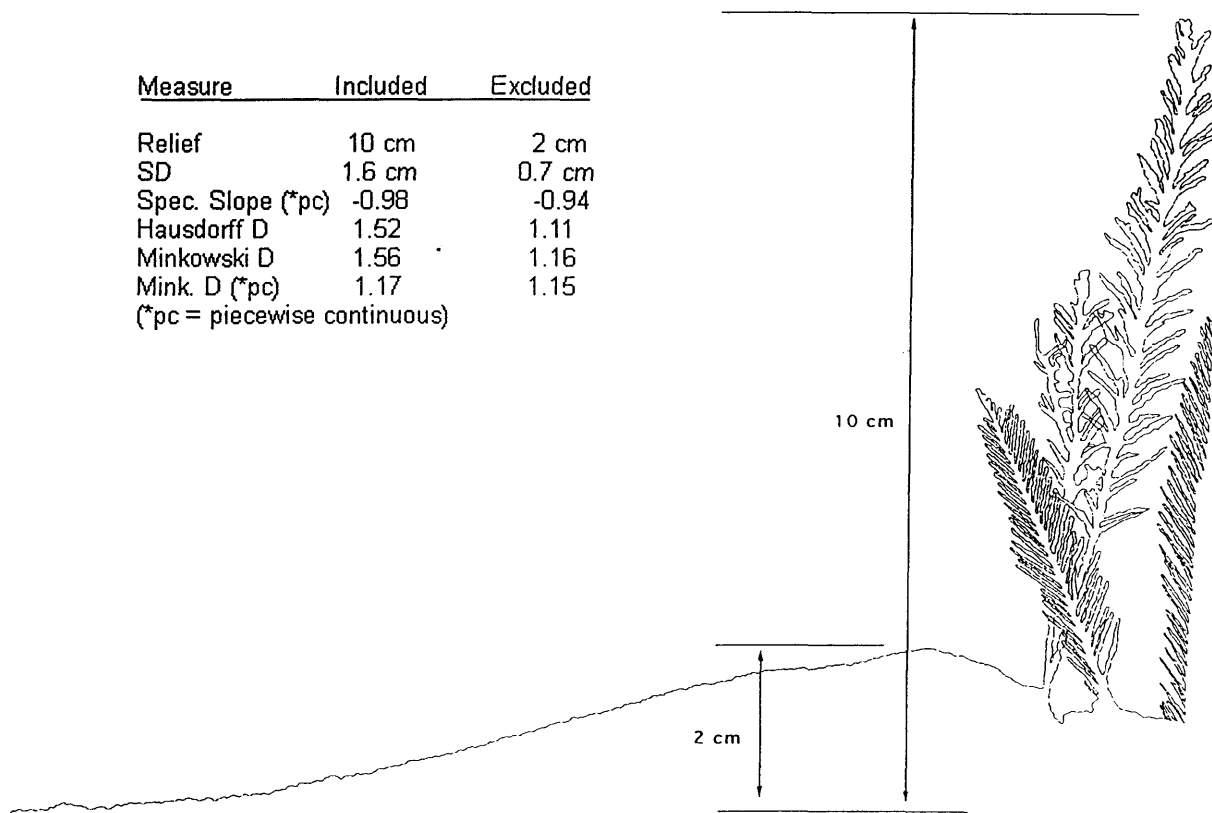


Figure 41. Influence of epifaunal anthozoans upon measurements.

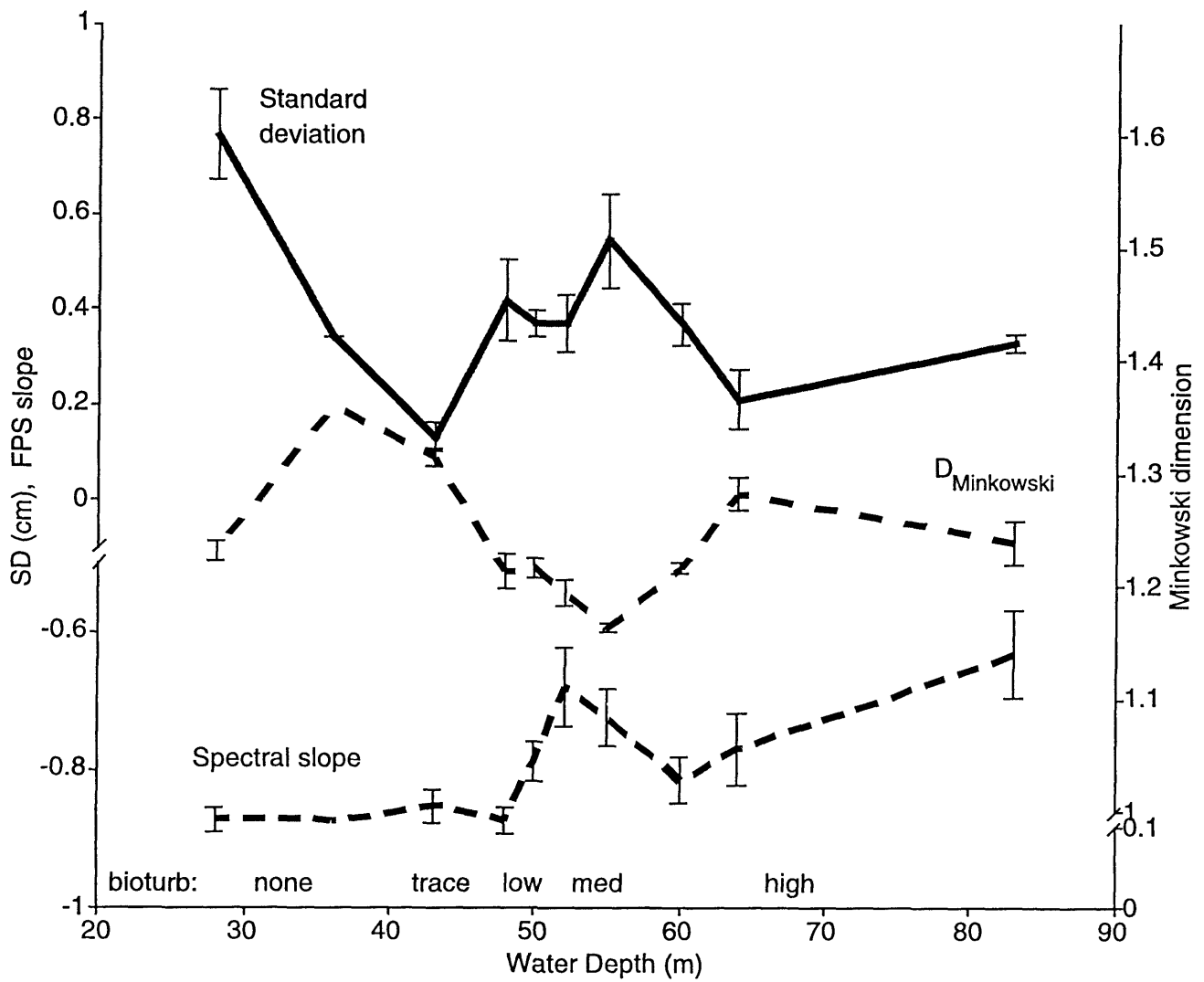


Figure 42. Sediment-water interface standard deviation, Minkowski dimension, and Fourier power spectra slopes by water depth.

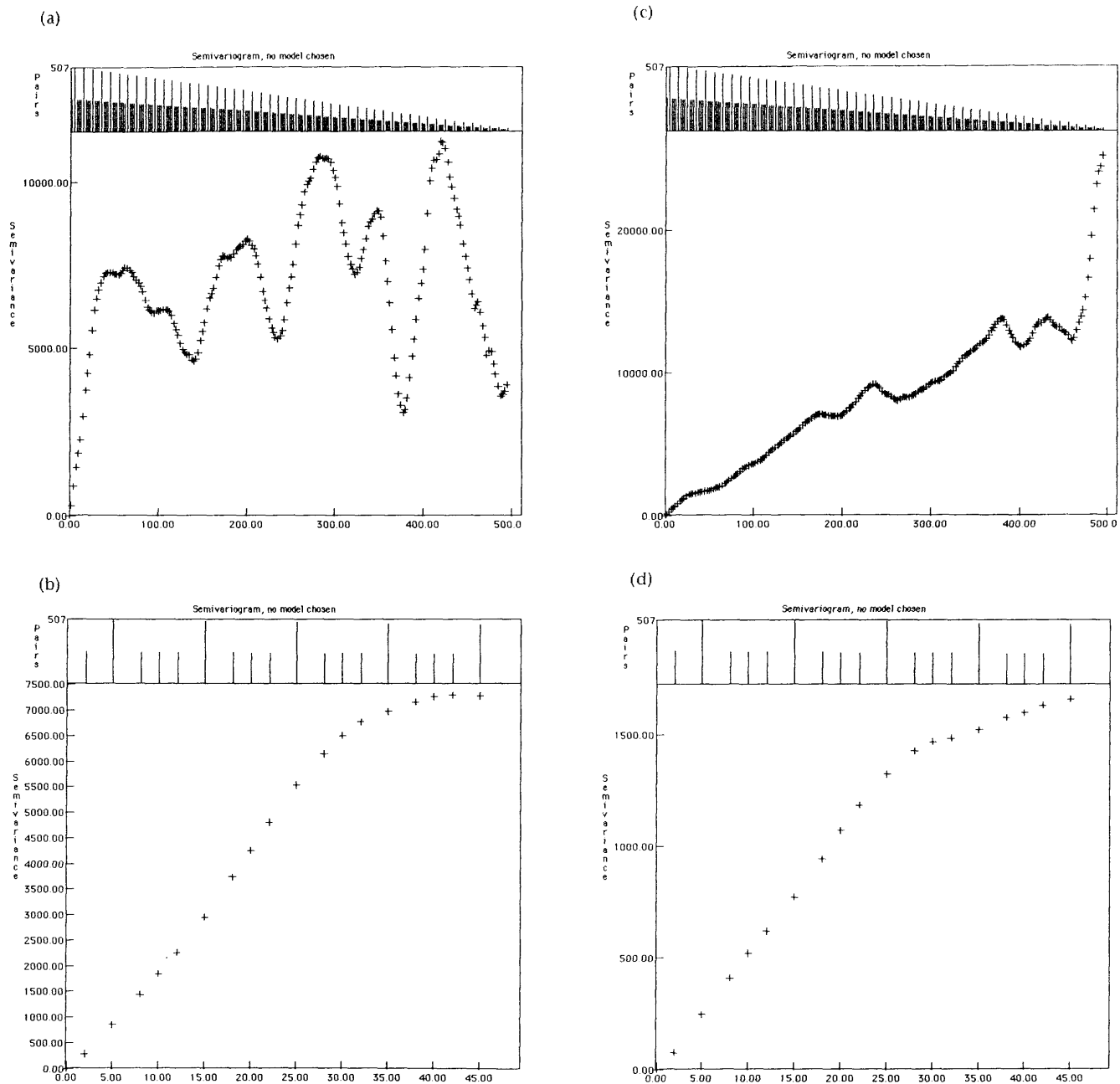
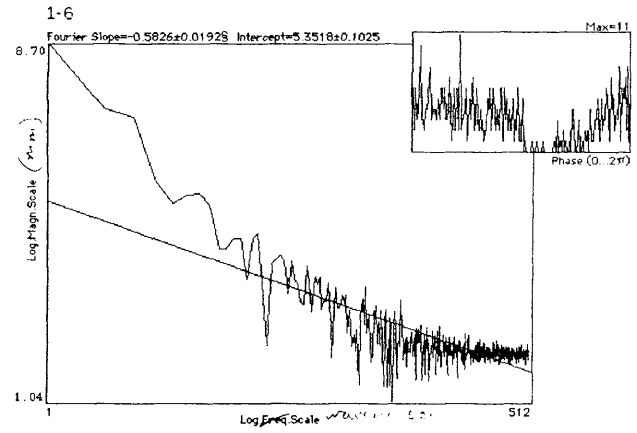
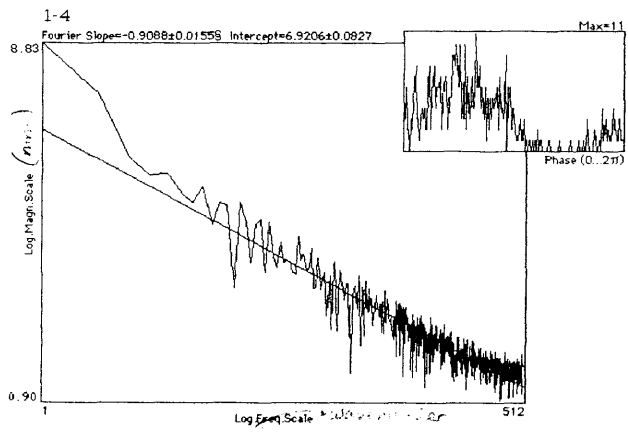
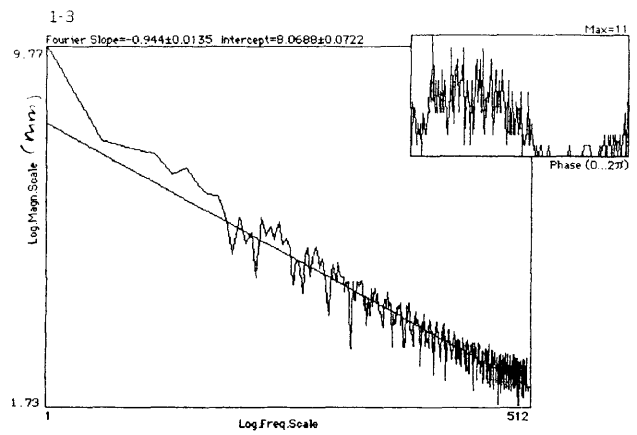
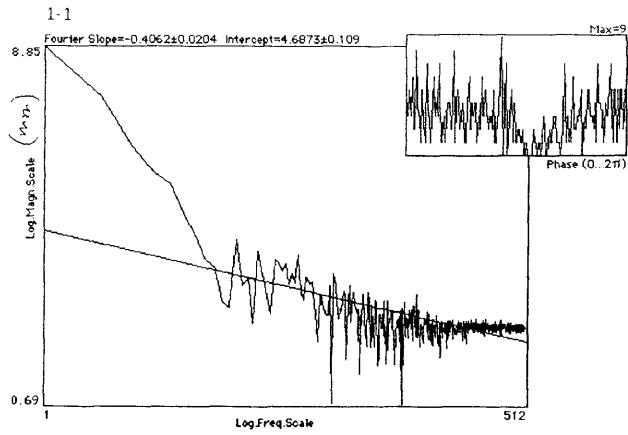
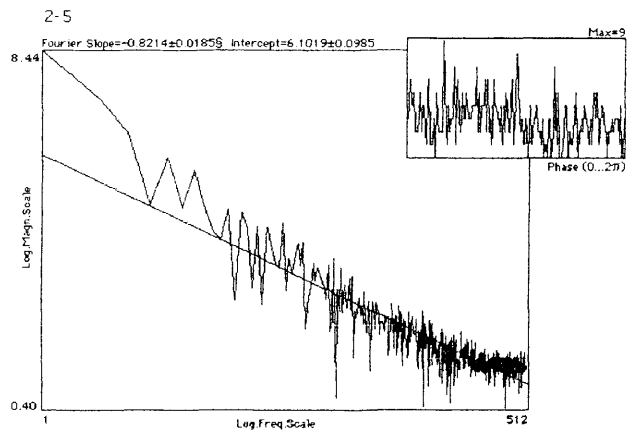
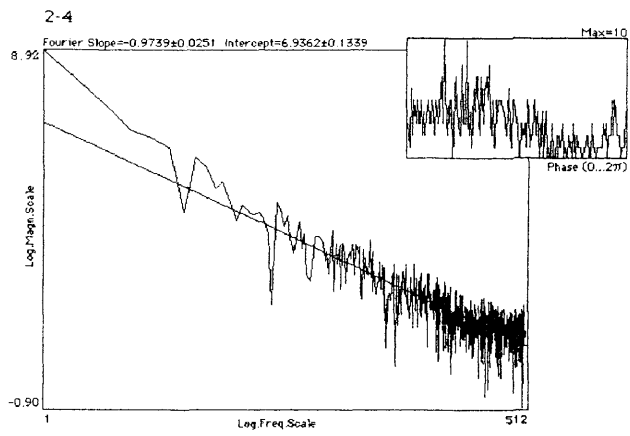
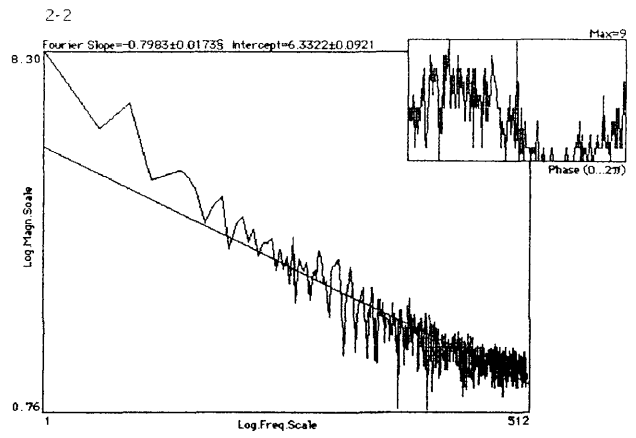
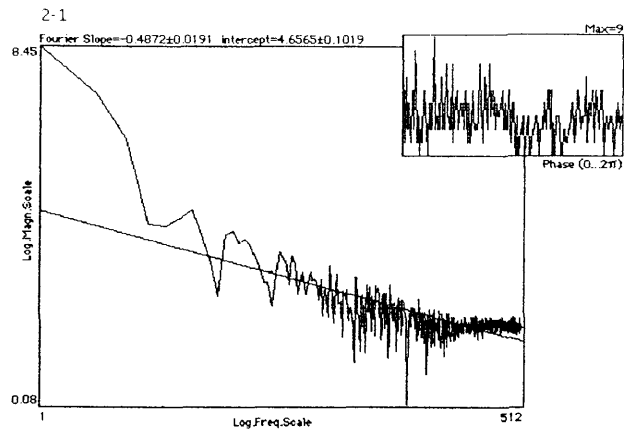
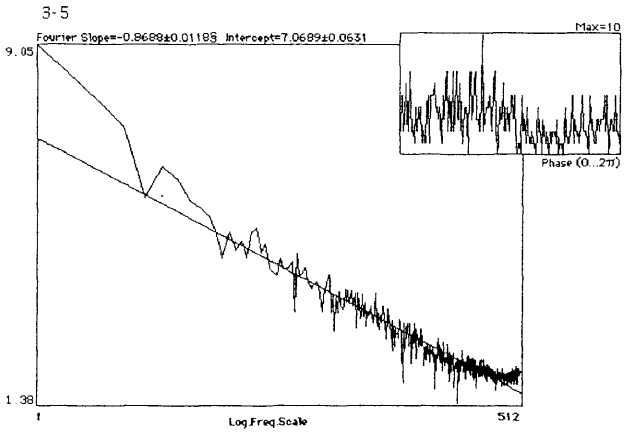
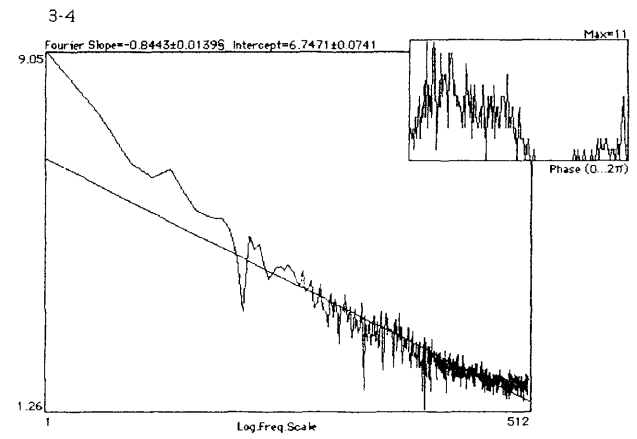
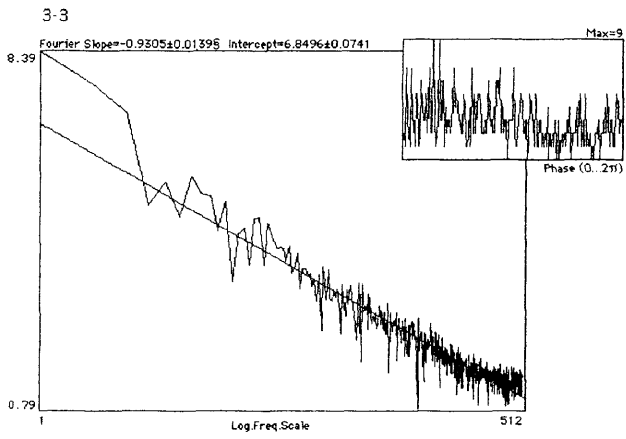
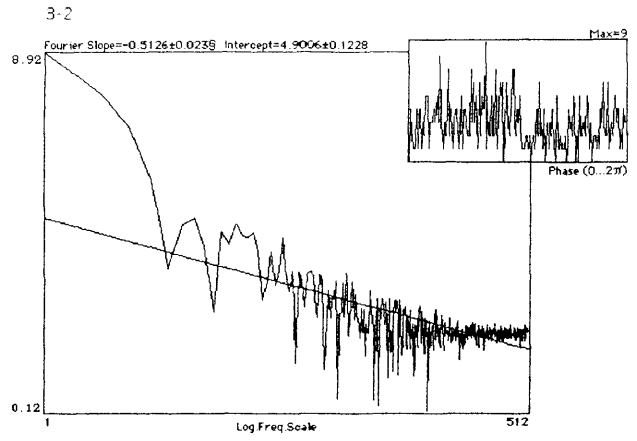
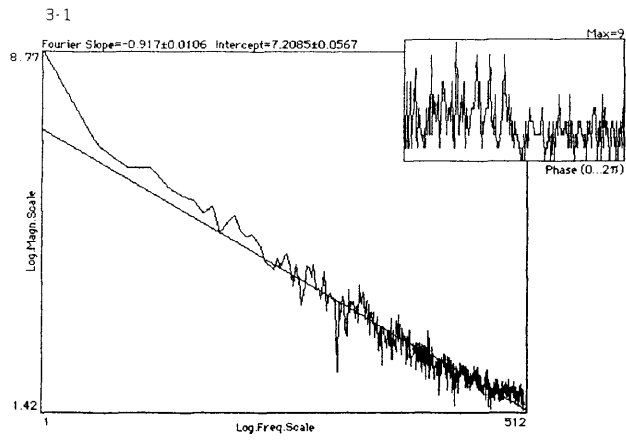
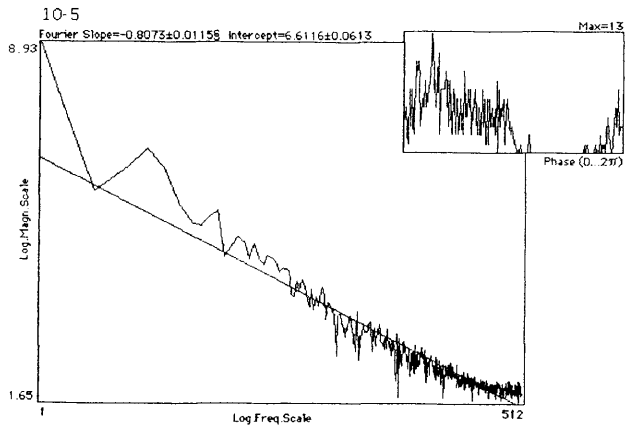
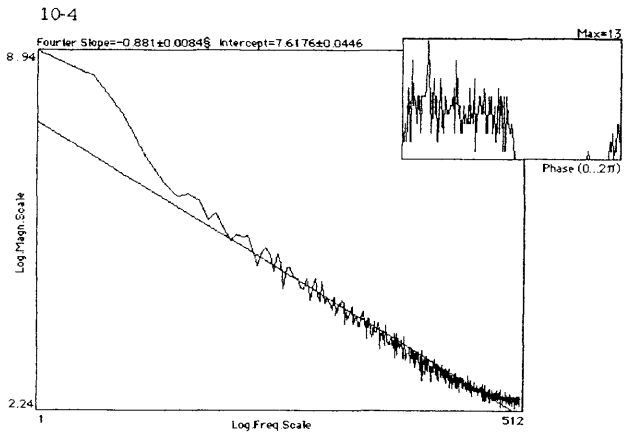
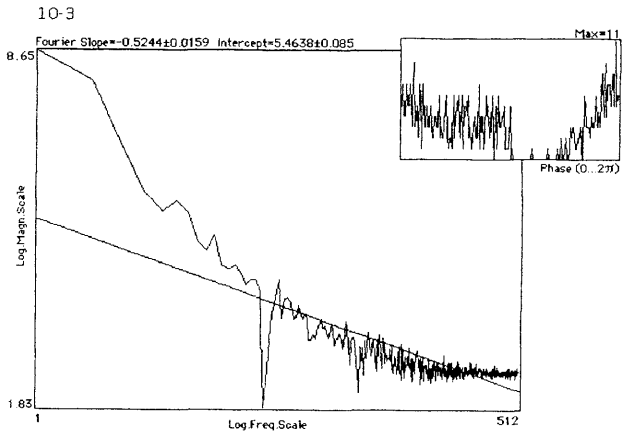
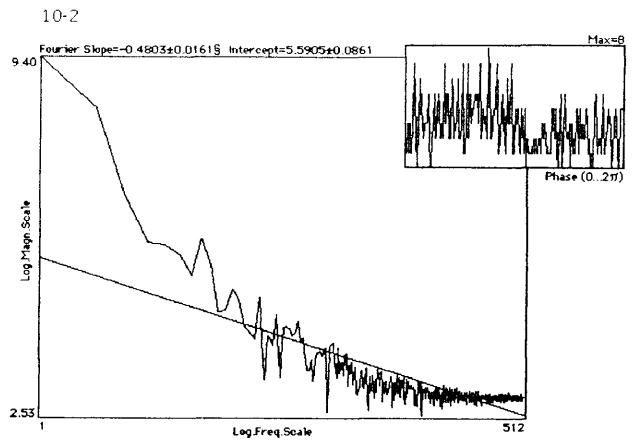
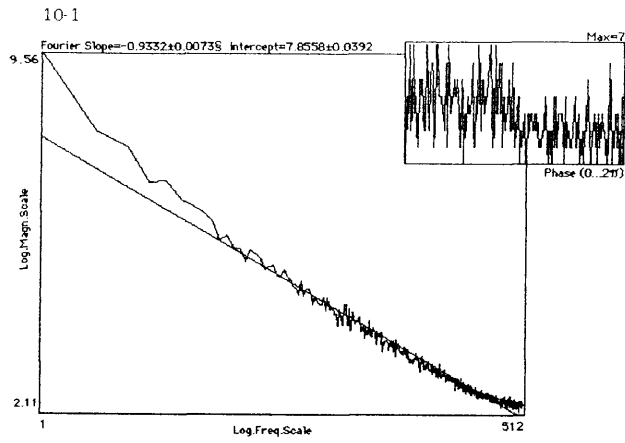


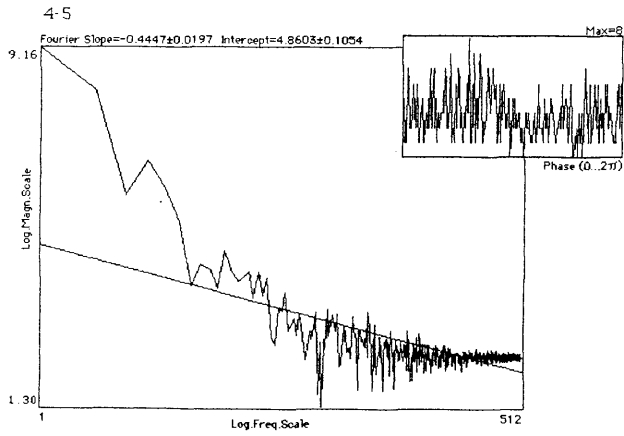
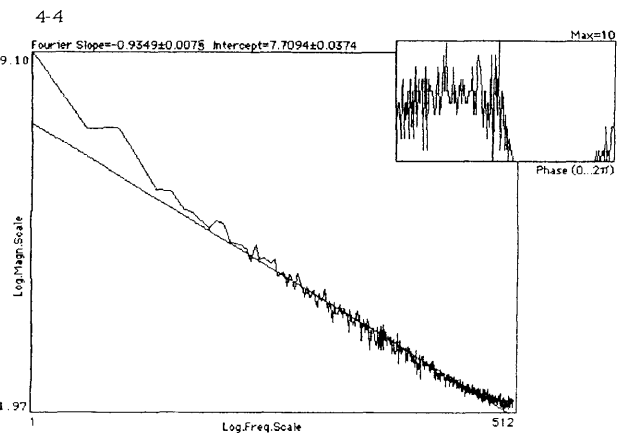
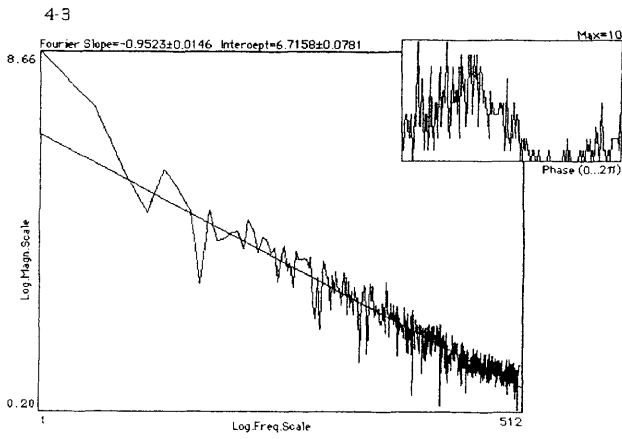
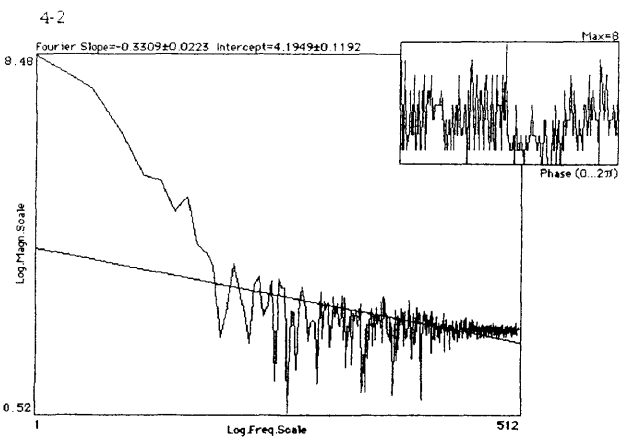
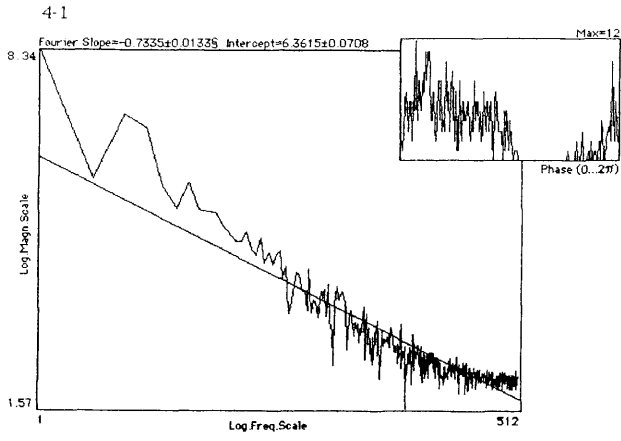
Figure 43. Semivariograms for fractal lines: (a) semivariogram for entire data series from line generated by fractal Brownian motion simulation ($\alpha = 0.5$, $D = 1.5$), (b) origin of (a) magnified, (c) semivariogram for entire data series from line generated by Fourier spectrum with Gaussian magnitudes distributed according to the specified slope ($\alpha = 0.5$, $D = 1.5$) and random phase, and (d) origin of (c) magnified. Fractal lines generated by "Fractals" (copyright John Russ). Semivariograms produced using "Surface III+" (copyright Kansas Geological Survey).

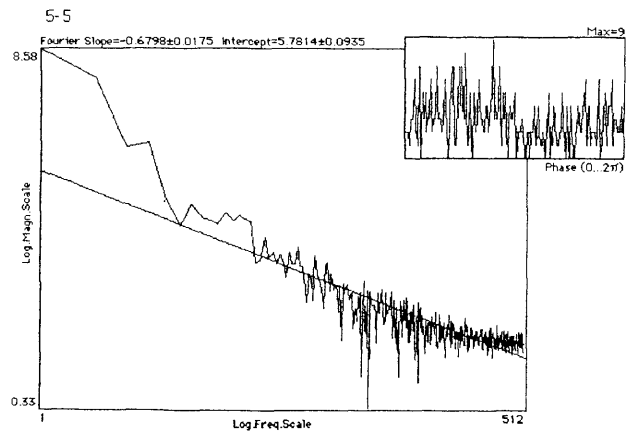
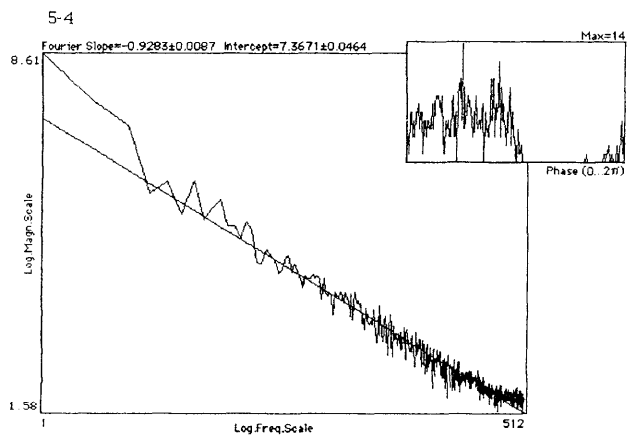
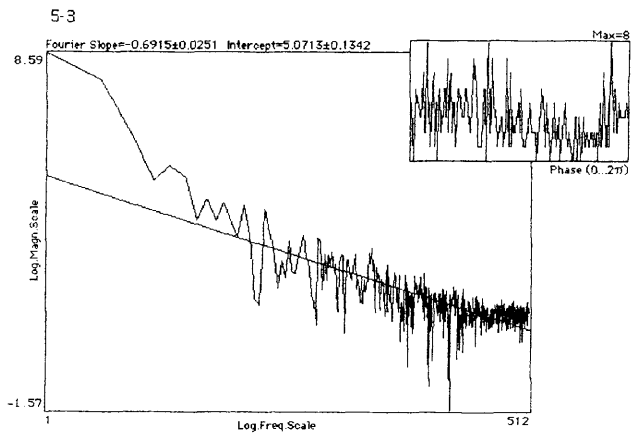
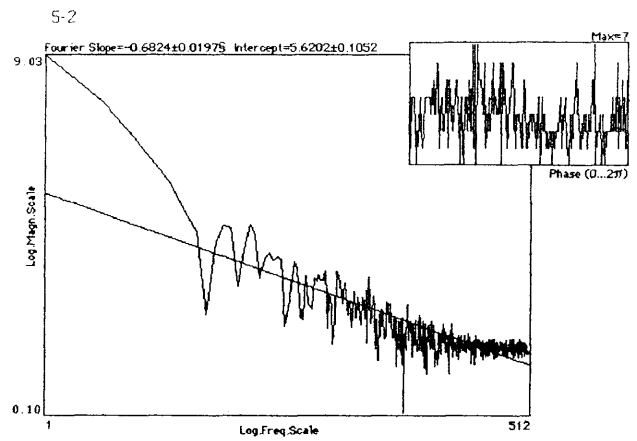
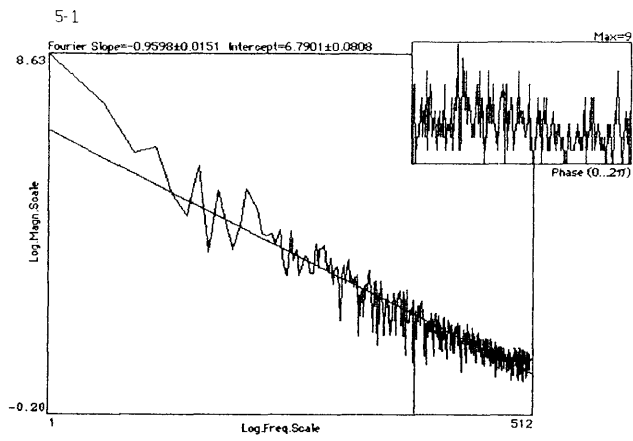


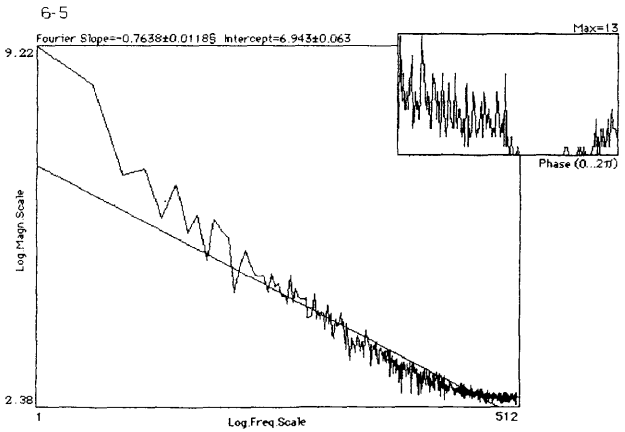
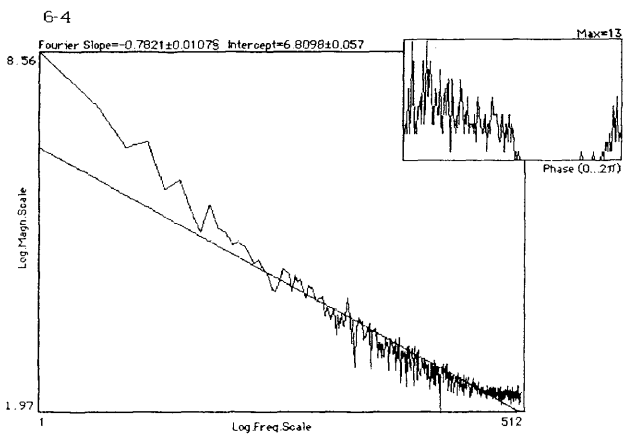
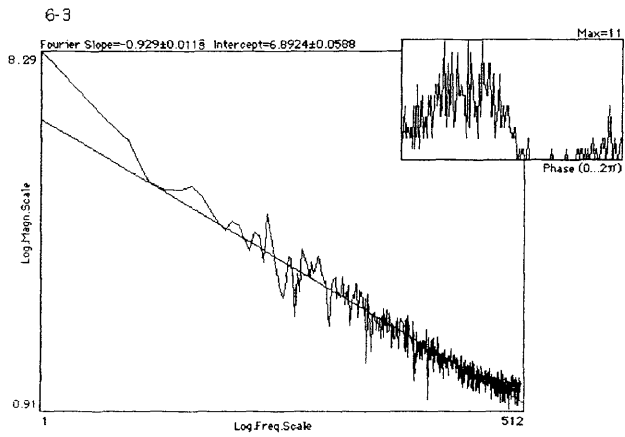
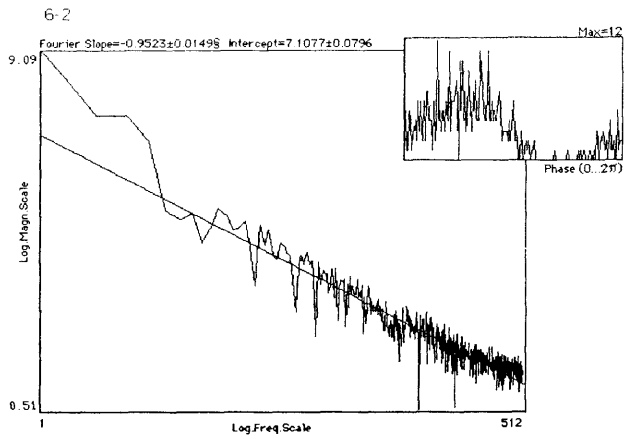
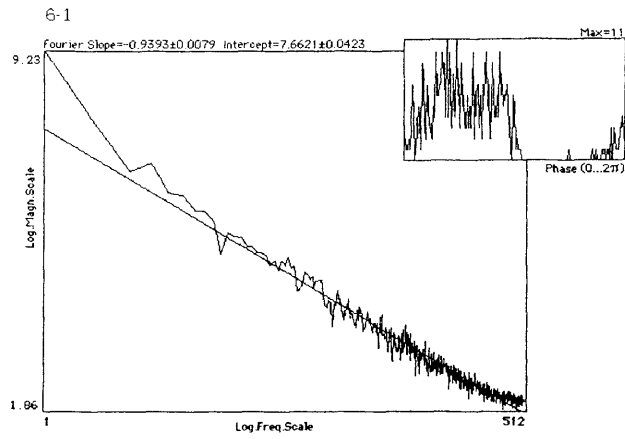


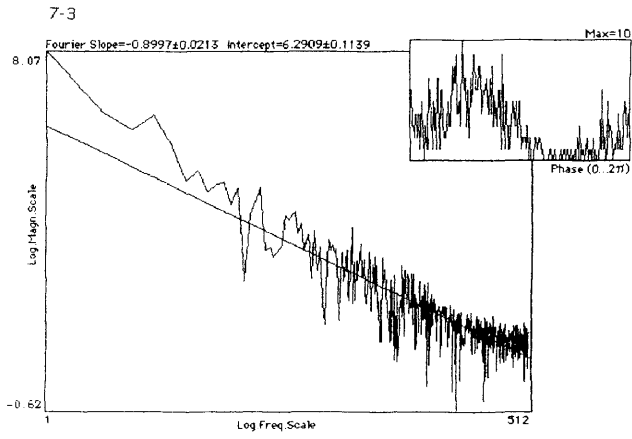
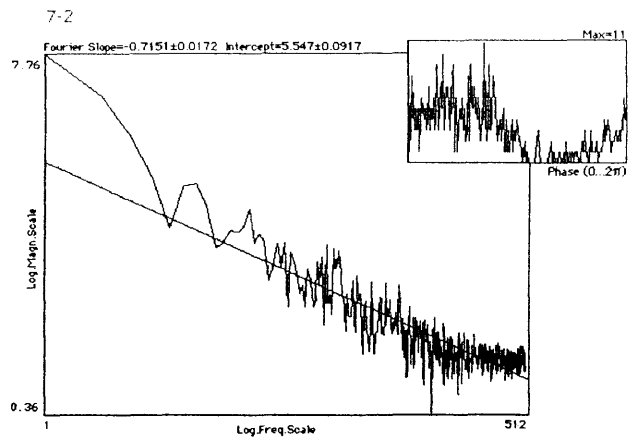
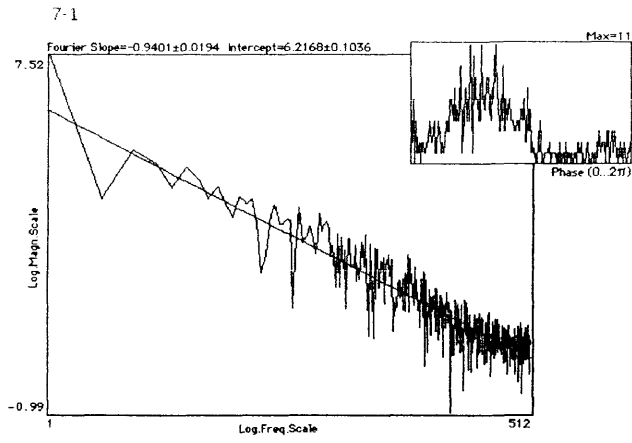




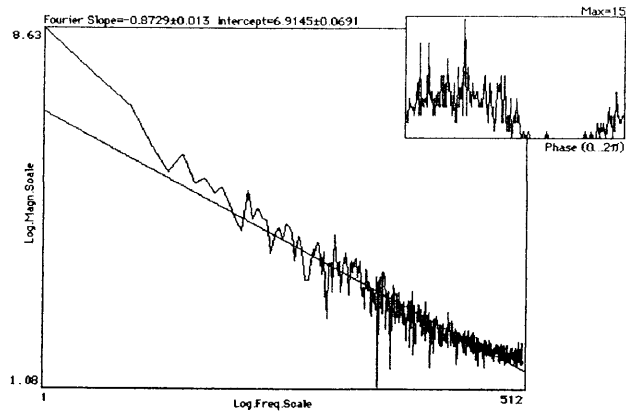


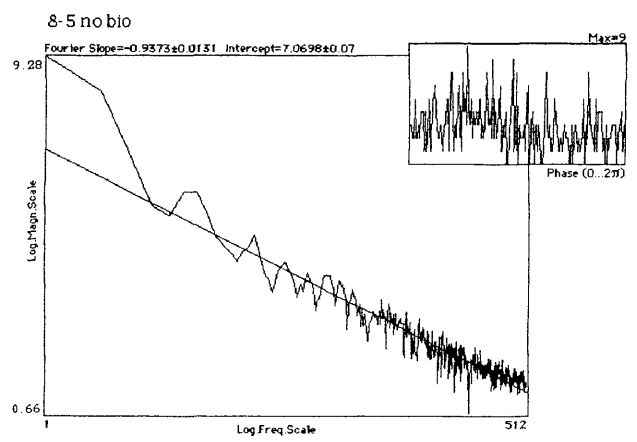
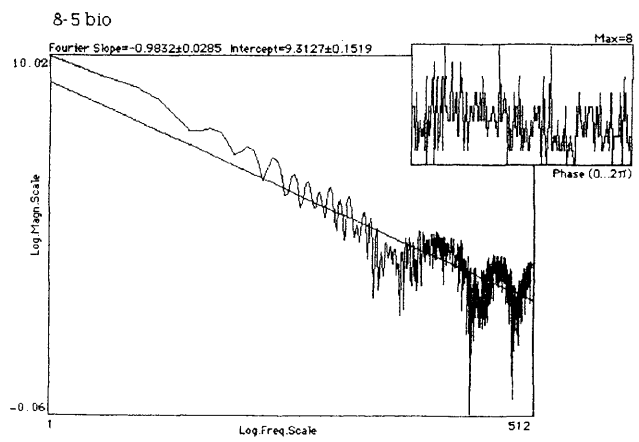
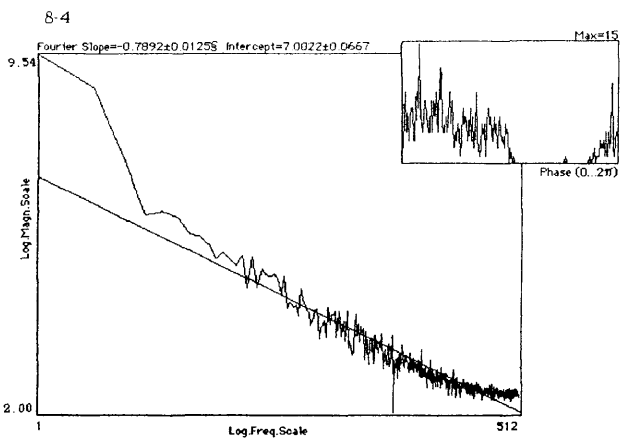
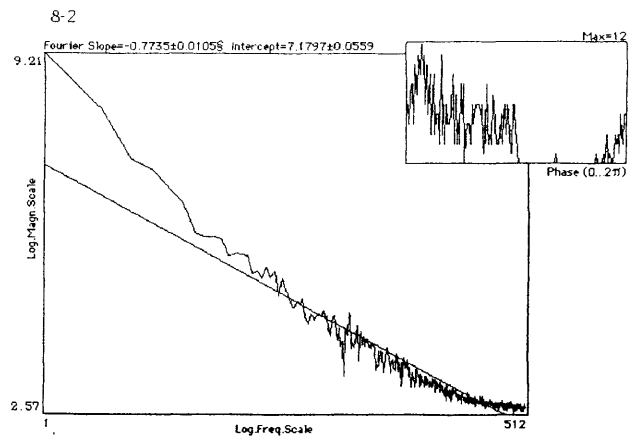


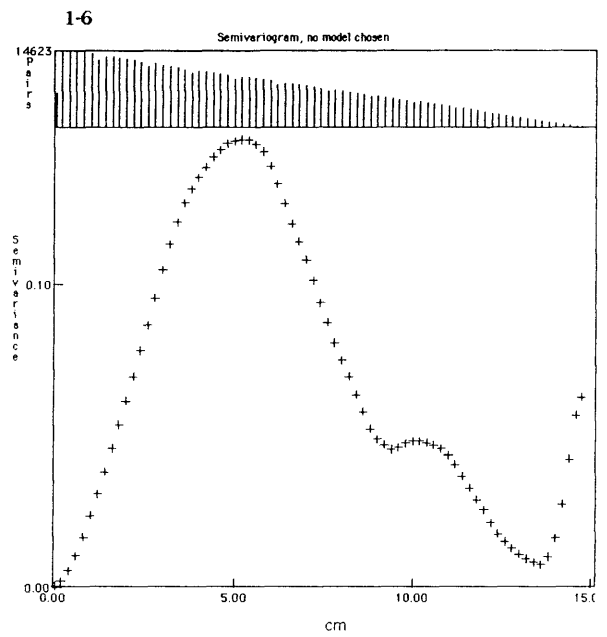
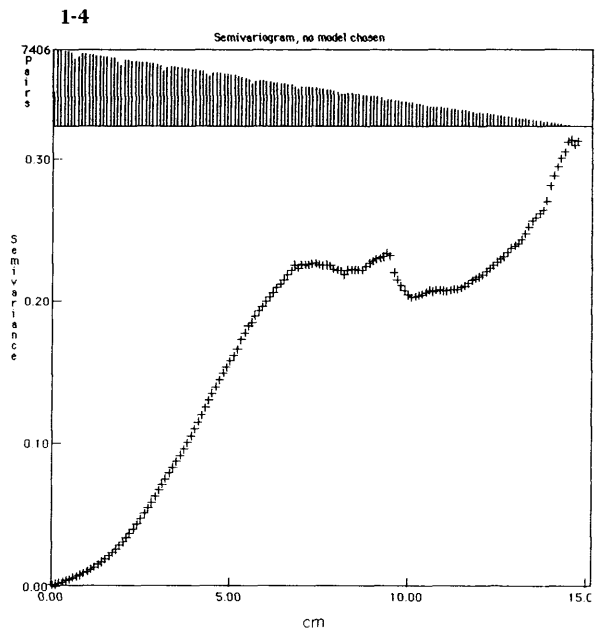
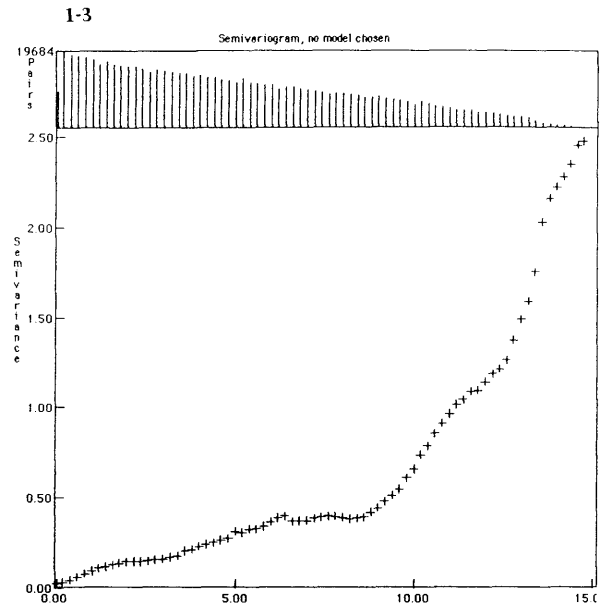
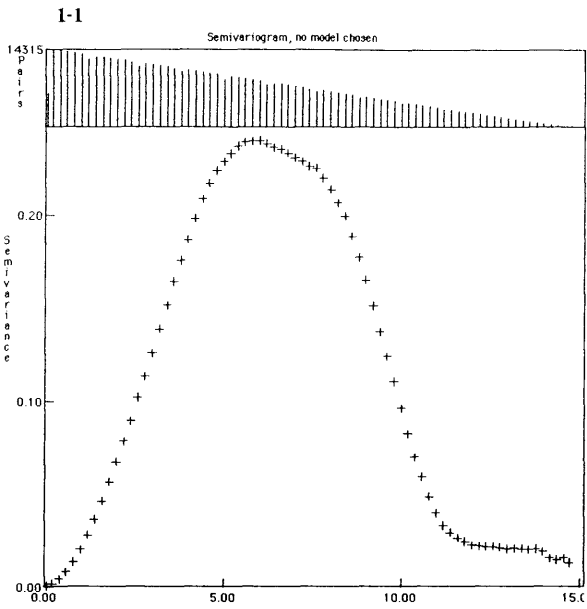


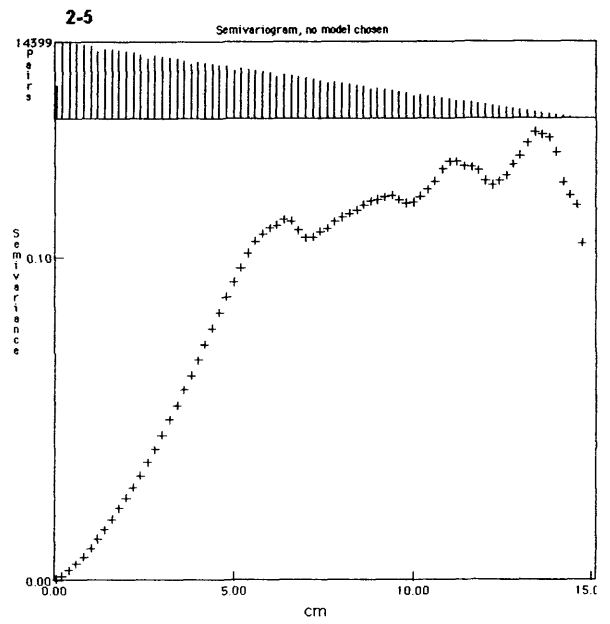
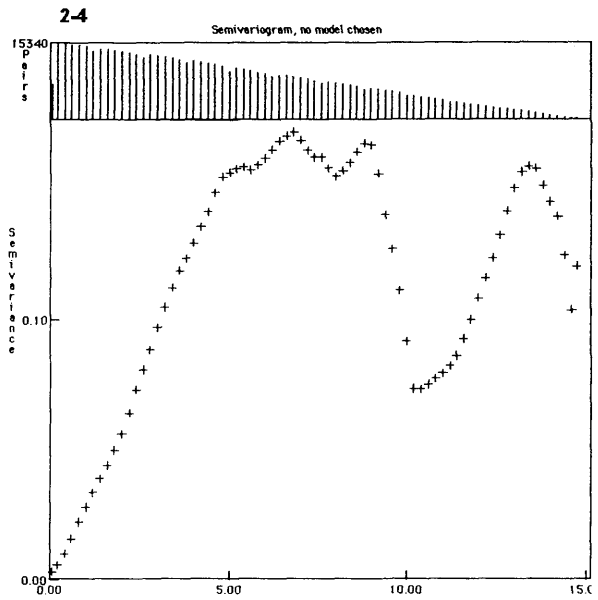
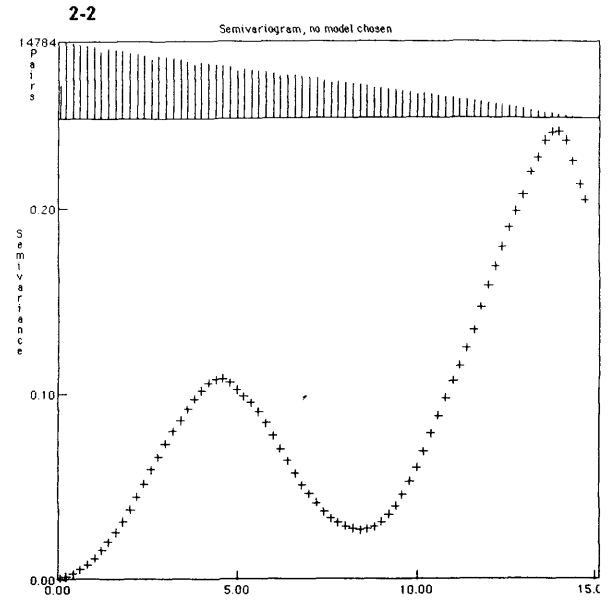
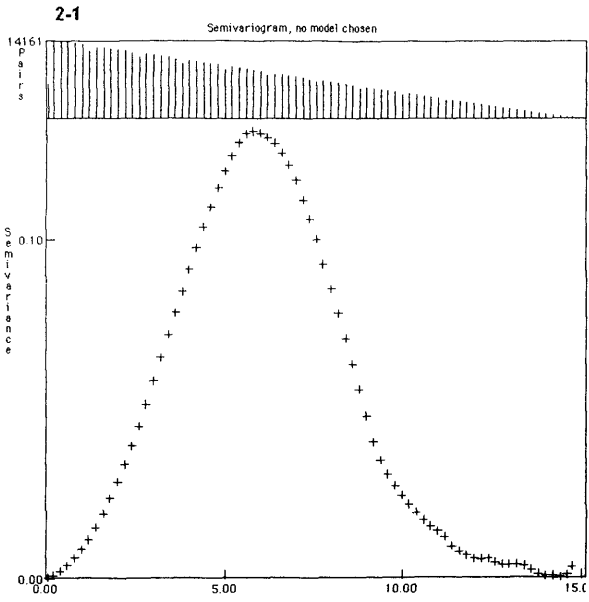


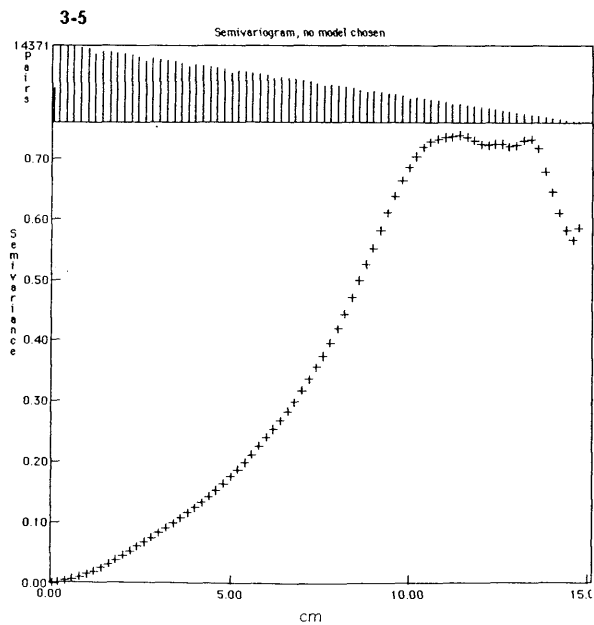
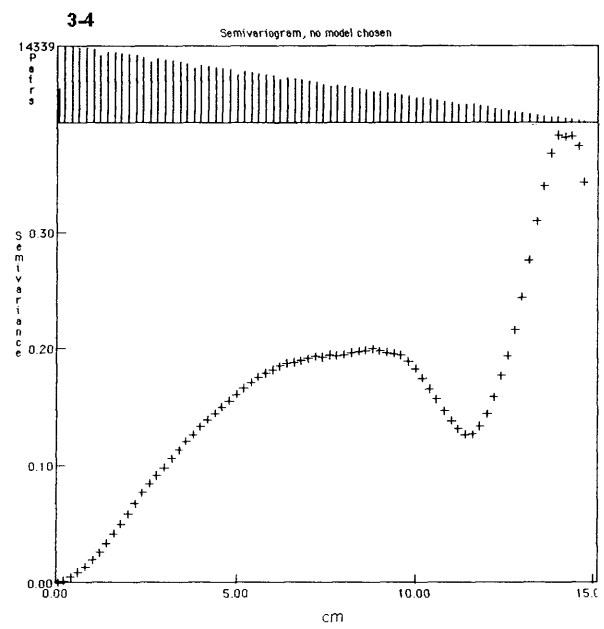
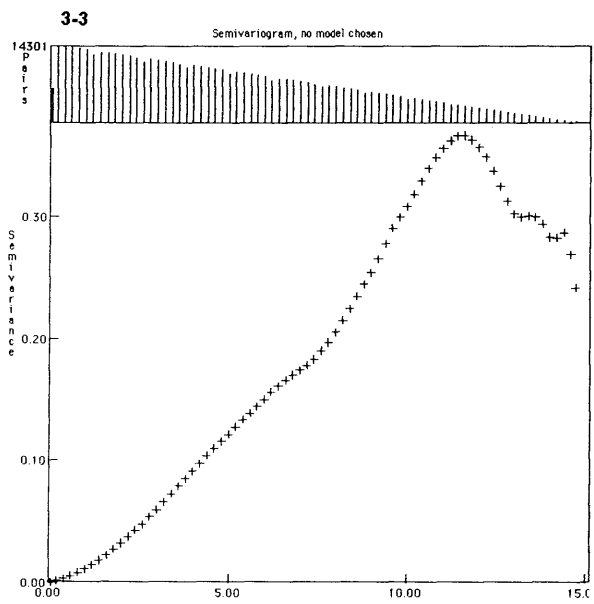
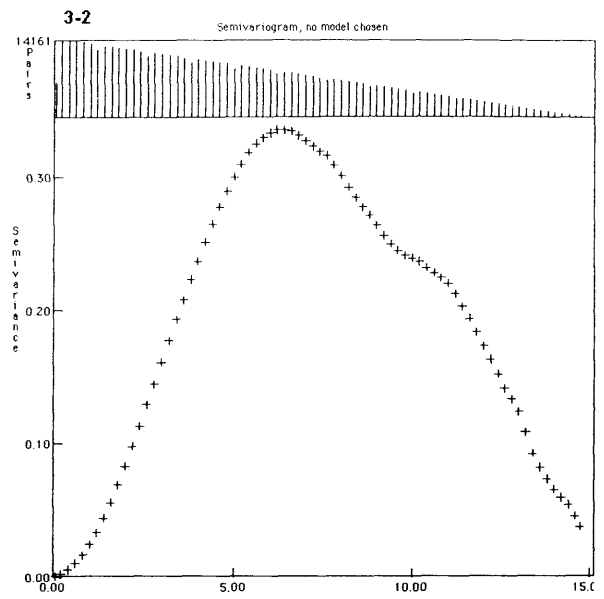
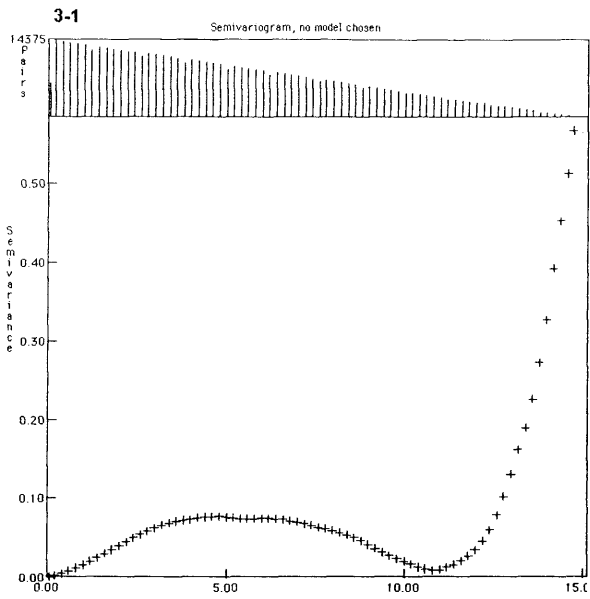
9-1

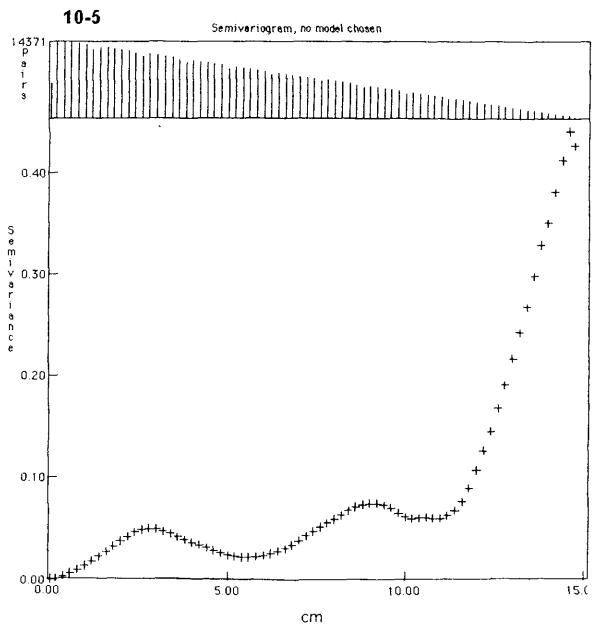
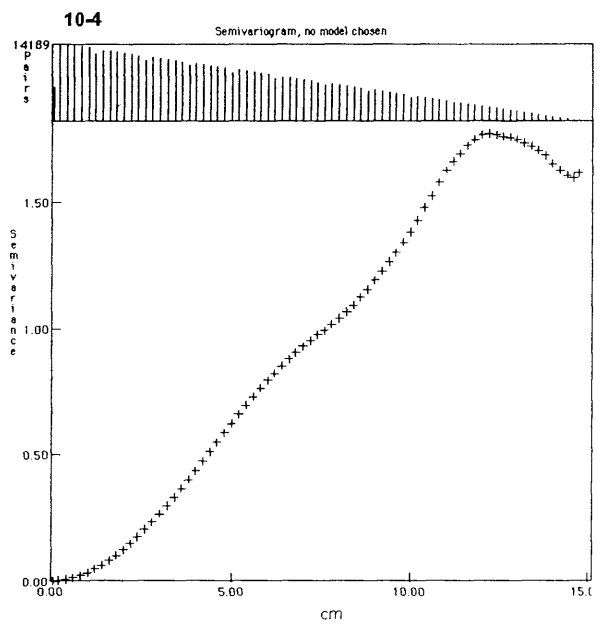
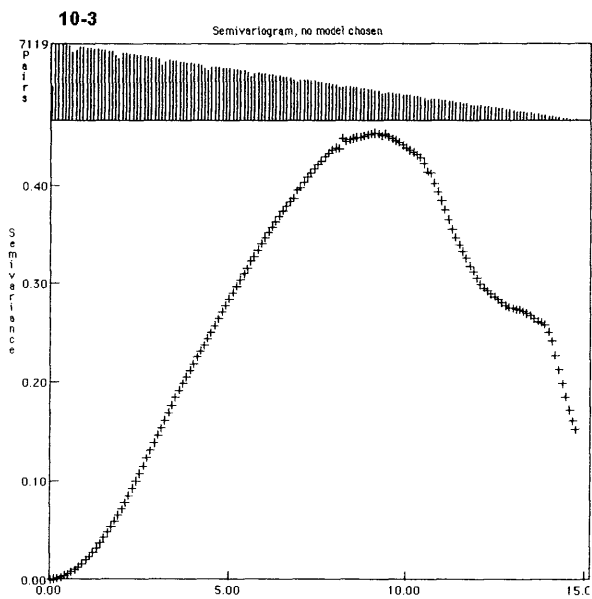
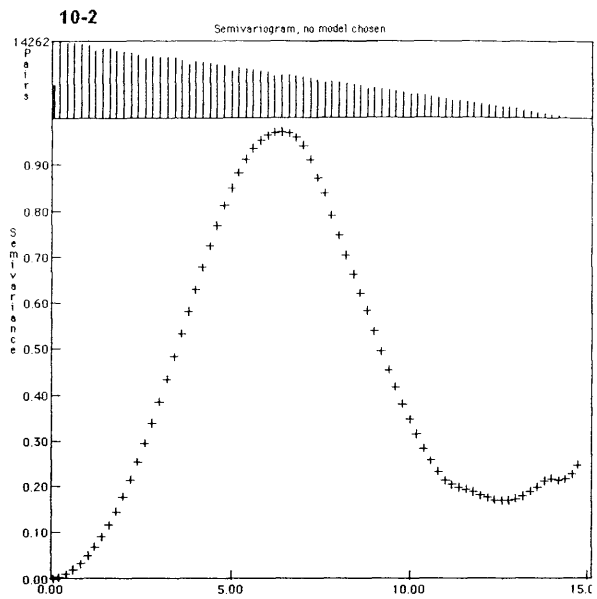
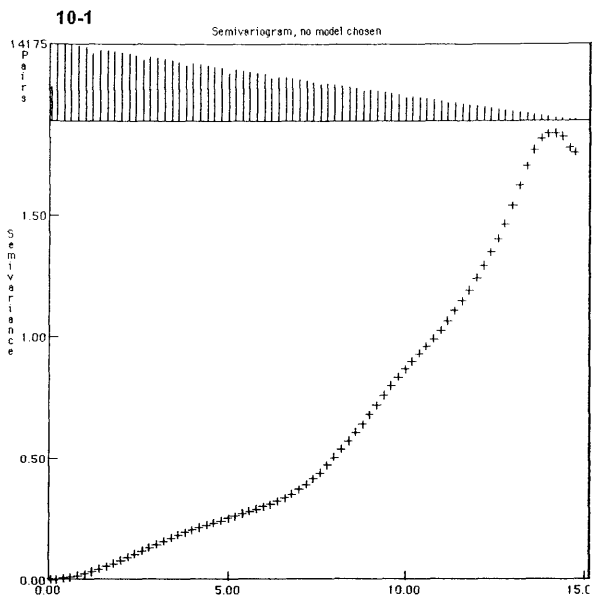


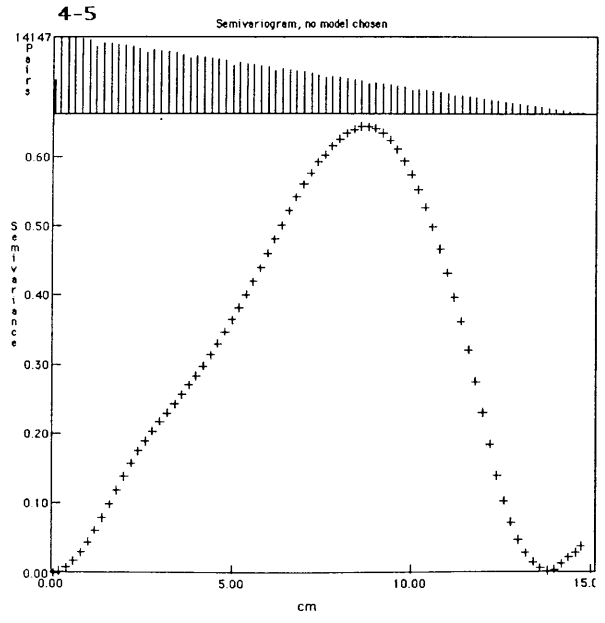
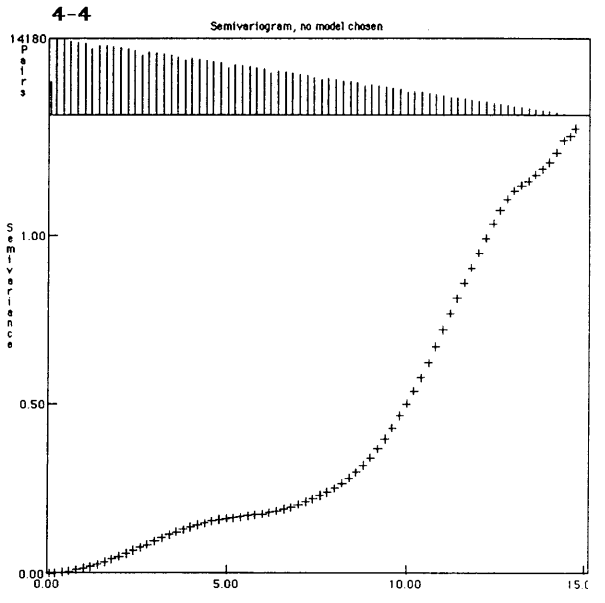
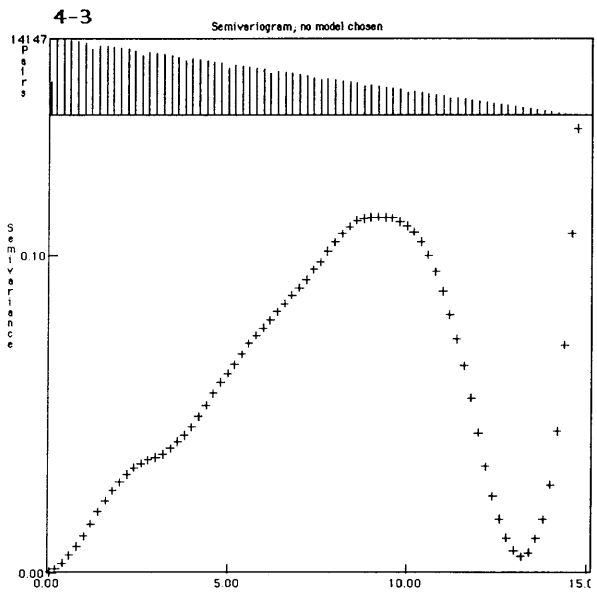
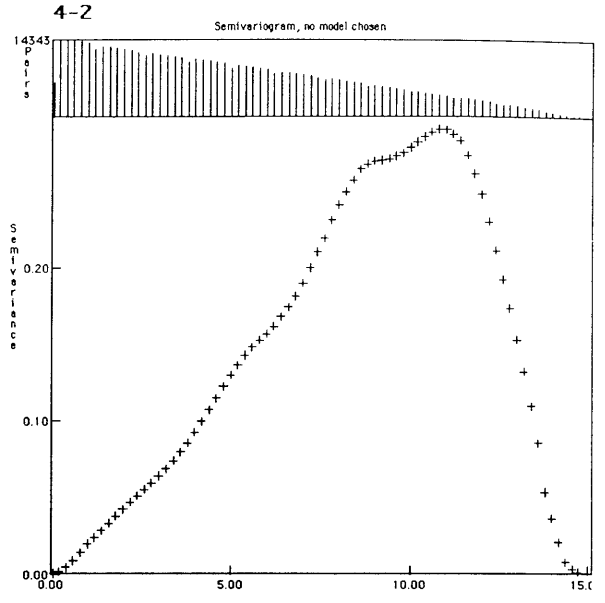
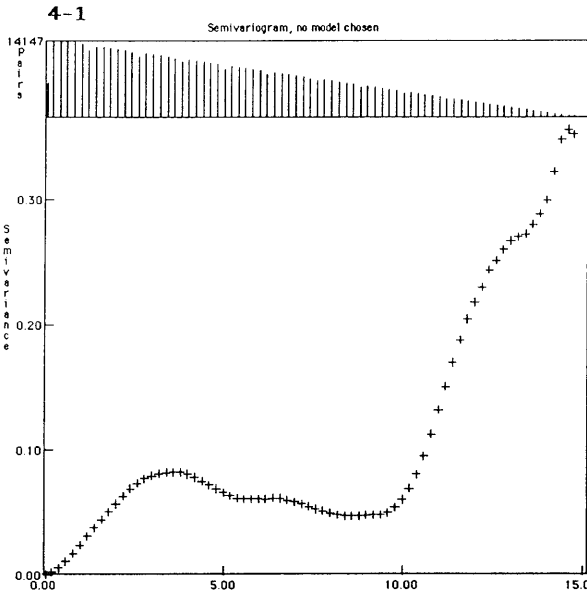


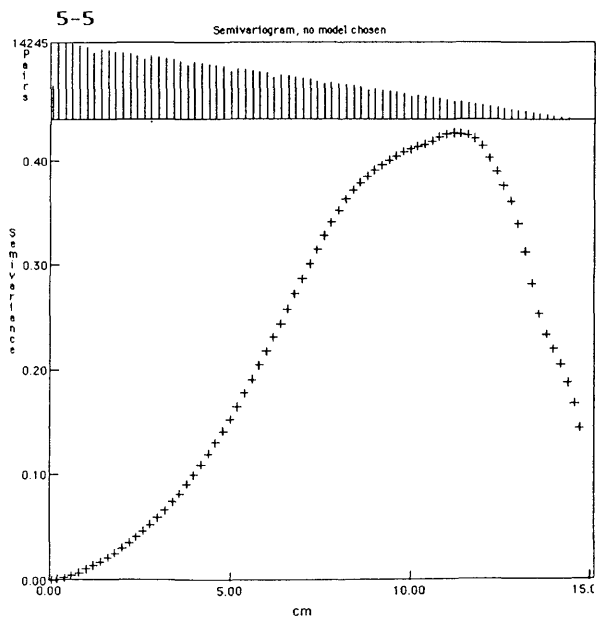
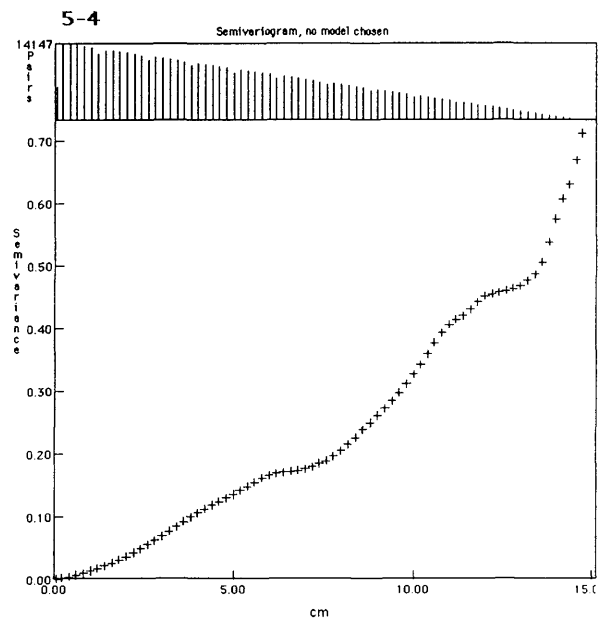
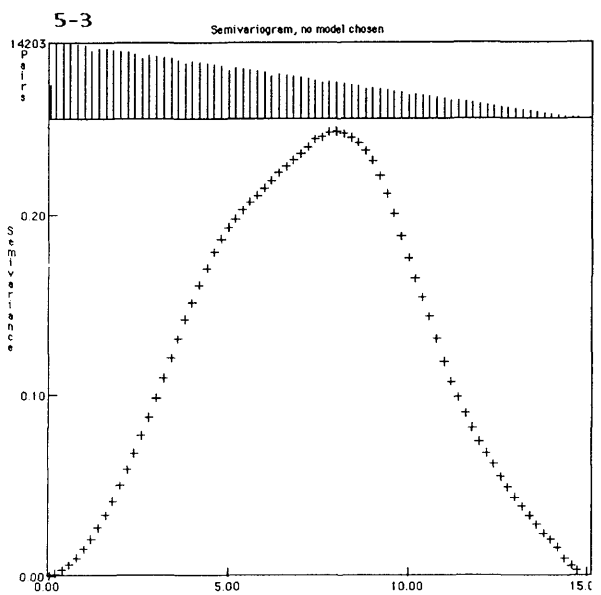
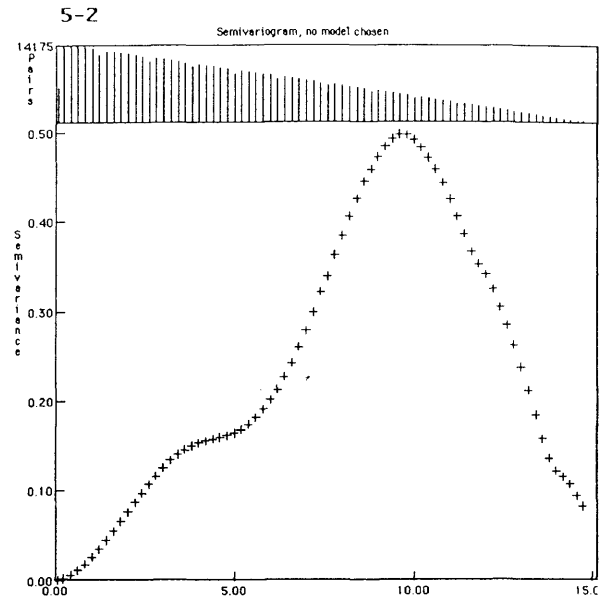
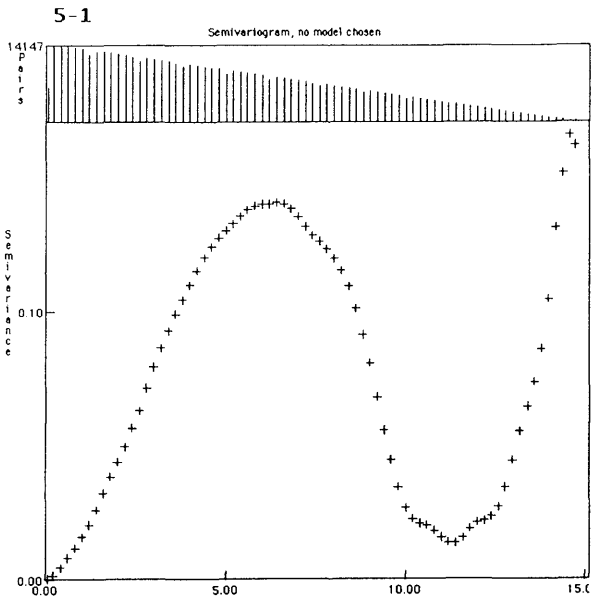


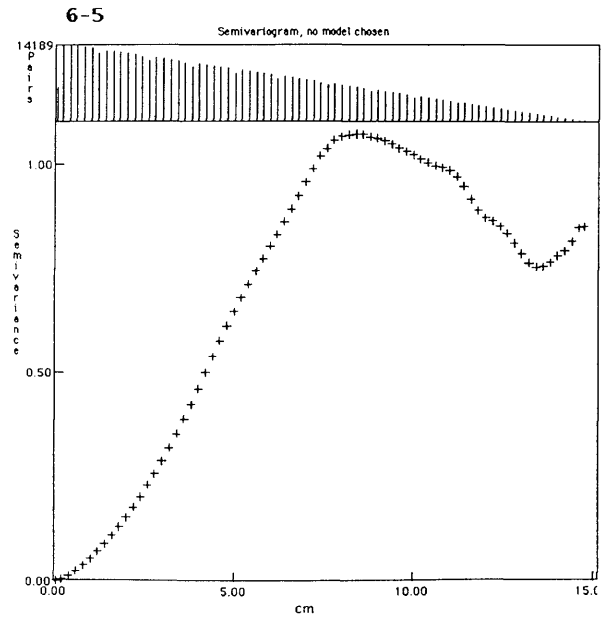
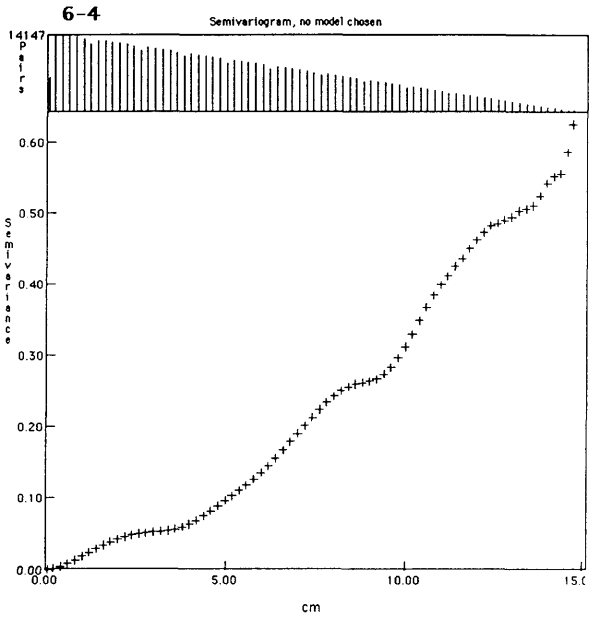
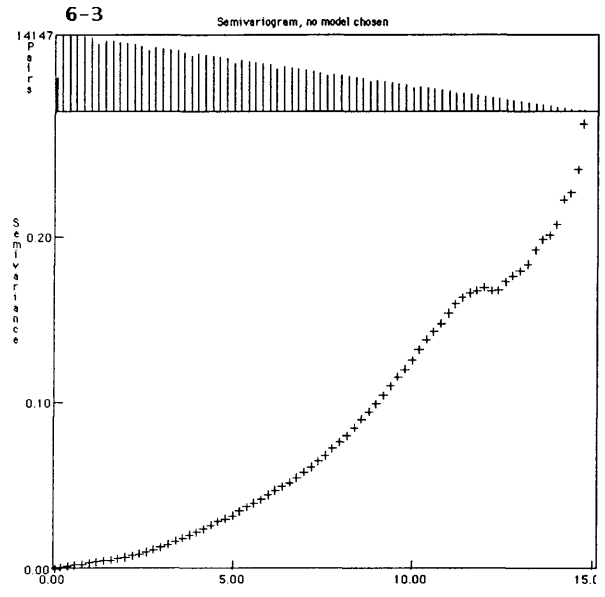
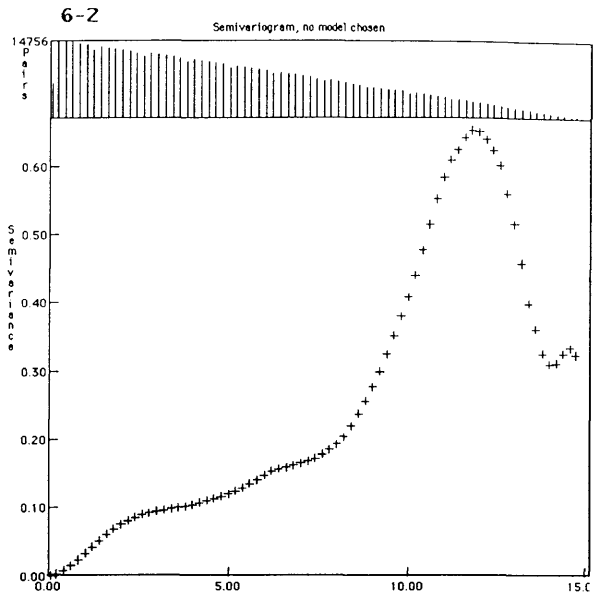
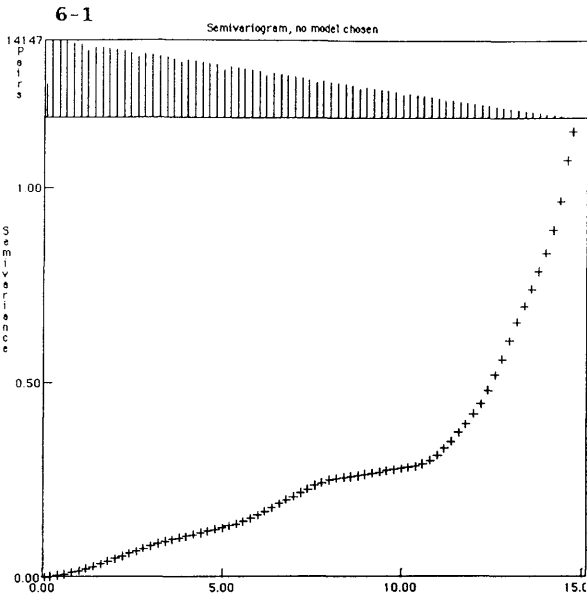




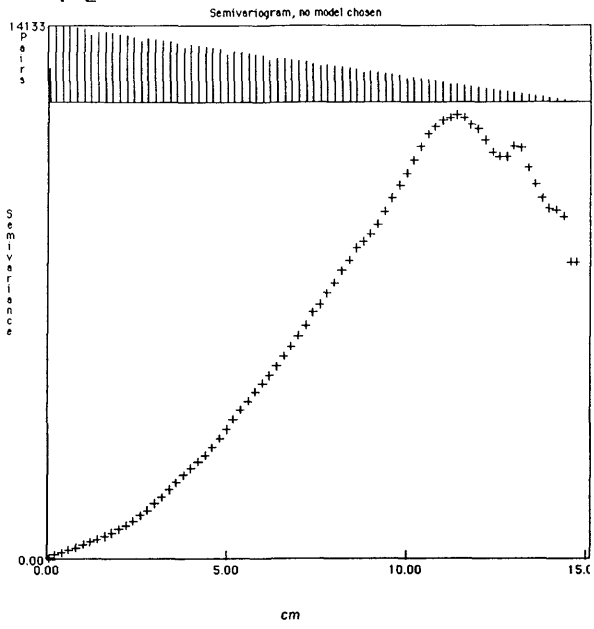




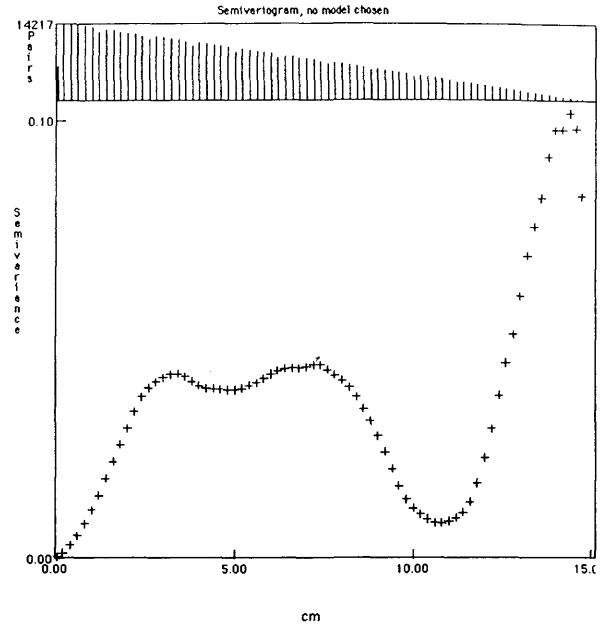




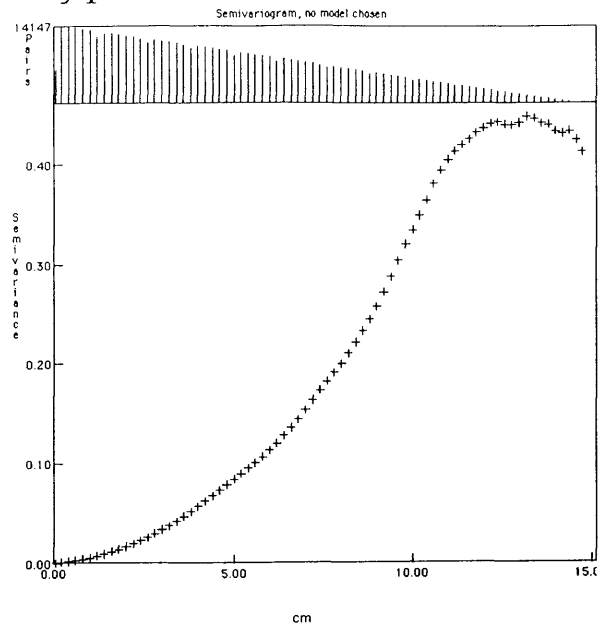
7-2



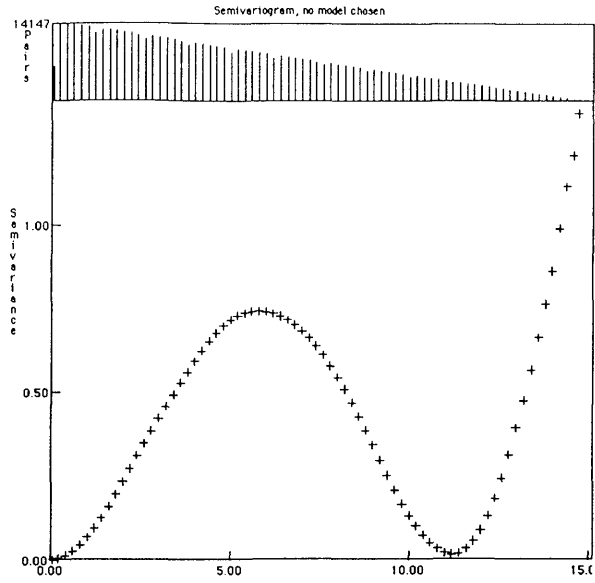
7-4



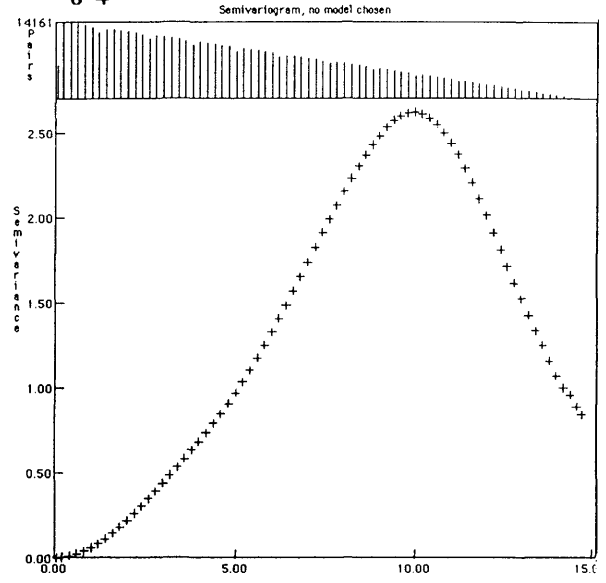
9-1



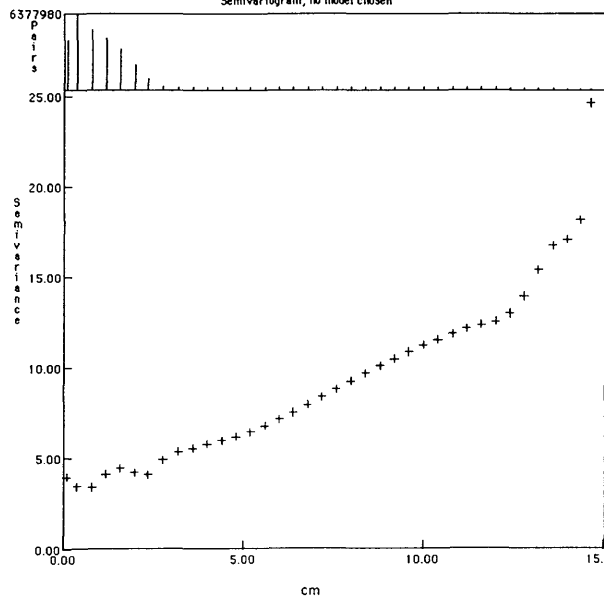
8-2



8-4



8-5 with epifauna



8-5 without epifauna

